Alignment calibration of the GALA laser altimeter through laser ranging to Earth

Development of a calibration for the Ganymede Laser Altimeter

M. Smeets

Delft University of Technology

Master Thesis Aerospace Engineering

TU Delft

Alignment calibration of the GALA laser altimeter through laser ranging to Earth.

Master Thesis

by

Martijn Smeets

To obtain the degree of Master of Science
at the Delft University of Technology,
to be defended publicly on Monday August 7, 2017 at 14:00 PM.

Student number:	1526863	
Project duration :	September, 2016 – July, 2017	
Thesis committee:	Dr. Ir. Dominic Dirkx	TU Delft, supervisor
	Dr. Hauke Hussmann	DLR
	Prof. Dr. Pieter Visser	TU Delft
	Ir. Prem Sundaramoorthy	TU Delft

The author can be contacted at: martijnsmeets205@gmail.com.

An electronic version of this thesis is available at: http://repository.tudelft.nl/

TU Delft Delft University of Technology

DLR Deutsches Zentrum für Luft- und Raumfahrt
German Aerospace Center

Preface

This thesis concludes my master Space Exploration at the Delft University of Technology and my involvement in the development of the Ganymede Laser Altimeter (GALA) at the Deutsches Zentrum für Luft und Raumfahrt (DLR) in Berlin. It is for now my main achievement and contribution to the world of space flight and exploration. The master space flight was not always an obvious choice for me. It was my final bachelor project, or Design Synthesis Exercise (DSE), that sparked my interest for space flight. During this project I discovered that I really liked working on a space exploration project and at the end of the DSE, I decided to pursue a master in this field.

Starting this master I decided that I would not only do a master in this field, but also dive into the world of space flight; rockets, satellites and the solar system. I became involved with the Delft Aerospace Rocket Engineering (DARE) student team and attended numerous space flight oriented activities such as a trip to various space related companies organised by the study Society of Aerospace Students (VSV) 'Leonardo da Vinci'. Just before leaving for an internship at Airbus Defence and Space in Friedrichshafen, I began to search for a topic for my master thesis. During this process I became aware that I wanted to contribute to an active project in space and came into contact with Dr. Ir. Dominic Dirkx. He could tell me about an upcoming project in his field of expertise; laser ranging. This project was the development of GALA, performed by DLR in Berlin. After contacting Dr. Hauke Hussmann, the project leader for GALA, a work plan was devised that really made me enthusiastic. I decided that I would take on this challenge, supervised by Dominic Dirkx, and perform most of the work at DLR in Berlin at the Institute of Planetary Research in the Planetary Geodesy group.

For 7 months I joined the Planetary Geodesy group where I was guided by Dr. Hauke Hussmann, Dr. Alexander Stark and Gregor Steinbrügge. It was a great experience to be able to perform my work close to the GALA team where I was able to attend meetings and ask various persons for their expertise. This also enabled me to make a trip to the laser ground station at Wettzell which was a really valuable and close-by experience of laser ranging in practice. Here I also met Prof. Dr. Ulrich Schreiber, who provided me with an abundance of practical experience on laser ranging. All this culminated to the final months in Delft for the writing of my final thesis. For this warm welcome I am the entire team in Berlin very grateful.

I would like to thank Dominic Dirkx for supervising me during my entire thesis work. During the development of a topic for my thesis, writing my literature study and throughout my thesis work he provided me with ideas, help and guidance for which I am very grateful. I thank him for setting up contact with DLR in Berlin who offered me the opportunity to experience space exploration at this renowned institute.

For the invite to DLR in Berlin I would like to thank Hauke Hussmann who arranged this for me, and for his help and guidance. Alexander Stark shared not only his office with me, but also his time, helping me with whatever came to my mind and introducing me to various aspects of laser ranging, altimetry and so many other topics of which Alexander seems to have knowledge. I would like to thank him for this and thank Gregor Steinbrügge for his help and guidance and for taking part in the trip to Wettzell, for which I thank Ulrich Schreiber. I thank my friends and the people I met throughout my study and master for making it a great time.

Last but not least I am very grateful for the support throughout my study by my parents and sisters who supported my throughout my study and master. Who moved me to and from Germany 4 times and were always there to help me further with whatever I was facing. I am forever thankful for their energy and time.

Martijn Smeets
Delft, July 2017

Abstract

As part of the ESA mission to Jupiter and Ganymede carried out by the Jupiter Icy Moons Explorer (JUICE) spacecraft, the Ganymede Laser Altimeter (GALA) will determine the topography and detect Ganymede's tidal degree-2 signal in order to investigate the existence of a subsurface ocean and constrain its thickness. To deliver successful measurements GALA is to be calibrated for its misalignment with an accuracy of at least 14 arcsec. This misalignment cannot be measured on ground since it will be subject to vibrations, microgravity and settling after launch. Thus this calibration is to be performed while JUICE is on its interplanetary cruise to Jupiter.

This thesis aims to answer the question how this calibration can be performed using laser ranging to an Earth-based ground station. This calibration procedure consists of a scan performed by JUICE with a size as large as the maximum expected misalignment found at 333 arcsec. A model for the attitude during laser ranging was developed to be used to simulate the distribution and intensities of the laser pulses transmitted by GALA. During this scan of several hours and with a shot frequency of 30 Hz, the ground station will be able to detect 500 to 1500 pulses. This result was validated with the real life MLA and Hayabusa experiments already performed. The spatial distribution of these detected pulses is used to reconstruct the Gaussian pulse shape of the laser pulses. By determining its peak intensity, the ground station location can be estimated which is used to measure the misalignment. This estimation procedure was found to be robust and reliable enough to be incorporated in the simulation tool that can be run many times to achieve a statistically significant result on the estimation error. Since the estimation is based on the spatial distribution, the main drivers for the accuracy are the slew rate, scan pattern, distance, detection threshold and attitude model. These were investigated for their influence on the calibration and used to find their optimal values.

The trajectory of JUICE was analysed for the most optimal opportunities given various constrains to perform a laser ranging campaign leading to a selection of options to be analysed. Using the simulation it was found that interplanetary laser ranging can be used to calibrate GALA by employing 8-10 hours of scanning at a distance no further than around 0.5 AU by using ground station characteristics such as found at Wettzell with a telescope diameter of 0.75 metres and optical and quantum efficiencies of 0.5 and 0.2 respectively. For the most optimal opportunity, laser ranging will be performed at a distance of 0.39 AU for 10 hours with a slew rate of 0.0055 deg/s. This leads to a 2 sigma calibration residual of 3.62 arcsec resulting in a total calibration error of 11 arcsec. This confirms the assumption that a calibration accuracy of 14 arcsec is possible and thus a successful laser altimetry mission can be performed by GALA.

Contents

List of Figures

List of Tables

Abbreviations

ACE	Absolute Control Error.
ACKE	Absolute Control Knowledge Error.
AGE	Absolute Guidance Error.
AGKE	Absolute Guidance Knowledge Error.
AKE	Absolute Knowledge Error.
APD	Avalanche Photodiode.
APE	Absolute Pointing Error.
APOLLO	Apache Point Observatory Lunar Laser-ranging Operation.
BELA	BepiColombo Laser Altimeter.
CE	Control Error.
DLR	Deutsches Zentrum für Luft und Raumfahrt.
EIDA	Experiment Interface Document - Part A.
EIDB	Experiment Interface Document - Part B.
ELU	Electronic Unit.
ESA	European Space Agency.
FOV	Field of View.
GALA	Ganymede Laser Altimeter.
GCO	Ganymede Circular Orbit.
GE	Guidance Error.
GGAO	Goddard Geophysical and Astronomical Observatory.
GLAS	Geoscience Laser Altimeter System.
HGA	High Gain Antenna.
IAG	International Association of Geodesy.
ILRS	International Laser Ranging Service.
ILS	Instrument Line of Sight.
ITRF	International Terrestrial Reference Frame.
JUICE	JUpiter ICy moons Explorer.
LEU	Laser Electronic Unit.
MKE	Mean Knowledge Error.
MLA	Mercury Laser Altimeter.
MPE	Mean Pointing Error.
NASA	National Aeronautics and Space Administration.
PMTs	Photomultiplier Tubes.
RKE	Relative Knowledge Error.
RPE	Relative Pointing Error.
SAPD	Single-photon Avalanche Photodiode.
SLR	Satellite Laser Ranging.
SPICE	Spacecraft Planet Instrument Camera matrix Events.
TIA	Transimpedance Amplifier.
TPAGKE	Total Pointing, Alignment & Guidance Knowledge Error.
TRU	Transceiver Unit.
WPLTN	Western Pacific Laser Tracking Network.

Nomenclature

A_r	Receiver area	m^2
AU	Astronomical Unit	149 597 871 kilometres
σ_{atm}	Attenuation coefficient	-
B_0	Transimpendance amplifier bandwidth	Hz
c	The speed of light	m/s
d	Distance	m
du	Difference in radial displacement	m
d_r	Receiver telescope diameter	m
Δt	Time of flight	sec
E_T	Energy of the laser pulse transmitted	mJ
E_t	Energy transmitted	mJ
E_p	Energy of a photon	mJ
e	Error	arcsec
e_p	Pointing error	arcsec
e_r	Error set as requirement	arcsec
e_x	Error around in x direction	arcsec
e_y	Error around in y direction	arcsec
f_q	Frequency at which the laser pulses are fired	Hz
M	Gain of an APD	-
g	Gravitational acceleration	m/s^2
h_2	First Love number	-
H	Altitude	m
h	Height	m
h_t	Height of the ground station	m
h_{sc}	Atmospheric scale height	km
I_D	APD dark current	A
I_{DB}	APD dark current (bulk)	A
I_{DS}	APD dark current (surface)	A
I	Intensity	photons/m^2
I_0	Peak intensity of the Gaussian pulse	photons/m^2
k_2	Second Love number	-
k	Realisation	-
M	Mass	kg
N_b	Detected background noise photoelectrons	photoelectrons
N_λ	Solar irradiance at Earth	W/m^2/nm
n_p	Level of confidence	sigma
N_{RG}	Number of bins in a range gate	bins
N_s	Total detected signal photoelectrons from the laser pulse	photoelectrons
K_t	Threshold	photoelectrons
N_{tot}	Total detected photoelectrons	photoelectrons
n_r	Number of photons received	photons
n_T	Number of photons transmitted	photons

h	Planck constant	m^2kg/s
P	Probability	-
P_d	Probability of detection	-
P_{fa}	False detection probability	-
P_{FD}	Probability of false detection	-
R	Distance spacecraft to nadir surface	m
r	Radial distance from the midpoint of the beam	m
R	Radius of the body	m
r_R	Telescope radius	m
R_{ref}	Reference surface height	m
θ_z	Zenith angle	deg
θ_J	Zenith angle of JUICE	deg
θ_S	Zenith angle of the Sun	deg
t	Thickness of cirrus clouds	km
t_i	Estimated parameters	-
t	Time	sec
t_{bin}	Length of bin in time	sec
t_g	Length of the range gate	sec
n_{total}	Total number of photons	photons
t_r	Time of arrival	sec
T	Transmission factor	-
T_{atmos}	Atmospheric transmission factor	-
T_c	Transmission factor for cirrus clouds	-
T_{total}	Total transmission factor	-
t_t	Time of transmission	sec
u_r	Radial displacement at the surface	m
V	Visibility	m
w_0	Beam waist radius	m
w	Radial size of the laser spot	m
y_i	Measured data	-
z	Range measured by altimeter	m
z	Altitude of scattering volume	m

Greek symbols

α	Surface slope	deg
α	Angle between JUICE and the Sun	deg
Δt	Time interval	sec
Δv	Change in velocity	m/s
$\Delta\phi$	Pointing error	arcsec
$\Delta\phi_a$	Alignment error	arcsec
$\Delta\phi_c$	Spacecraft control knowledge error	arcsec
$\Delta\phi_g$	Spacecraft trajectory knowledge error	arcsec
ϵ_{RF}	Optical filter efficiency of the receiver	-
η_t	Optical efficiency of the transmitter	-
η_q	Quantum efficiency of the detector	-
η_r	Optical efficiency of the receiver optics	-
λ_t	Wavelength of transmitted laser pulse	nm
μ_{total}	Total mean error	arcsec
ν	Frequency	Hz
Ω	Solid angle	sr
Ω_r	Receiver Field of view	sr
ϕ	Off-nadir pointing angle	arcsec
δz	Range error	m
ρ	reflectivity constant	-
σ_f	Digital filter width	Hz
σ_0	Pulse width	sec
σ_{RF}	Optical filter bandpass widths	Hz
σ_σ	Standard deviation of the standard deviation	arcsec
$\Delta\lambda$	Spectral bandwidth of the spectral filter	nm
τ	Offset in time between measurements	sec
τ	Time since laser pulse is transmitted	sec
θ_{cmd}	Commanded attitude	-
$\theta_{\frac{1}{2}}$	$1/e^2$ Half cone divergence angle	arcsec
θ_{SC}	True spacecraft attitude	-
θ_T	Divergence angle	arcsec
θ_T	$1/e^2$ Full cone divergence angle	arcsec
Φ	Tidal potential	-
Θ_{FOV}	Full cone field of view	arcsec

1 Introduction

As part of the European Space Agency's (ESA) Cosmic Vision program, the first large class mission, the JUpiter ICy moons Explorer (JUICE) (Grasset et al., 2013) will be launched in 2022 to investigate Jupiter and its moons Ganymede, Callisto and Europa. Part of the payload is the Ganymede Laser Altimeter (GALA), which main objectives are to determine the topography of Ganymede on various scales and to detect its tidal degree-2 signal. This is crucial to investigate the existence of a subsurface ocean on Ganymede and to constrain the thickness and rheology of the outer ice shell above this ocean.

The quality of the measurements taken by GALA and thus its scientific performance, are heavily influenced by instrument errors and pointing errors. For both types, GALA is to be calibrated to guarantee successful measurements. Most instrument errors that are caused by internal electronics and the internal clock can be measured during testing on ground or can later be measured in orbit. The highest uncertainty in the measurements is caused by the pointing and alignment errors (Steinbrügge et al., 2015), even if it is presumed that the laser altimeter is calibrated during planetary cruise. An improvement on this aspect would appreciably improve the measurements of GALA. One contribution in this error is the misalignment between the laser line of sight and the nadir axis of the spacecraft which is under influence of settling due to vibrations and microgravity present during and after launch of the spacecraft. Therefore the only option is to measure this when the spacecraft is already on its way to Jupiter and in this thesis, calibration through laser ranging to an Earth-based laser ground station is studied.

1.1. Laser Altimetry

A laser altimeter measures the distance d to the surface by measuring the time of flight Δt of the laser pulse. This is sent by the transmitter using a laser, bounces back from the surface and is detected by the receiver of the laser altimeter. Therefore the distance for the ideal case is half of the measured time of flight;

$$d = \frac{1}{2} c \Delta t \tag{1.1}$$

where c is the speed of light. Although simple in its concept, in practice several issues are present, both advantageous and disadvantageous. As the distance measured is strongly dependent on Δt it is important to measure the time of transmission t_t and the time the laser pulse is received t_r. However many issues are present here, for example the laser pulse sent can be approximated by a Gaussian pulse, with a clear maximum intensity. However the temporal profile of the received pulse will be deformed and it can be difficult to detect the maximum intensity again in order to calculate Δt (Abshire et al., 2000).The waveform can differ in shape; if it is elongated in time, the slope of the surface can be determined. This is caused when the laser signal hitting the top of the slope will be back earlier than the laser signal hitting the bottom of the slope, for the same footprint as depicted in Figure 1.1. However this can also be caused by roughness of the terrain. To distinguish these two, the surrounding measurements, with the footprint shifted to the next location can be used. By measuring the mean height for both footprints, one can derive the difference in height. Then it is known which part of the elongated signal is caused by a slope and which part is caused by roughness. Another effect that can be measured is the reflectivity or albedo of the surface at the laser wavelength. The higher the albedo, the more energy is reflected back to the detector. When the albedo is known, something

can be said about the type of the material where the measurement was made on. Effects that also cause a range error are the electronics used to detect pulses that have a delay themselves, and the clock aboard used for timing will have a limited accuracy and will drift over time (Riris et al., 2010). Other effects are for example the path delay of the pulse (Thomas et al., 2007; Gardner, 1992).

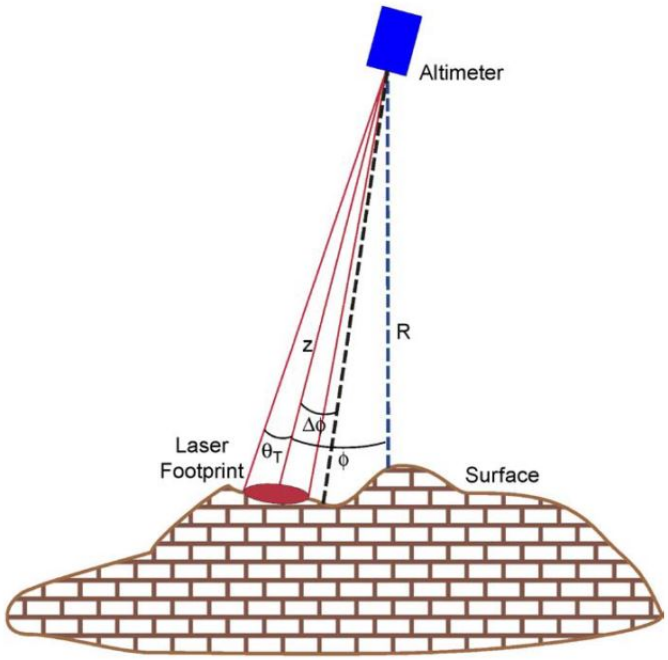

Figure 1.1: Overview of laser altimeter geometry (Thomas et al., 2007).

Another key point is the knowledge of where the laser altimeter is pointing. Typically the laser altimeter is mounted such that its line of sight is the same as the nadir axis of the spacecraft as depicted in Figure 1.1, where a typical situation with a small off-nadir is presented. Here R is the distance of the spacecraft to the surface directly below, z is the distance from the altimeter to the surface. However the off-nadir pointing angle ϕ is only known with limited accuracy $\Delta\phi$. Furthermore the laser pulse has a divergence defined by the divergence angle θ_T which is the angle where the beam intensity is $\frac{1}{e^2}$ of its maximum intensity. The diverging beam results in a laser footprint as depicted in Figure 1.1 by the red area. The final result of the laser altimeter is not the distance but the height h of the measured surface with respect to a reference R_{ref} given by (Thomas et al., 2007)

$$h = \sqrt{R^2 + z^2 - 2Rz\cos\phi} - R_{ref} \tag{1.2}$$

From the final resulting heights, a height profile can be made of the surface, which can then be matched with optical images from a camera. Together they provide much information about the surface and geological features. When multiple measurements are taken from the same area, due to cross-overs of the trajectory of the spacecraft, taking into account altitude changes of the spacecraft, the change in heights or the height profile can be measured. In this way deformations of the surface, for example caused by tides, can be measured. Note that not only the pointing knowledge is of great importance to the measurement, also the knowledge of the position of the spacecraft has a large contribution. This is done using orbit determination techniques using for example Doppler tracking.

1.1.1. Influence of pointing errors

Following the geometry in Figure 1.1, the range error δz is a function of the altitude H and the pointing error $\Delta\phi$, which shifts the footprint in horizontal direction, and the surface slope α which introduces the offset in range as given by (Steinbrügge et al., 2015)

$$\delta z \quad = \quad H\tan(\Delta\phi)\,\tan(\alpha) \tag{1.3}$$

GALA will do most of its measurements in the Ganymede Circular Orbit (GCO) 500 orbit at an altitude of 500 km. Using this height and a typical value of 5 degrees for the slope (Berquin et al., 2013; Steinbrügge et al.,

2015), Table 1.1 shows the range error caused just by the pointing error.

Table 1.1: Influence of pointing errors on range error.

	Value [arcsec]	Range error [m]
Pointing error (desired)	20	7
Pointing error (example)	100	34

Here 7 metres is set as the desirable maximum range error, corresponding to a pointing error of 20 arcsec. A pointing error of 100 arcsec corresponds already to a range error 34 metres, much more than desired. It will be shown in Section 5.1 that without calibration, the error is even much higher, requiring in-orbit calibration.

1.2. Research question, aims and objectives

Laser ranging can be used to calibrate a laser altimeter (Smith et al., 2010, 2006), however it is not clear to which extend this applies to GALA and this leads to the main question of this research:

How can interplanetary laser ranging to an Earth based ground station be used to calibrate the alignment of the GALA laser altimeter?

Here two aspects are the most important; firstly, how does a calibration of GALA look like? GALA is part of a spacecraft that has nine other instruments on board and is managed by ESA, which is therefore highly interested in the operational implications of such a calibration. Also this results in a lot of operational constraints. Furthermore, the method used for calibration can heavily influence the accuracy of it (Luthcke et al., 2000). Therefore, it is important to also develop an operational concept for the calibration, as also requested by DLR. Thus this thesis will be a practice-oriented and design-oriented research.

The second aspect is the gained improvement of the accuracy for GALA. The main focus of the calibration for GALA is measuring the misalignment, the offset between the line of sight of GALA and the nadir axis of JUICE. Improving the knowledge of this misalignment, or reducing the uncertainty of this error, will directly lead to accuracy improvements of the laser altimeter measurements. It is important to investigate how much this improvement is, how it can be influenced by the calibration and in what way the improvement can be maximised. This improvement is required to ensure successful science return and is why calibration is required.

The calibration is to be performed while JUICE is on planetary cruise to Jupiter and therefore the trajectory defines when and where a calibration campaign can be performed. This trajectory provides many options for calibration and part of this research will be devoted to find the optimal opportunities given the constrains and select the best options and a representative option to be studied in detail.

Following the above discussion, four central questions are defined as follows:

1. What is a representative laser ranging opportunity?
2. How is the calibration performed and what are the main drivers?
3. Which accuracy can be achieved by calibration?
4. What is the impact on the science performance of GALA at Ganymede of this calibration?

1.2.1. Objectives

Given the central questions and the main question, a research objective is formulated as follows.

The objective of this research is to provide a concept to improve the alignment knowledge of the Ganymede Laser Altimeter (GALA) by developing and analysing a possible laser ranging campaign during interplanetary cruise.

Sub-objectives can be formulated using the sub-questions as such:

1 Select a representative laser ranging opportunity.

Here multiple objectives and questions are investigated. What does the trajectory of JUICE look like and what are the constraints for a laser ranging campaign? Furthermore parameters that will increase the calibration accuracy are identified and discussed. From here optimal opportunities can be selected from which also a representative option is chosen.

2 Develop and simulate a laser ranging campaign calibrating the misalignment and identify its main characteristics.

Here the research goes into more detail. The link budget will be assessed and other drivers will be characterised. An operational concept is developed and finally a simulation will be created to simulate the laser ranging campaign.

3 Investigate the performance of the calibration.

The outcome of the simulation will be assessed to be able to say something about the expected improvement due to a calibration and the influence of the drivers for the calibration performance will be assessed.

4 Investigate the improvement of the science performance of GALA

Given the improvement found in the previous objective, the objective here is to see how much this will improve the science performance of GALA.

1.3. Thesis Outline

This thesis will start with an overview of the JUICE mission and the spacecraft in Chapter 2, after which the background on the tidal measurements that will be performed by GALA is discussed to get an overview of the influence of the calibration on the measurements later on. Chapter 4 will discuss the propagation of lasers, receiver and detector properties and leads to a model for the received intensity at the ground station. Also the noise sources are discussed and finally a detection scheme for the pulses is developed in this chapter. After establishing this theoretical basis on lasers, the discussion is moved towards the practical aspects of laser ranging itself in Chapter 4. GALA and other laser altimeters are discussed, as is the ground station which is a key component in this kind of laser ranging. Chapter 5 will discuss the pointing errors of influence on GALA and establish the pointing budgets. Also the pointing errors during laser ranging are discussed and translated into the development of an attitude model. Chapter 6 guides the reader through the development of the simulation tool which is verified and finally validated through the investigation of two other in-orbit calibration experiments.

As this thesis is oriented towards laser ranging with GALA, Chapter 7 investigates the trajectory of JUICE to identify possible options for laser ranging and find the most optimal opportunities where laser ranging can be achieved with an acceptable accuracy. Chapter 8 will assess to which parameters the estimation of the ground station and the calibration error are sensitive and will conclude on a calibration accuracy. The conclusion and recommendations in Chapter 9 give an overview and will discuss the goals of this thesis after which recommendations are given for further steps in reaching an actual laser ranging campaign with GALA.

2

The JUICE mission

To assure the delivery of space missions that investigate big scientific questions successfully, ESA developed a plan called the Cosmic Vision 2015-2025 programme (Bignami et al., 2005). Published in 2005, this program is the current cycle of ESA's long term planning for space missions succeeding the Horizon 2000 program. Here the main science questions are selected and a way to select and implement missions is outlined taking into account the current status of technology and expected developments. This programme provides long term stability for missions as they can take more then twenty years for their development and operations. For example the Cassini/Huygens mission, of which the Huygens probe was developed by ESA started development in the 1980s and the probe landed finally in 2004 (Lebreton et al., 2005) while Cassini is still in operation even till September 2017.

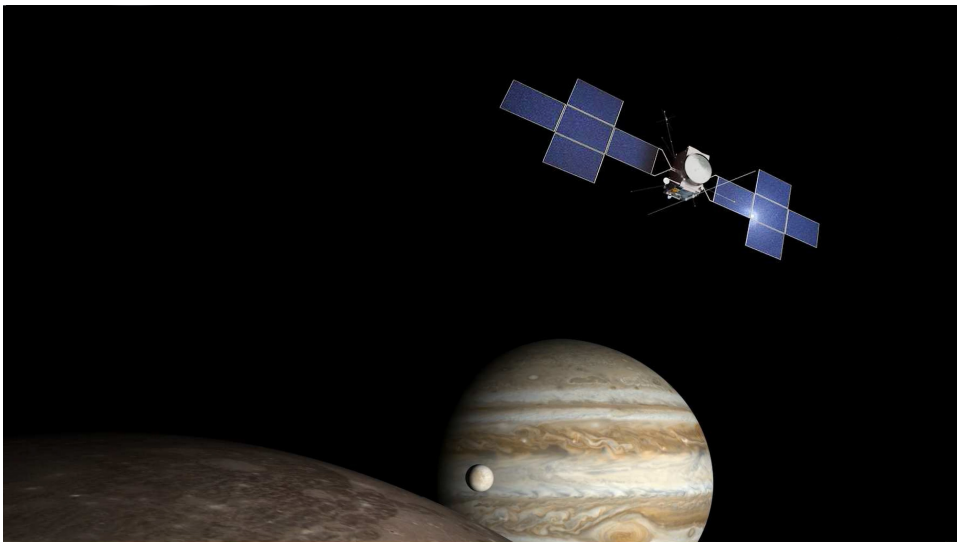

Figure 2.1: Artist impression of JUICE. (Airbus Defence and Space, 2016).

In correspondence with the scientific community the main science drivers are grouped in four themes:

- Theme 1. What are the conditions for planet formation and the emergence of life?
- Theme 2. How does the Solar System work?
- Theme 3. What are the fundamental physical laws of the Universe?
- Theme 4. How did the Universe originate and what is it made of?

2.1. JUICE

The JUICE mission is the first L-class (large) European Space Agency (ESA) mission within its Cosmic Vision Programme and envisioned to answer large questions about the solar system and its planets and moons focussing on the first two themes of the Cosmic Vision programme. As such, the JUICE mission is centred around its main theme as defined in the Definition Study Report, or informally the JUICE Red Book (European Space Agency (ESA), 2014):

The emergence of habitable worlds around gas giants.

It is known that on Earth, life can develop and evolve even under the most harsh conditions. This makes scientist wonder if Earth is the only place where life exists and which conditions are required for life. To see if life would be present somewhere else it is important to see what the conditions in other place then Earth are like, both within and outside of the Solar System. JUICE aims at addressing both situations by investigating if, within the Solar System, the necessary conditions for life are present. It does this by studying the moons of Jupiter but also takes a closer look at Jupiter itself. Jupiter serves as a archetype for gas giants that are now found around other stars, potentially also providing conditions for life to exist. This is how JUICE also aims at investigating potential life out of the Solar System. To summarise, two main goals for JUICE are presented with its sub objectives (European Space Agency (ESA), 2014).

- Characterise Ganymede, Europa and Callisto as planetary objects and potential habitats
  - Ganymede as a planetary object and possible habitat
  - Europa's recently active zones
  - Callisto as a remnant of the early Jovian system
- Explore the Jupiter system as an archetype for gas giants
  - The Jovian atmosphere
  - The Jovian magnetosphere
  - The Jovian satellite and ring systems

Although JUICE will study the entire Jovian satellite system, an emphasis is placed on Ganymede, Europa and Callisto, although not in the same detail. These three are selected as all of them are potentially or known ocean-bearing worlds (Hussmann H et al., 2006). Water is seen as the minimum requirement for habitability (Kasting et al., 1993), and although this does not mean that life has actually existed on these worlds, these are potentially habitable, as required by the goals for JUICE. Not only the search for oceans is interesting, also the evolution of the surface and the composition of the satellites is of interest, as is the interaction with the Jovian magnetosphere. Using the same instruments, also the atmosphere of Jupiter can be studied, complimenting the on-going Juno mission, studying its chemistry, composition and structure (Yelle and Miller, 2004). The Jovian magnetosphere influences heavily the entire Jovian satellite environment (Mauk et al., 2004) and is thus an important object to study, as is the interaction of this magnetic field with the Jovian satellite and ring system.

2.1.1. Mission overview

The mission of JUICE can be divided in two phases, firstly there is the interplanetary transfer phase, where JUICE will have flybys of Venus, Earth and Mars. Secondly there is the science phase where JUICE will orbit Jupiter, followed by a transfer to Ganymede and finally a phase where the spacecraft orbits Ganymede. The trajectory is designed such that there is enough time to send data to Earth and be able to meet the science goals while also minimise radiation from the environment of Jupiter, which is known for its harsh radiation conditions. Launching in 2022 the planetary cruise will take 7.4 years while the science phase will take around 3 years to complete (European Space Agency (ESA), 2014).

Note that originally a circular orbit around Ganymede at 200 km was also planned. However due to Δv constraints, this was scrapped from the mission profile. If a more completed design or Δv savings would allow again for such a phase, it will be added, improving the science that can be performed. For example the resolution of the measurements of GALA would increase, however adding more phases to the mission will also put more stress on the radiation hardness of the spacecraft design.

Table 2.1: Mission phases for JUICE (European Space Agency (ESA), 2014)

Phase		Duration
Interplanetary Cruise		7.4 years
Nominal science phase		3.4 years
	Jupiter equatorial phase 1 and transfer to Callisto	12 months
	Europa flybys	1 month
	Jupiter high inclination orbit and Callisto flybys	6 months
	Jupiter equatorial phase 2 and transfer to Ganymede	9 months
	Ganymede Phase	9.5 months
	1st elliptical phase	
	High altitude circular orbit at 5000 km (GCO-5000)	
	2nd elliptical phase	
	Low altitude circular orbit at 500 km (GCO-500)	

2.1.2. Spacecraft Design

The main drivers for the design of JUICE are the large distance to the Sun, the choice of using solar power and the harsh radiation environment around Jupiter. As seen from Table 2.1 JUICE will also perform a large amount of manoeuvres requiring a large Δv capability. This results in a fairly large spacecraft with a dry mass of around 1800 kg and a wet mass of around 4800 kg. Furthermore, large solar panels are required due to the large distance, and also a high gain antenna is required for data transmission. A baseline data rate of 48 kbps, resulting in 1.4 Gb of data per day is one of the main limitations for instruments to perform science, as most instruments can generate much more data than that can be transmitted back to Earth (European Space Agency (ESA), 2014). Damage due to the radiation environment around Jupiter is mitigated in multiple ways. Firstly the trajectory is designed with highly elliptical orbits, placing the spacecraft out of the harshest radiation for long times. Furthermore, the spacecraft design includes a radiation vault, an area heavily shielded from radiation where most electronics will be installed to provide them shielding. A preliminary design is depicted in Figure 2.2.

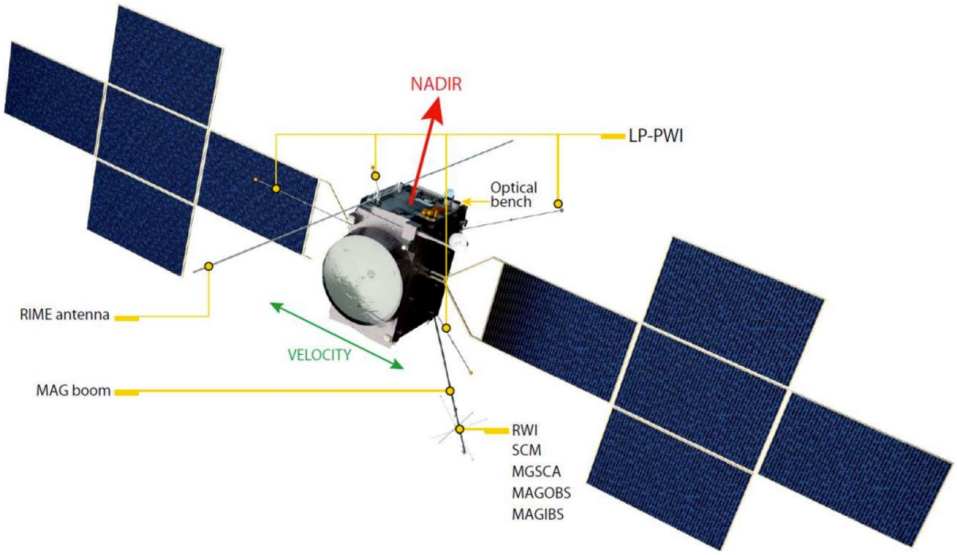

Figure 2.2: Proposed spacecraft design for JUICE (Credit: Airbus DS).

2.2. Ganymede

The focus of the JUICE and GALA mission will lie on Ganymede which is the largest moon in the solar system and visited six times by the Galileo Orbiter studying the moon and taking pictures as in Figure 2.3.

Figure 2.3: Picture of Ganymede taken by the Galileo spacecraft (NASA/JPL, 1998).

As seen in Figure 2.3, the surface of Ganymede features around 40% of dark terrain while the rest of the terrain is more bright with relatively low crater density (Showman and Malhotra, 1999). The surface is mainly covered by ice while its density is measured at 1940 kg/m^3, between the densities of silicates and water (Hussmann et al., 2015). Being an icy moon, these class of bodies evolved differently compared to other bodies such as planets due to tidal energy sources, different temperatures and compositions (Prockter et al., 2010) and studies of the surface features have been performed (Prockter et al., 2000) using the images taken by Voyager 2 and later by the Galileo spacecraft (Belton et al., 1996). (Prockter et al., 1998) concluded that the dark terrain may be formed by non-water contaminants caused by sublimation and mass wasting. The bright terrains are caused by resurfacing due to tectonism (Pappalardo et al., 1998), causing much of the surface to be heavily deformed and grooved.

Ganymede is the only moon in the solar system where an intrinsic magnetic field has been discovered (Kivelson et al., 1996). This can be explained by a liquid metal core, like on Earth, estimated to be around 200 km in thickness (Kivelson et al., 2002). Above the metallic core, a layer of silicates is expected above which an ice-layer should be present (Hussmann et al., 2015). However the magnetic field measured by the Galileo spacecraft cannot be fully explained by the intrinsic magnetic field, therefore Ganymede should also have an induced magnetic field (Kivelson et al., 2002). This field is caused by an ocean layer on top, and above this ocean there is another ice layer, the surface that can be seen (Collins and Johnson, 2014). Several studies on this ice and ocean structure have been performed e.g. (Vance et al., 2014), and here JUICE will perform measurements to constrain the ice shell and ocean thicknesses and further improve the understanding of the interior structure.

The ice shell can deform much more in the presence of an ocean as concluded by (Moore and Schubert, 2003). There it was determined that without an ocean, the deformation of the surface due to tides is less than 0.5 meter, while with a subsurface ocean present, the deformation of the upper ice layer is around 7 meters, detectable by GALA (Steinbrügge et al., 2015). The subsurface ocean was also detected by observing the aurora of Ganymede since it is governed by the magnetic field, variations caused by the induced magnetic field should be visible in the aurora. This is indeed observed using the Hubble Space Telescope (Saur et al., 2015), further confirming the existence of the sub surface ocean.

One of the main topics for JUICE and GALA is characterising the thicknesses of the subsurface ocean and the ice shell by measuring the first Love number h_2 which describes the radial displacement at the surface of

the body u_r, under influence of a tidal potential Φ; (Love, 1911)

$$h_2 = \frac{g u_r}{\Phi} \tag{2.1}$$

Here g is the gravitational acceleration $\frac{GM}{R^2}$ with M as the mass of the body and R its radius. h_2 will be zero when the body does not deform at all and thus provides a measure to determine how deformable a body is, or how it resists tidal forcing.

Figure 2.4 shows how this fits in the bigger picture for determining the thickness of the ocean and ice shell where the ocean thickness and top ice shell thickness are shown with constrains plotted on top of each other. The first constraint is set by the melting curve for ice. This depends on pressure, temperature and composition of the ice, e.g. the stability of ice differs with pressure, which will be different for a different ice thickness. Since also the temperature and composition of the ice is not know, this melting curve is not a line but a region. The libration amplitude is caused partly by the density contrast between the ice shell and ocean and thus sets also a constrain, as does the measurement of the magnetic induction, determining the electrical conductivity of the ocean (Grasset et al., 2013).

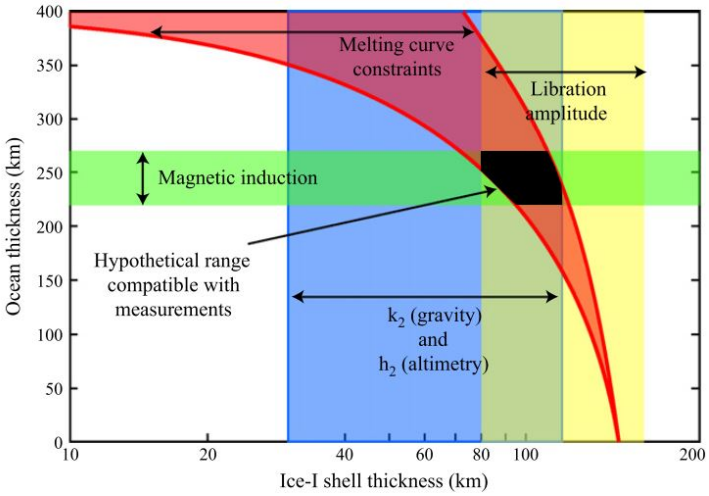

Figure 2.4: Constraints on the thickness of the Ocean and Ice shell (Grasset et al., 2013).

Finally the rigidity of the ice, governed by its thickness, is determined by measuring the two love numbers k_2 and h_2, resulting in the bounded black area with possible thicknesses for the ocean and the ice shell. GALA will contribute to the measurement of h_2 by measuring the radial displacement as given in Equation 2.2. This is done using crossovers where two or more times a measurement is taken from the same spot at different times, t_1 and t_2 in Equation 2.3.

$$u_r = \frac{h_2 \Phi(r,\theta,\phi,t)}{g} \tag{2.2}$$

$$du = \frac{h_2}{g}\left(\Phi_1(r,\theta,\phi,t_1) - \Phi_2(r,\theta,\phi,t_2)\right) + dr_{n1} - dr_{n2} \tag{2.3}$$

Here du is the difference between two measurements and since tidal models exist to compute the tidal potentials Φ_1 and Φ_2 (Moore and Schubert, 2003; Hussmann et al., 2011), it is possible to determine h_2. dr_{n1} and dr_{n2} are the errors of the two measurements, consisting of orbit errors, range errors and pointing errors. It is the contribution of the pointing error to this term that this study aims to reduce, improving the determination accuracy of h_2, leading to a better estimation of the thickness of the ice shell and sub surface ocean.

3

Link Budget

When looking at a laser beam in daily life the beam appears as an infinite line with a constant thickness resulting in a very small point when it hits a surface. One can use it to point at a lecture slide or cut through materials since all energy is concentrated in a very small point. However when lasers are introduced into a space environment, propagation distances become large and the laser beam appears not so perfect as before. Even laser beams start to spread their energy over a certain area and lose their energy when propagating through an atmosphere. In order to analyse laser ranging with GALA a quantification of the received signal is required for the subsequent analysis and to see if laser ranging is possible at all. Often coined as the link budget, the goal of this chapter is to establish a model for the incoming signal at the ground station. Rather than just a final number, often the result of al link budget calculation, a more sophisticated approach is used incorporating the signal shape and the noise that is encountered in real laser ranging. Section 3.1 will elaborate on laser beams travelling through free space and an atmosphere after which the other end of the link, the receiver will be treated in Section 3.2, resulting in a total link budget in Section 3.3. Section 3.4 treats the different noise sources and the discussion is moved towards discriminating the signal from the noise in Section 3.5 through a detection method suitable for the envisioned experiment.

3.1. Laser Beams

GALA's laser pulses are generated by an active Q-switched Nd:Yag laser (Lingenauber et al., 2013), meaning that the laser consists of a neodymium-doped yttrium aluminium garnet crystal inside an optical resonator. The electrons in the crystal are pumped into a higher energy level, a process that builds up until the energy is released in the form of a short laser pulse. The release of the laser energy is done at a certain frequency and is a common technique employed for lasers named Q-switching (Siegman, 1986). For GALA a laser pulse of 25 mJ is created with a 1-sigma width of 2.9 ns at a frequency, which is the pulse repetition rate, of 30 Hz with a wavelength of 1064 nm (Lingenauber et al., 2013).

The energy of a photon E_p at 1064 nm is given by Equation 3.1 and with a given total energy of the laser pulse the number of outgoing photons n_T is given in as shown in Equation 3.2. Here c is the speed of light, h is the Planck constant and E_T is the total pulse energy as it leaves the transmitter. For GALA, assuming an energy of 25 mJ, n_T lies around $1.34 \cdot 10^{17}$ photons per pulse.

$$E_p = \frac{hc}{\lambda} \tag{3.1}$$

$$n_T = \frac{E_T \lambda}{hc} \tag{3.2}$$

The spatial intensity profile can be approximated by a Gaussian beam for most lasers (Siegman, 1986) and this is also the case for GALA in the far field. A Gaussian beam in this case is characterised by the beam waist radius w_0 and the wavelength. Such a beam is visualised in Figure 3.1 where the beam propagates in the z+ direction, diverging with the divergence angle θ, which is usually used to characterised a laser beam. Here the divergence angle is the half cone angle denoted as $\theta_{\frac{1}{2}}$ from now on, while θ_T is used for the full cone divergence angle. At this angle, the intensity is decreased to $\frac{1}{e^2}$ with respect to its peak intensity in the middle and lies for GALA at a value of 50 μrad or 10.3 arc seconds.

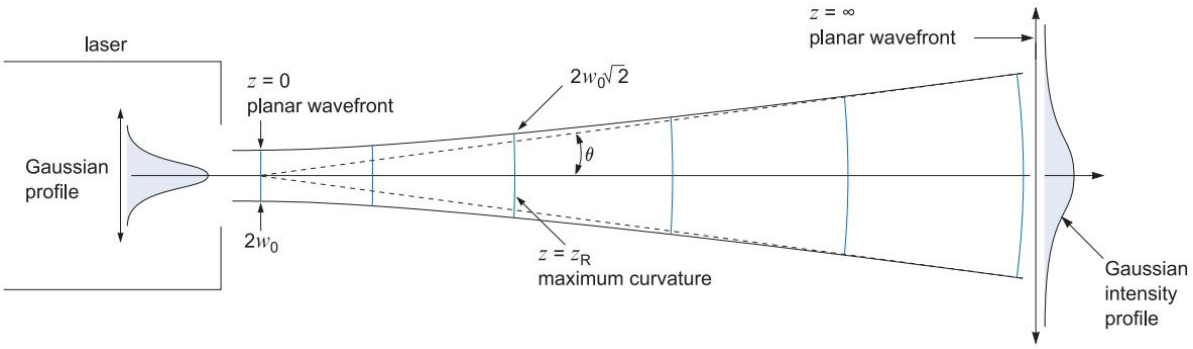

Figure 3.1: Gaussian beam spatial intensity profile in the far field (IDEX Optics and Photonics, 2016).

3.1.1. Free Space Propagation

As the laser beam propagates through free space, it's intensity profile in the far field can be approximated through Equations 3.3 and 3.4 and $\theta_{\frac{1}{2}}$ is indeed incorporated through Equation 3.5. This approximation holds for the intensity profile in the far field with small divergence angles (Siegman, 1986).

$$I(r,z) = I_0\left(\frac{w_0}{w(z)}\right)^2 \exp\left(-2\frac{r^2}{w(z)^2}\right) \tag{3.3}$$

$$w(z) = w_0\sqrt{1+\left(\frac{\lambda z}{\pi w_0}\right)^2} \approx \frac{\lambda z}{\pi w_0} \tag{3.4}$$

$$\theta_{\frac{1}{2}} = \frac{\lambda}{\pi w_0} \tag{3.5}$$

The importance of this equation in this study lies in the dependency of the intensity on the radial distance r from the midpoint of the beam. As the focus of this study lies on large distances, the laser spot size w will range from 50 meters in Ganymede orbit, to thousands of kilometres during the proposed laser ranging at large distances from Earth where it is highly likely that the receiving ground station will not be near the midpoint but somewhere else in the beam spot. Using Equation 3.5 and the value of 10.3 arcsec for GALA's $\theta_{\frac{1}{2}}$, the beam waist at z=0, w_0, is 6.7 cm. I_0 is the intensity expressed in photons per square meter at the midpoint of the beam for r and z both zero, while the total amount of photons, spread over the entire footprint of the beam, is equal to n_T. Thus if Equation 3.3 is integrated using polar coordinates where z is set to 0 as shown in Equation 3.6, the total number of photons n_{total} in a spot with radius r inside the beam is given by Equation 3.7.

$$n_{total} = \int_0^r \int_0^{2\pi} I_0\left(\frac{w_0}{w_0}\right)^2 \exp\left(-2\frac{r^2}{w_0^2}\right) d\theta r dr \tag{3.6}$$

$$n_{total}(r) = I_0\frac{\pi w_0^2}{2}\left(1-\exp\left(-2\frac{r^2}{w(z)^2}\right)\right) \tag{3.7}$$

Setting r to infinity to capture all the photons of the pulse as in Equation 3.8 leads to an expression for I_0 in Equation 3.9 which will be used in following calculations.

$$n_{total}(\infty) = I_0\frac{\pi w_0^2}{2} \tag{3.8}$$

$$I_0 = n_T\frac{2}{\pi w_0^2} \tag{3.9}$$

An example intensity profile of GALA at a distance of 0.2 AU is shown in Figure 3.2 both showing the distance from the midpoint as the deviation from the midpoint in arc seconds. The $\frac{1}{e^2}$ is around 1500 km or 10.3 arc seconds and as can be seen, beyond this point there are still photons present.

3.1.2. Atmospheric Propagation

After the pulse propagates through the vacuum of space, it will travel its final part to the ground station through Earth's atmosphere, influencing the pulse propagation in several ways. It will delay the propagation

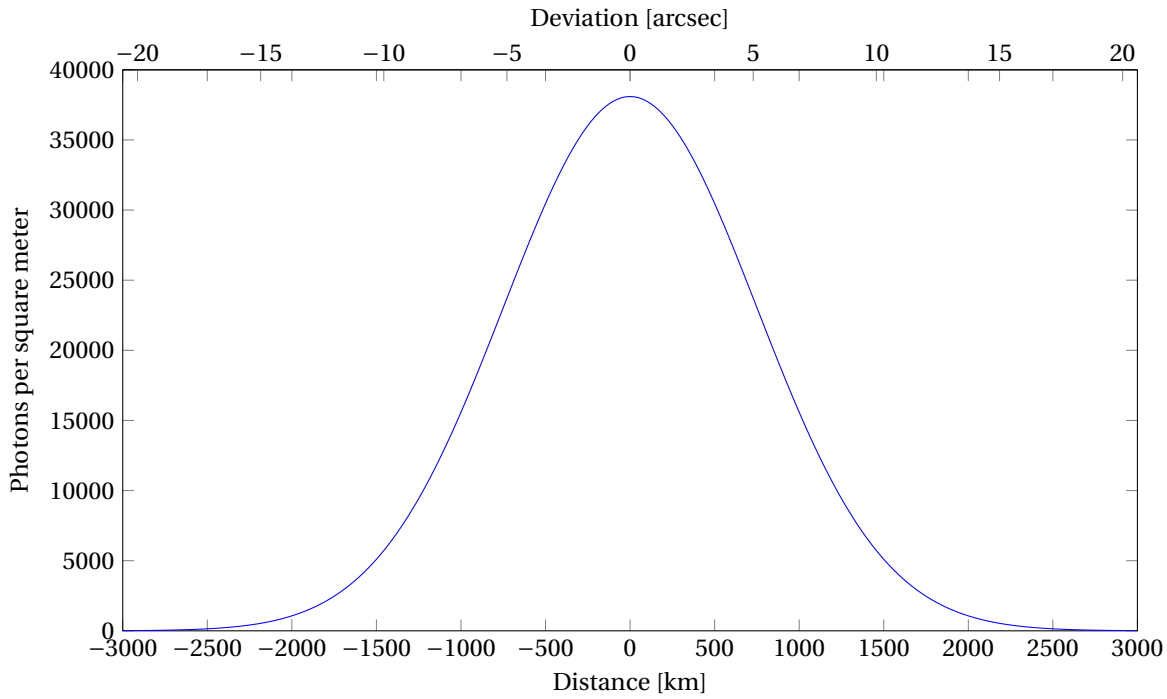

Figure 3.2: Intensity profile for the GALA laser at a distance of 0.2 AU.

due to the fact that the light travels slower than in a vacuum and it will bend the path of the light, delaying the signal even further (Degnan, 1993). These effects represent one of the main challenges in laser ranging and are extensively studied and can be modelled by assuming different layers for the entire Earth as employed by (Marini and Murray, C. W., 1973). Here the air density, temperature and humidity are measured at the ground station for calculating the influence on the signal. This holds especially for the range error in the signal. This method in combination with the method employed by (Mendes and Pavlis, 2004) where the zenith delay is predicted, is standard practice for any laser ground station and leads to accuracies in the order of millimetres. These layers can also cause the beam to spread and wander but the influence for a downlink is negligible and thus are not considered in this study (Dirkx et al., 2014a).

However the atmosphere also influences the intensity of the signal due to atmospheric attenuation (Degnan, 1993). This effect plays an important role in establishing the link budget or signal intensity at ground and is expressed by an one-way transmission coefficient T in Equation 3.10 where a straight path is assumed for the laser pulse.

$$T(\lambda_t, V, h_t) = \exp\left(-\frac{1}{\cos\theta_z}\int_{h_t}^{\infty}\sigma_{atm}(\lambda_t, V, h)dh\right) \tag{3.10}$$

$$T_{atmos} = T^{\frac{1}{\cos\theta_z}} \tag{3.11}$$

Here λ_t is the wavelength of the signal, V the visibility, h_t is the height of the ground station, θ_z the zenith angle (90° - elevation) and σ_{atm} the attenuation coefficient. This coefficient can be modelled in various ways which are deemed out of the scope of this thesis. Instead one value for T_{atmos} will be assumed which is than only influenced by the zenith angle as in Equation 3.11 where T is the transmission with a zenith angle of zero degrees. This value corresponds to a certain visibility and the wavelength used by GALA at 1064 nm as visualised in Figures 3.3 and 3.4.

Figure 3.3 shows the transmission over the typical wavelengths for laser ranging where it can be seen that for a clear dry air without aerosols, T is 0.94, which is identified as the best case. This Figure also clearly shows absorption bands for other wavelengths while these are absent in Figure 3.4 however here T^2 is found to be 0.4 for light haze, which is the worst case in absence of clouds and corresponds to a T of 0.6. This value for T will be used throughout this study.

In the presence of large, visible clouds the laser signal is blocked but also cirrus clouds are of big impact for laser ranging and is experimentally found to follow Equation 3.12 (Degnan, 1993). These clouds are not

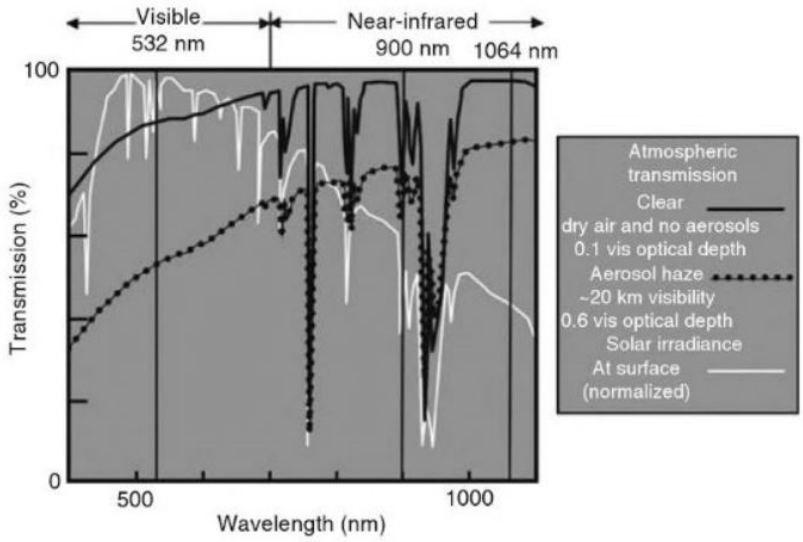

Figure 3.3: Transmission coefficients for different conditions as used in LIDAR (Jie and Toth, 2008).

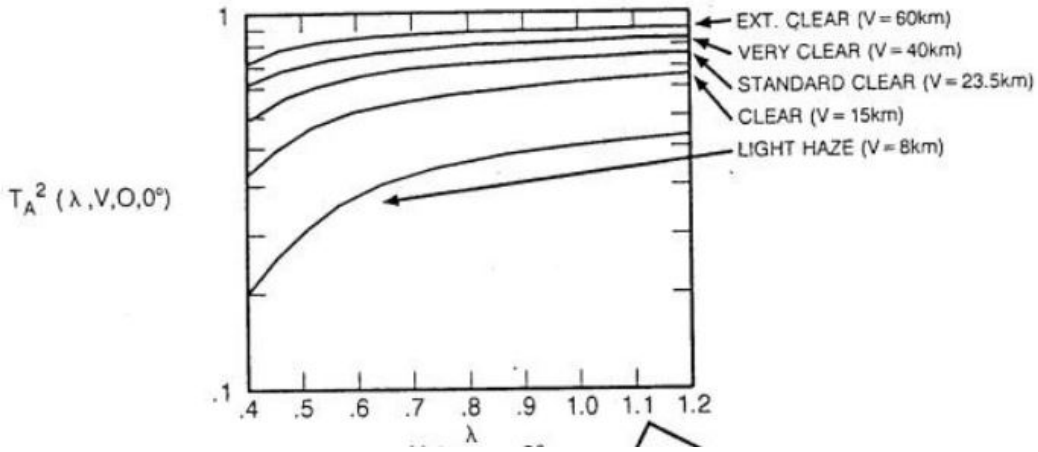

Figure 3.4: Two-way transmission coefficients for different visibilities. (Degnan, 1993).

always visible but are typically present 50% of the time above a ground station.

$$T_c = \exp(-0.14(t \sec\theta_z)^2) \tag{3.12}$$

Here T_c is the transmission introduced by the cirrus clouds and t is their thickness. For the calculation of T_c the mean thickness of 1.3 kilometres will be used (Degnan, 1993).

So finally the total transmission coefficient T_{total} is a combination of both Equation 3.11 and 3.12 as given in Equation 3.13.

$$T_{total} = T_{atmos} \cdot T_c = T^{\sec\theta_z} \cdot \exp(-0.14(t \sec\theta_z)^2) \tag{3.13}$$

3.2. Receiver Properties

When the laser pulse has travelled through the atmosphere it will be received by a ground station. A ground station captures the laser pulse through a telescope and then the light will be focused and passed on to the detector through typically 25 lenses. This is a typical number for ground stations such as at Wettzell (Schreiber, 2017). Each lens has a typical throughput efficiency of 0.98 and the telescope itself also has an efficiency. A typical value for the efficiency of the receiver η_r for the entire path of the laser pulse is 0.2 - 0.5 (IRLS, 2017; Schreiber, 2017).

One of the other causes of the reduced efficiency at the ground station is the use of a spectral filter. This filter will filter out light with other wavelengths than that of the laser pulse. This greatly reduces the noise which would otherwise be caused by photons with other wavelengths. Therefore this is an unavoidable property of the receiver and will be discussed further in Section 3.4 on noise. Discussing filters and their influence on the throughput efficiency is out of the scope of this study and thus the efficiencies of the telescope as mentioned above will be used for calculations.

3.2.1. Avalanche Photodiodes

In order to detect the incoming laser pulse, several types of detectors can be used including Photomultiplier Tubes (PMTs) and Avalanche Photodiode (APD)s. The APD is widely used in laser ranging and is a semiconductor photo detector using the photoelectric effect that produces a small current when photons hit the detector surface. Then, by using a high reverse voltage, an electron avalanche is created which acts as an internal gain, producing a measurable current. When the reverse voltage is raised just above the breakdown voltage, the APD works in the so called Geiger mode and is named a Single-photon Avalanche Photodiode (SAPD). The breakdown voltage is the voltage where the insulator becomes conductive and the hit of a single photon will now cause a self sustaining avalanche. When photons hit the detector, not all photons will be converted to a current and the ratio between incoming signal and produced current is a typical parameter for detectors. This quantum efficiency is shown in Figure 3.5 for a typical silicon APD with respect to the wavelength of the incoming signal.

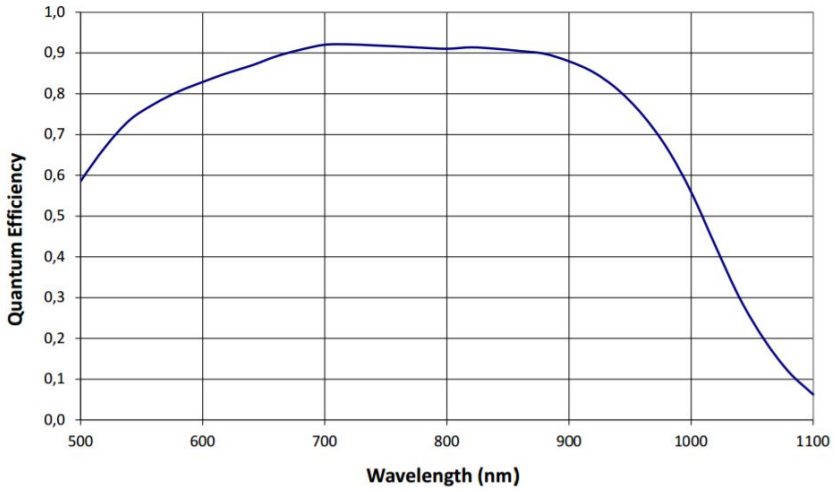

Figure 3.5: Quantum efficiency for a typical APD as used in laser ground stations (Laser Components, 2017).

It can clearly be seen that, while efficiency is fairly high for wavelengths from 700 to 900 nm, the efficiency for 1064 nm is around 0.2, a large reduction. Silicon APDs are the most widely used APDs but other types like Germanium and InGaAs APDs also exist, featuring better efficiencies at other wavelengths. As a worst case value for the quantum efficiency, 0.2 will be used, also used in the Hayabusa experiment Noda et al. (2016).

A typical InGaAs APD used for 1064 nm ranging at Wettzell offers a quantum efficiency of around 0.7 and thus this value will be used as the best case quantum efficiency (Princeton Lightwave, 2010). However the internal gain created by the high voltage as discussed is much lower for InGaAs APDs. Where silicon APDs have an internal gain of 50 to 500, InGaAs APDs typically have a gain of 10 (Perkin Elmer, 2003), meaning that the output voltage is lower, making it more difficult to detect low photon intensities.

3.3. Total Link Budget

In order to determine whether or not a laser pulse can be received by the ground station, the number of photons that are detected, or photoelectrons, can be evaluated using the link budget equation starting with

Equations 3.14 and 3.15 (Degnan, 2002a).

$$n_s^B = \frac{C_{AB} E_A A_b}{R^2} \tag{3.14}$$

$$C_{AB} = \frac{\eta_q^B \eta_r^B T_A^{\sec(\theta_A)} T_B^{\sec(\theta_B)}}{h\nu \Omega_t^A} \tag{3.15}$$

$$n_s^B = \frac{E_A}{h\nu} \frac{A_b}{\Omega_t^A} T_A^{\sec(\theta_A)} T_B^{\sec(\theta_B)} \eta_q^B \eta_r^B \tag{3.16}$$

$$\Omega_t^A = \frac{A_T}{R^2} \tag{3.17}$$

These Equations are reordered and put together for clarity in Equation 3.16 which will be modified to suit the laser ranging for GALA, resulting in Equation 3.18. The first term $\frac{E_A}{h\nu}$, where h is again Planck's constant while ν is the frequency of the photon, is the same as Equation 3.2 and is the amount of photons sent out by the transmitter n_T which will be used in 3.18. The next term $\frac{A_b}{\Omega_t^A}$ determines the amount of photons receivable by the receiver telescope area A_b and the footprint size of the laser beam through the solid angle Ω_t^A given by Equation 3.17. However, now $I(r,z)$ from Equation 3.3 will be used, which gives the amount of photons per square metre. This is multiplied by the area of the receiver A_r as seen in Equation 3.18. This signal is then reduced by the atmosphere and this reduction depends on the elevation or zenith angle of JUICE θ_J . Equation 3.16 states this two times as T_A and T_B, but in case of laser ranging from a satellite in vacuum to Earth the pulse only travels once through the atmosphere and T_{total} from Equation 3.13 is used instead using the zenith angle of JUICE θ_J as its input. Finally the efficiencies of the receiver telescope and APD are included as η_r and η_q respectively and the efficiency of the transmitting telescope as η_t.

$$n_r = I(r,z) A_r \; T_{total}(\theta_J) \; \eta_t \eta_r \eta_q \tag{3.18}$$

The result is the mean number of detectable photons, or photoelectrons, at the receiver n_r in Equation 3.18. However, due to the nature of the process that creates the laser pulse, this number is the mean expected number of photons (Murphy, 2001; Dirkx et al., 2014a). The uncertainty in the number of detected photons is modelled using Poisson statistics using the probability mass function as given by

$$P(N_s) = \frac{n_r^{N_s}}{N_s!} e^{-n_r} \tag{3.19}$$

Here N_s is the number of photoelectrons detected and n_r is the mean number of expected detectable photons per pulse from Equation 3.18. This effect becomes especially important when the photons counts become low in the 1-10 range as it will govern whether or not the pulse is above the threshold and detected. So even if the mean number of photons is above the threshold, it can be the case that it is not detected and vice versa.

3.4. Noise

During laser ranging, the receiver will also detect photons, noise, not originating from the laser pulse and produced by various sources. Instrument noise and stellar background noise are always present under any condition, contrary to noise from the Sun by direct illumination of the receiver and through atmospheric scattering, both only present during daytime ranging. For GALA looking to Earth, also the reflected sunlight by Earth's atmosphere and surface will cause noise in the detector. The last source is backscatter noise produced when a laser pulse is sent out by the transmitter and also clouds can deflect the signal back to the receiver, introducing false detections at the ground station (Degnan, 2002a).

3.4.1. Laser Backscatter

Backscatter noise is caused by the scattering atmosphere that reflects some photons of the pulse that is sent out by the transmitter, back to the receiver. It is assumed that during laser ranging operations, a two way laser link is the goal of the experiment and thus GALA and the ground station will be firing laser pulses at each other. Thus, when photons sent out by GALA arrive at the ground station, it is possible that a pulse has just been sent out by the ground station and thus creating backscatter noise at the same time as the pulse from GALA should be detected. This is especially the case for monostatic systems where the outgoing pulse is

using the same telescope to transmit as it uses to receive photons. This is the case for many ground stations such as Wettzell but does not hold for GALA as GALA uses separate telescopes for transmitting and receiving pulses. Furthermore, GALA is not operating in an atmosphere so this noise only holds for the ground station and can be described by Equation (Degnan, 2002a) which is a function of the time since the outgoing laser pulse was sent.

$$n_{bs}(\tau) = \frac{\eta_q \eta_r A_r}{2\pi h\nu} \frac{E_T}{h_{sc} c} \left[\ln\left(\frac{1}{T}\right) T^{\sec\theta_J \left[1-\exp\left(-\frac{c\tau}{2h_{sc}\sec\theta_J}\right)\right]} \right] \left(\frac{\exp\left(-\frac{c\tau}{2h_{sc}\sec\theta_J}\right)}{\tau^2} \right) \tag{3.20}$$

$$\tau = \frac{2s}{c} = \frac{2\sec\theta_J}{c}(z - h_s) \tag{3.21}$$

Here τ is expressed in Equation 3.21, and represents the time since the laser pulse is sent out as this is 2 times the distance z to the scattering volume, divided by speed of light$c$. θ_J is the zenith angle of JUICE as seen from the ground station, z the altitude of the scattering volume and h_{sc} the atmospheric scale height, used to model the atmosphere. T is the transmission coefficient for the atmosphere causing the scattering and $\eta_q \eta_r A_r E_T$ characterises the ground station by its efficiencies, telescope area and laser pulse energy.

Through Equation 3.21 it can be seen that the backscatter noise reduces quickly with time since the laser pulse was sent. In the case of the laser ground station at Wettzell, the pulse is sent out by a rotating mirror, which blocks incoming signal just after sending out the laser pulse. Thus, no immediate backscatter is received and any backscatter noise afterwards will be very low. Furthermore, the noise is significant for 100 microseconds per shot (Degnan, 2002a), which would sum up to 0.3% of the time when operating at 30 Hz. For these reasons, it is decided not to incorporate this noise in this study.

3.4.2. Solar Noise

Solar noise comes in four ways to a detector, direct illumination, as stray light, through atmospheric scattering or through reflection from a planet into the detector. Operational rules prevent a ground station like Wettzell to have a angular separation between the Sun and the target of lower than 20 degrees. Thus no direct illumination is possible and this restriction also holds for the receiver at GALA. Furthermore, it is assumed that the receivers are equipped with a baffle that rejects stray light. Since the angular separation has a limit, it is assumed that no significant stray light reaches the detector with larger angular separations. Although the baffle for GALA is still under development this is a safe assumption according to the studies performed for this design (Wegert, 2016).

Sun light can still reach the detector through atmospheric scattering which can be approximated by Equation 3.22 (Degnan, 2002a) where $\eta_q \eta_r A_r \Omega_r$ again characterise the receiver where Ω_r is the receiver field of view. $\Delta\lambda$ is the bandwidth of the spectral filter at the receiver and N_λ is the solar irradiance at Earth, which is 0.64621 W/m^2/nm at the 1064 nm wavelength. The atmosphere is modelled as one uniform atmosphere and shows up only through the transmission coefficient T which is the same as in equation 3.11.

$$n_{ls} = \frac{\eta_q \eta_r N_\lambda(\Delta\lambda) A_r \Omega_r}{4\pi h\nu} \left[\sec\theta_J T^{\sec\theta_J} \left(\frac{1 - T^{\sec\theta_S - \sec\theta_J}}{\sec\theta_S - \sec\theta_J} \right) \right] \tag{3.22}$$

Here θ_S and θ_J are the zenith angles of the Sun and JUICE respectively and their separation determines the noise level. However, when the zenith angles become the same, Equation 3.23 approximates the level of noise due to scattering. This is a likely case since the elevations of Sun and JUICE will increase and decrease due to the rotation of the Earth but will not do this synchronised. Thus the elevations will cross each other twice a day. Note that this does not mean that the angular separation is close to zero, only the zenith or elevation angles of the two are the same, but the azimuth angle can be very different. The atmospheric scattering here does not include the distribution of scatter with altitude and no horizontal gradients are taken into account. It therefore only depends on the zenith angle, and not on the azimuth angle, the noise is uniform and the same from any direction. Section 6.3 will present the solar noise from atmospheric scattering in Figure 6.8.

$$n_{ls} = \frac{\eta_q \eta_r N_\lambda(\Delta\lambda) A_r \Omega_r}{4\pi h\nu} \left(T^{\sec\theta_J} \ln T^{\sec\theta_J} \right) \tag{3.23}$$

A significant noise contribution for GALA will be the reflected sunlight by the Earth's surface and atmosphere if the Earth is not dark as seen from GALA and is approximated by: (Degnan, 2002a)

$$n_{sa} \cong \frac{\eta_q \eta_r N_\lambda \Delta\lambda A_r r^2}{h\nu R^2}\left(\rho g_{ps}(\alpha) + \frac{1}{2}\ln\left(\frac{1}{T}\right) g_{as}(\alpha)\right) \tag{3.24}$$

Here r is the volumetric radius of Earth, R is the distance from JUICE to the Earth, ρ is the reflectivity at 1064 nm and α is the angle between JUICE and the Sun at Earth and determines how much light is reflected using the geometry. g_{as} governs the light reflected by a thin atmosphere, compared to the entire volume, and g_{ps} governs the light reflected by the surface. This is described in Equations 3.25 to 3.28 where a the planet is modelled as a sphere and bending of light is not taken into account (Degnan, 2002a).

$$g_{ps}(0 \le \alpha \le \frac{\pi}{2}) = \cos^2\alpha + \frac{2}{\pi}\int_{|\cos\alpha|}^{1} x\cos^{-1}\left(-\cot\alpha\left(\frac{\sqrt{1-x^2}}{x}\right)\right)dx \tag{3.25}$$

$$g_{ps}(\frac{\pi}{2} \le \alpha \le \pi) = \frac{2}{\pi}\int_{\cos\alpha}^{1} x\cos^{-1}\left(-\cot\alpha\left(\frac{\sqrt{1-x^2}}{x}\right)\right)dx \tag{3.26}$$

$$g_{as}(0 \le \alpha \le \frac{\pi}{2}) = 1 - \sin\alpha + \frac{1}{\pi}\int_{0}^{\sin\alpha} \cos^{-1}\left(-\cot\alpha\left(\frac{x}{\sqrt{1-x^2}}\right)\right)dx \tag{3.27}$$

$$g_{as}(\frac{\pi}{2} \le \alpha \le \pi) = \frac{1}{\pi}\int_{0}^{\sin\alpha} \cos^{-1}\left(-\cot\alpha\left(\frac{x}{\sqrt{1-x^2}}\right)\right)dx \tag{3.28}$$

3.4.3. Dark Noise

Dark noise is the noise detected when the detector is not receiving any photons but producing noise itself. The largest contribution to this is the the noise from the APDs as they suffer from noise caused by current leakage caused by leakage across the surface of the detector and spontaneous triggers of avalanches caused by spontaneous production of electron hole pairs. These are the surface dark current I_{DS} and bulk dark current I_{DB} respectively. The spontaneous triggers are multiplied by the gain M of the APD and the result is the total dark current I_D as given by: (Perkin Elmer, 2003; Gunderson et al., 2006).

$$I_D = I_{DS} + MI_{DB} \tag{3.29}$$

Dark noise can be mitigated by cooling the APD to lower temperatures than the standard 20 deg which is fairly common practice at ground stations such as Wettzell (Renker, 2006). Other properties of influence on the dark current is the reverse voltage, governing the gain, the excess noise factor which scales with the reverse voltage and the system bandwidth which is governed by the amplifier behind the APD (Gunderson et al., 2006). These parameters are typically tuned for the specific case at hand and depend on ground station conditions and limitations. Therefore it is difficult to state one number for the dark noise of the receiver and instead a number of values is reported based on several sources in Table 3.1.

Table 3.1: Dark noise count rates.

Origin	Value [kHz]	Source
Stated Average	0.1 - 10	(Degnan, 2002a)
Ulrich Schreiber	10	(Schreiber, 2017)
SAP-series	15	(Laser Components, 2016)
PGA-200	75	(Princeton Lightwave, 2010)
PGA-025u series	100	(Princeton Lightwave, 2017)

Here the values are taken for the typical conditions reported in the data sheets for the APDs and taking all the values from Table 3.1, it can be seen that it ranges from 0.1 kHz to 100 kHz. This means that in the worst case, 100.000 photon detections per second are expected caused by the dark noise of the APD while this means only 100 photons per second are expected in the best case. The values used for dark noise are given in Section 8.1.

3.4.4. Noise Modelling

All equations discussed in this section produce a certain mean expected photons per second that reach the receiver. Then Poisson statistics are used to model the actual noise:

$$P(X = k) = \frac{N^k}{k!} e^{-N} \tag{3.30}$$

Expressed here is the chance P that exactly k photons reach the receiver in a certain time period with N the expected number of photons reaching the receiver that time period, described by the equations in this sections.

Noise can be reduced in four different ways through four types of filtering. Spectral filtering uses a band-pass filter to reduce the noise from photons with a different wavelength than that of the expected signal and was seen in Equations 3.22 and 3.24 and can have a value of 0.3 to 20 nm. Here also the field of view can be reduced to reduce the amount of incoming photons, spatial filtering. When the arrival time is known to a certain accuracy, the detector can be activated only for that period of time that the signal is expected. This temporal filtering is done by gating the receiver and it reduces the expected number of photons N in Equation 3.30 by introducing a range gate. The last way of reducing noise, or actually false detections, is by setting a threshold for the number photoelectrons required to trigger a detection, setting up an amplitude filter.

3.5. Detection of a Laser Pulse

The scientific laser ranging community is moving more and more towards single photon detection using APDs in Geiger mode(Degnan, 2001, 2002b) where very low signal strengths can be employed for successfully laser ranging. In this mode every received photon is counted and thus also a lot of noise is detected making it no longer possible to distinguish a signal photon from a noise photon. Instead the signal is extracted through the use of statistics such as post-detection Poisson filtering, taking advantage of the fact that noise is Poisson distributed in time while the signal will be present at a fixed frequency. For this, multi-kilohertz lasers with very short laser pulses are used to be able to use these statistics. However, GALA is not optimised for laser ranging and operates only at a frequency of 30 Hz. Given the short amount of time that the laser pulses are detectable, it will be unlikely that this method can be used. Furthermore the arrival times of the pulses sent by GALA will be to unpredictable to cope with the noise since an orbit prediction accuracy of 20 m is common in satellite laser ranging while JUICE will be at hundreds of meters at its best. Thus it is concluded that single photon detection is not possible in this study and thus is not considered further. This means that the APD used for detection will operate in linear mode and not in Geiger mode and that detection at very low signal intensities is not possible. However the pulse energy of GALA at 0.25 mJ is considerably higher than for lasers that make use of high frequencies and low intensities.

A threshold can be used to discriminate the signal from the noise. Here the receiver is looking in the direction where the signal should be coming from and the APD is detecting the incoming photons for a period of time. When this signal is evaluated in terms of photons per second, peaks that rise above the noise are expected to originate from the laser pulse, since at this point in time, suddenly many photons will arrive at the detector while the noise behaves randomly in time but with a specific mean number of expected photons per second. The APD is now operating in linear mode and will continuously measure the incoming photons by outputting a voltage and this voltage is recorded and can be analysed. Now this analysis can be done immediately and parallel while receiving signal and it can be done afterwards. For example GALA does this immediately employing certain procedures and algorithms as it has no storage capacity to keep the full recordings for every detection it does. However on ground this storage capacity will be available and one could visually inspect the recorded signal to identify pulses. This will be however a tedious exercise and for this thesis an automated method is required such as employed by GALA and many other altimeters.

Instead the signal is divided in bins with a certain length in time. Each bin is analysed separately for its signal level and when the signal is higher than the threshold set, the bin is identified as the signal bin. The length of the bin is chosen such that if a signal arrives, the largest increase in signal is achieved to make sure it stands out from the noise. This is achieved by setting the length of the bin such that the entire expected laser pulse is captured. In the case of the 1-sigma length of the GALA laser pulse of 2.9 ns, one can set the bin to a length t_{bin} such that it corresponds to the 6-sigma value of the pulse, 17.4 ns. This makes sure 99% of the pulse is captured in a single bin, assuming that the signal falls exactly synchronised in a bin. Here it is also assumed that the pulse is not broadened during its propagation. Pulse broadening is indeed negligible for pulses larger than 20 ps (Lu et al., 2012). Thus all of the pulse falls within one bin and is not divided into

two bins. This is a valid assumption since when the signal is analysed one can shift the start of the bins as required.

Now within each bin a certain number of photons will be recorded. Let N_s be the number of signal photons received by the ground station when a pulse is recorded in the bin. N_s will only be present when a pulse is received in a bin. However for all bins, N_b is the sum of all the background noise received at the detector within a bin given in Equation 3.31. When a signal is present in the bin the total number of photoelectrons is than given as in Equation 3.32.

$$N_b = n_b\, t_{bin} \tag{3.31}$$

$$N_{tot} = N_s + N_b \tag{3.32}$$

When setting up threshold detection, a threshold K_t is specified as the number of photons to be received in a bin for a detection to be registered. When the total number of photons N_{tot} given in Equation 3.32 rises above K_t, the bin is identified as a signal bin (Degnan, 2002a). Thus it is assumed that no other means of discriminating the signal from noise is used. Using Poisson statistics given in Equation 3.30, the probability P_d that the signal is correctly detected, when N_{tot} is equal to or exceeds the threshold, is given by Equation 3.33. This can be simplified to Equation 3.34 since the probability is equal to one minus the probability that it does not correctly identify the signal (Degnan, 2002a).

$$P_d(N_{tot} \geq K_t) = \sum_{k=K_t}^{\infty} \frac{N_{tot}^k}{k!} e^{-N_{tot}} \tag{3.33}$$

$$P_d(N_{tot} \geq K_t) = 1 - \sum_{k=0}^{K_t-1} \frac{N_{tot}^k}{k!} e^{-N_{tot}} \tag{3.34}$$

When no signal is present in the bin, a false detections can take place when the noise N_b exceeds the threshold and the bin is falsely identified as the signal bin. The probability of a false identification is given by:

$$P_{fa}(N_b \geq K_t) = 1 - \sum_{k=0}^{K_t-1} \frac{N_b^k}{k!} e^{-N_b} \tag{3.35}$$

Now both the possibilities of a bin with a signal present and a bin with no signal present are covered by Equations 3.34 and 3.35. The probability P_{fa} can be limited by setting a certain threshold, but will never become zero. With a bin size of 17.4 ns, the amount of bins is very large, around 57 million bins per second. Thus even with a very small P_{fa}, many false detections can take place while only 30 times per second a pulse detection can take place. To mitigate this, a very high threshold can be set, decreasing P_{fa} but also decreasing P_d, which is unwanted. Instead laser altimeters typically make use of the fact that the arrival time of a pulse can be predicted when range information is present. When the position of the spacecraft can be predicted, a range can also be predicted and used to divide the incoming signal into range gates. Laser altimeters typically gate their receiver using certain range gate. This range gate t_g is a certain period in time where the incoming laser pulse is expected. The better the prediction of the range, the smaller the range gate can be set. When the detector is only active for a limited amount of time, also the number of bins N_{RG}, given by Equation 3.36, will become smaller.

$$N_{RG} = \frac{t_g}{t_{bin}} \tag{3.36}$$

Thus the range gate t_g will contain a number of bins N_{RG} for which it has to be decided which bin is a signal bin. For standard laser altimeter operations, with every pulse sent out, a pulse coming back can be expected and thus in every range gate a signal will be present. In the case of the calibration through laser ranging, most of the times the laser will not be pointing at the ground station and thus most of the times no signal will be present. However due to the uncertainty in the misalignment, it is not known when it is pointing at the ground station and thus for every range gate still a choice has to be made on whether or not the range gate contains a signal or not.

Figure 3.6 visualises the concept of range gates with bins. Here a simplified signal is presented where the amount of received photons per bin is shown. For visualisation purposes, only five bins per range gate are shown and the contributions of noise and signal are shown separately while in reality there is no way to discriminate this. A threshold is set at 5 photoelectrons and 4 range gates are depicted in time.

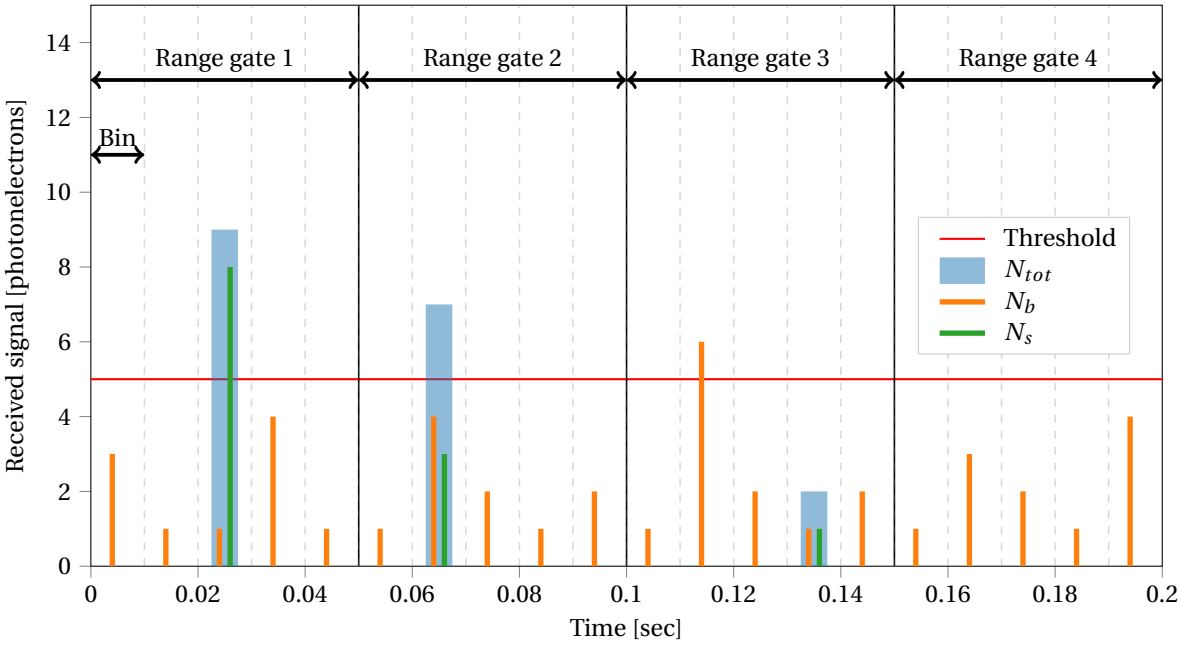

Figure 3.6: Overview of the effect of a detection threshold used in combination range gates and bins. Four different range gates are depicted in terms of signal leading to various cases for detection.

If a signal is present in the range gate, it will be present in only one bin and the chance of detection of that signal in the range gate is again given by Equation 3.34. This case is visualised in the first three range gates in Figure 3.6 where in all three a signal is present. In the first range gate, the signal itself would already be strong enough to trigger a detection but N_{tot} is raised a bit by some noise. In the second case one of the advantages becomes clear of threshold detection as here the signal itself is not strong enough to exceed the threshold. However also noise is received raising N_{tot} above the threshold and triggering a detection once more. Thus when the threshold is chosen appropriately and the noise conditions allow for it, one can even detect pulses that do not exceed the threshold themselves. Unfortunately, with many bins and a certain noise level, also false detections will happen as depicted in the third range gate in Figure 3.6. Here there is actually a signal present but it is not strong enough to trigger a detection while noise does trigger a detection. There is no way to distinguish the signal from the noise here and thus this information is lost unless the threshold would be lowered. However then the threshold would be set at 1 and many false detections would take place. In the fourth range gate, no signal is present and the threshold prevents any detection which is desired as no signal is present here.

The probability that a detection is triggered by noise such as in the third range gate in Figure 3.6, the probability of false detection P_{FD}, is the probability that in one or more bins the noise exceeds the threshold. This is the sum of the binomial distributions for one or more bins exceeding the threshold for one range gate:

$$P_{FD} = \sum_{n=1}^{N_{RG}} \frac{N_{RG}!}{n!(N_{RG}-n)!} P_{fa}^{n} (1-P_{fa})^{N_{RG}-n} \tag{3.37}$$

This can be rewritten as 1 minus the chance that the noise does not exceed the threshold in any of the bins, which is 1 minus the chance that it does exceed the threshold in a bin, resulting in:

$$P_{FD} = 1-(1-P_{fa})^{N_{RG}} \tag{3.38}$$

These equations show that now the probability of false detection can be decreased without decreasing the chance of detection by just decreasing the range gate. With no signal present, a low P_d, and no false detections take place, a low P_{FD}, no detection is registered and the range gate is identified as not to contain a signal as visualised in the fourth range gate in Figure 3.6.

For this laser ranging experiment, the spacecraft is scanning Earth in a certain scan pattern for a certain period of time. During this period it is unknown when the laser pulses will hit the detector due to the unknown misalignment. However, when the laser pulses hit the detector, this will only be for a relatively short

time compared to the total scan time. Thus it is important to be able to detect the passes of the laser immediately while making sure that the false detections are not too numerous and make this too difficult. This is different from other missions since in altimetry and satellite laser ranging it is known that a signal will return. Thus here the possibility that no detection takes place in the presence of a signal should be minimised and the threshold should make cases such as for the second range gate in Figure 3.6 possible. At the same time the probability of false detection in absence of a signal should also be minimised by selecting the threshold such as in the fourth range gate. It now becomes clear that the threshold selection is mostly governed by the noise, which is itself highly influenced by ground station parameters, and by the range gate which depends on the range prediction accuracy. The influence of choosing the threshold for misalignment calibrated as envisioned in this thesis is analysed and discussed in Section 8.4 while the implementation of pulse detection in the simulation is discussed in Section 6.1.1.

4

Laser ranging

One of the objectives of this thesis is to develop a calibration procedure for GALA. Laser ranging is selected as the method to be able to perform the best calibration possible; during the interplanetary cruise of JUICE towards Jupiter. This means that the laser ranging procedure has to work with the techniques available on GALA and JUICE in order to perform such a successful laser ranging experiment. This chapter will aim at providing the required knowledge on the principles and techniques used before and required to perform such an experiment. Section 4.1 will start with introducing GALA and its main characteristics as GALA was never build for laser ranging. Also two other laser altimeters, Mercury Laser Altimeter (MLA) and Hayabusa 2, will be introduced here. Section 4.2 takes a look at calibration procedures for laser altimeters and investigates how alignment calibration has been done for other altimeters. Finally Section 4.3 concludes with an overview of laser ranging techniques and the involvement of ground stations.

4.1. GALA

GALA is a classical laser altimeter using more powerful laser pulses at lower frequency to perform range measurements (Hussmann et al., 2014). The design is an evolution, with adaptations to its own requirements, of BepiColombo Laser Altimeter (BELA). The expected performance for the time resolution is under 1 ns resulting in a range accuracy up to 15 cm or 8 cm under optimal conditions (Lingenauber et al., 2013). GALA will also return pulse intensity and wave-form analysis providing the capability to assess also the surface albedo and the roughness.

4.1.1. Goals

Laser altimetry can provide characterisation of the shape and its variations in time, topography and rotation of a body, fundamental for a space exploration mission. GALA will contribute on five topics, starting with proving the existence of the subsurface ocean and characterising this ocean along with the ice shell. Furthermore, it will measure forced physical librations and determine the spin-axis obliquity and provide data about Ganymede's shape, global topographic measurements and local topographic measurements contributing to the science goals presented in Section 2.1. Also detailed topographic profiles can be made of the terrain, in particular the groves in the surface. This will be accompanied with information about the slopes, roughness and albedo of Ganymede (Hussmann et al., 2014). In order to do this, the design of GALA is capable of delivering sub nanosecond time resolution resulting in a range accuracy below 15 cm or 8 cm at its best. The pulse extraction required for this is done by sophisticated algorithms on board that can detect a signal with a minimum signal to noise ratio of 1.2, also extracting pulse intensity, width and shape in order to asses not only range but also the mentioned albedo, slopes and roughness. GALA is build and developed by a consortium consisting of institutes and industry in Germany (DLR), Switzerland (University of Berne, Physics Institute, Space Research and Planetary Sciences), Japan (Chiba Institute of Technology, Planetary Exploration Research Center) and Spain (Institute of Astrophysics of Andalucia-CSIC).

4.1.2. Technical Concept

GALA consists of three units; the Transceiver Unit (TRU), housing the transceiver and receiver, the Electronic Unit (ELU), housing most computers, and the Laser Electronic Unit (LEU), housing the control computer for

the laser. These units and their subsystems are visualised in the block diagram in Figure 4.1.

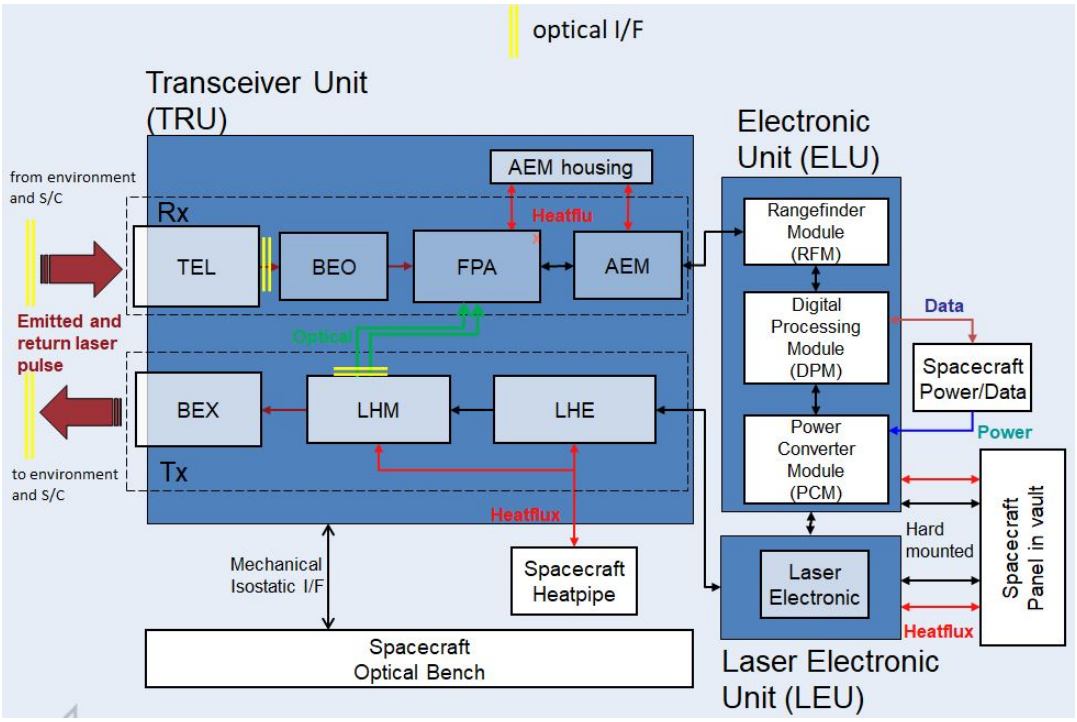

Figure 4.1: Block diagram of GALA (Lingenauber et al., 2014).

JUICE is a radiation sensitive mission requiring many radiation mitigations on different levels. One of the mitigation techniques is the creation of a radiation vault in the spacecraft consisting of a box made of titanium. As electronics are the most sensitive, most electronics are placed in the vault where possible. This also holds for the ELU and LEU of the GALA instrument.

The ELU consists of the rangefinder which receives the digitised signal from the detector. Then this module analyses the signal by filtering, sampling and applying algorithms to eventually detect the peak of the pulse and determine the range. When the range gate is opened, the incoming signal is sampled at 500 MHz (Steinbrügge et al., 2015). This signal is then analysed on board to find the peak in the signal. This is possible up to a SNR of 1.3. The digital processing module can be seen as the main computer of the instrument serving as the interface with the spacecraft. This means it takes care of preparing the measurement data for sending to the spacecraft communication system, receives commands from the spacecraft and controls all instrument functions. The power converter module takes care of providing power for every signal subsystem in the instrument (Lingenauber et al., 2013). The LEU contains the control electronics for the laser. Here the appropriate power and control signals are prepared for the laser. The TRU houses both the receiver and the transmitter and is mounted on the optical bench of JUICE. This optical bench provides a more stable structure in terms of thermal and dynamic stability than the spacecraft structure itself. Thus it is enhancing the pointing knowledge of the instruments. Figure 4.2 shows the current design of the TRU depicting the telescope, detector and electronics and laser. It requires 52 W of power and weights around 15 kilograms (Lingenauber et al., 2013).

All components of the TRU are located under the disk of the telescope protecting them from radiation from that direction while the other directions are covered by the spacecraft itself. This is to cope with the extreme radiation environment in which GALA will operate and also brings a heavy burden on the weight of the TRU since the thickness of the telescope disk is not determined by the optics but by what is required from radiation perspective. Therefore, the disk is not hollow, as would be required for the optics but is solid and made from a metal alloy.

The transmitter consists of two cold redundant laser resonators housed in the laser head module which is controlled by the laser head electronics unit. Laser beams are created by pumping light into an optical resonator or cavity, where the light travels through a gain medium. This gain medium is in this case the solid state ND:YAG producing a laser wavelength of 1064 nm and the resonator is transversal pumped by diodes.

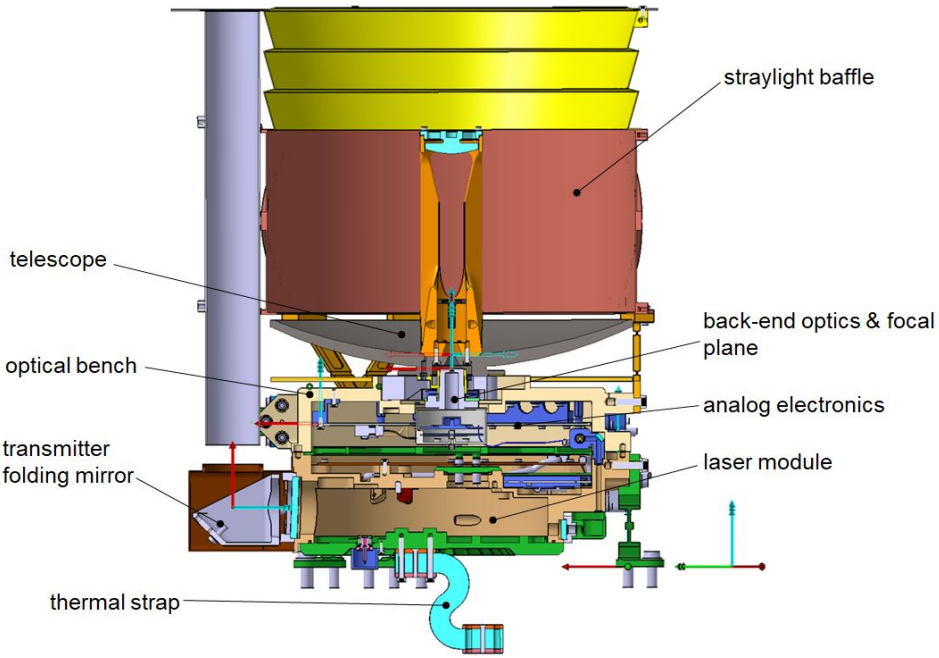

Figure 4.2: Design of the Transceiver Unit of GALA (Lingenauber et al., 2013).

The emittance of the pulse is controlled by an active Q-switch which means that the laser has an externally and actively controlled attenuator, creating the 30 Hz nominal operating frequency for the pulse rate of GALA. The energy produced by the laser is 17 mJ in Ganymede orbit, but is 25 mJ at beginning of life with a 1-sigma pulse width of 2.9 ns. After the laser pulse is generated, it is collimated by optics in the transmitter telescope resulting in a divergence angle of 100 μrad full cone and an optical efficiency of 0.85.

The receiver consists of a telescope with an optical filter to reduce unwanted light getting to the detector for which an APD is used. Table 4.1 summarises the properties of GALA.

4.1.3. Other Laser Altimeters

Hayabusa 2 LIDAR

Unlike GALA, the Hayabusa 2 LIDAR is developed with very different goals and conditions. It will orbit an asteroid and part of the mission is to touchdown on its surface. For this, the LIDAR will be used for navigation during this procedure, thus it had to be able to operate correctly as close as 30 meters from the surface. The orbit around the asteroid will also be very low such that this altimeter has a maximum range of 30 km. This is reflected in the high divergence angle of the laser beam of almost 250 arcsec as seen in Table 4.2. Figure 4.3 depicts the LIDAR in its final form with its telescope clearly visible. However, the receiver actually employs two telescopes, one for short range and one for long range. The long range telescope properties are reported in Table 4.2 as this one is envisioned to be used for calibration purposes (Noda et al., 2017).

Figure 4.3: Hayabusa 2 LIDAR (Mizuno et al., 2016).

Table 4.1: Instrument parameters of and GALA.

Parameter	Symbol	Unit	GALA
Laser transmitter			
Pulse Energy (Beginning of life)	E_t	mJ	25
Pulse Energy (At Ganymede)	E_t	mJ	17
Wavelength	λ_t	nm	1064
Frequency	f_q	Hz	30
Pulse width	σ_0	ns	2.9
Divergence (full cone)	θ_T	μrad	100
Divergence (half cone)	$\theta_{\frac{1}{2}}$	arcsec	10.3
Transmitter optical efficiency	η_t		0.85
Receiver optics			
Telescope radius	r_R	cm	12.5
Field of view (full cone)	Θ_{FOV}	μrad	450
Optical efficiency	η_r		0.85
Optical filter efficiency	ϵ_{RF}		0.8
Optical filter bandpass	σ_{RF}	nm	0.36
Detector			
Quantum efficiency	η_q		0.36
APD dark current (bulk)	I_{DB}	pA	50
APD dark current (Surface)	I_{DS}	nA	20
Maximum gain	M		150
Transimpedance Amplifier (TIA) bandtwidth	B_0	MHz	100
Digital filter width	σ_f	ns	5-60

Mercury Laser Altimeter

The design of MLA is based on the Geoscience Laser Altimeter System (GLAS) and generates laser pulses with a wavelength of 1064 nm. To detect the footprint, four telescopes are used that all have an optical fibre leading to one single detector, the APD (Cavanaugh et al., 2007). This was done to make sure that the footprint would be in the field of view of the telescopes since there existed a high uncertainty in the alignment. The instrument layout is shown in Figure 4.4 where the four detectors can be seen with the laser situated in the middle.

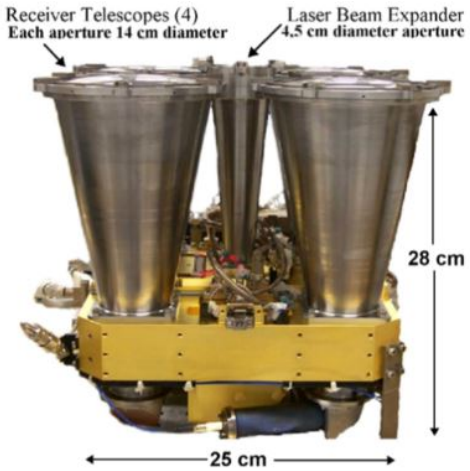

Figure 4.4: MLA instrument without covers (Cavanaugh et al., 2007)

Table 4.2 summarises the most important properties of MLA and the Hayabusa 2 LIDAR.

Table 4.2: Instrument parameters of MLA and the Hayabusa 2 LIDAR

Parameter	Symbol	Unit	MLA	Hayabusa 2 LIDAR
Laser transmitter				
Pulse Energy (Beginning of life)	E_t	mJ	25	15
Wavelength	λ_t	nm	1064	1064
Frequency	f_q	Hz	8	1
Pulse width	σ_0	ns	2.5	7
Divergence (half cone)	$\theta_{\frac{1}{2}}$	arcsec	8.3	248
Transmitter optical efficiency	η_t		0.85	
Receiver optics				
Telescope radius	r_R	cm	5.3 x 4	11
Field of view (full cone)	Θ_{FOV}	μrad	400	1500
Optical efficiency	η_r		0.77	
Optical filter bandpass	σ_{RF}	nm	0.3	
Detector				
Quantum efficiency	η_q		0.35	
Maximum gain	M		100	
TIA bandtwidth	B_0	MHz	100	

4.2. Calibration of Laser Altimeters

As stated earlier, the pointing errors originate from the fact that there is a certain uncertainty in where the laser is pointing and thus from what or where it is actually making a range measurement. Two things govern where the laser altimeter is pointing, the position of the laser, and at which angle it is pointing. The first error is the result of the uncertainty in the trajectory of the spacecraft as determined by orbit determination efforts. The second error, the actual pointing error of the spacecraft is composed of two contributions. Firstly, there is the inertial spacecraft pointing knowledge, or the difference between the actual pointing angle and the measured pointing angle. Secondly, the laser altimeter line of sight is considered to be pointing nadir. However, as the line of sight will not be perfectly aligned with the nadir axis of the spacecraft, a certain misalignment will be present. This alignment error is subject to vibrations, microgravity and settling and thus is to be measured in orbit, after launch and settling have taken place (Steinbrügge et al., 2015). Section 5.1 elaborates further on these errors while here an overview is given on different methods to calibrate the alignment of the altimeter.

A first step in measuring the misalignment of the laser altimeter is by doing this on ground. This can be done very precise, for example for GALA it is required to measure this with an accuracy of 14 arcsec as stated in European Space Agency (ESA) (2017). Other procedures for calibrating the electronics and other features area also planned according to the calibration plan developed for GALA (Althaus and Stark, 2017). However due to launch vibrations, microgravity and shocks due to separations of stages the alignment will change making the measurements on ground not very representative, depending on the stability of the structures. However it is still common practice to measure all alignments on ground as was done for e.g. MLA (Cavanaugh et al., 2007; Sun and Neumann, 2015). For LOLA the pointing was to be derived from analysis of the orbit and on ground measurements (Zuber et al., 2010; Smith et al., 2010). The misalignment was of particular concern for the GLAS as the alignment could not be measured on ground (Schutz et al., 2005) and thus had to be performed in orbit.

4.2.1. In orbit calibration

Measuring the misalignment of the laser altimeter can be done using terrain knowledge already gained by previous missions. Here six cases can be distinguished that all require good knowledge of the surface that is to be measured by the laser altimeter (Rowlands et al., 2000).

Direct Laser Altimetry above Oceans

Previous missions have established well mapped ocean models. Also an ocean has very small slopes which has as a consequence that a misalignment has almost no effect on the measured range as shown in Equation

1.3 where the slope has a large contribution to the range error. However, when the spacecraft changes attitude to off-nadir angles, the range error will be very sensitive to misalignments. This effect, and the accurate models of the sea surface height can be used when it is compared to the measurements of the altimeter (Rowlands et al., 2000).

Crossovers above Oceans
When the laser altimeter takes measurements of the same surface multiple times, as is the case with crossovers, the multiple measurements can be used to determine the average range and thus counter the effects of range bias and misalignment (Rowlands et al., 2000).

Direct Laser Altimetry over Land
As for the direct laser altimetry above oceans, the same can be done over land if accurate models exist(Rowlands et al., 2000). However over land, usually slopes are much more present, reducing the usefulness of this technique.

Crossovers over Land
As for the crossovers over oceans, the same can be done over land if accurate models exist (Rowlands et al., 2000).

Profile matching
The measurements of the altimeter will form a profile. This profile can be compared with other profiles constructed of the same surface. For example previous radar missions or camera pictures can provide a model for the profile of the surface (Rowlands et al., 2000).

Waveform matching
The slopes and vegetation will alter the waveform for the laser pulse that travels back to the receiver from the surface of the Earth. If a model exists that can accurately predict this, then the waveform measurements can be compared to the prediction of the model and thus it can be derived where the laser was pointing (Rowlands et al., 2000).

The technique of direct laser altimetry over oceans was further studied (Luthcke et al., 2000). For this technique, the observed ranges are compared to computed ranges from a measurement model. The residuals or discrepancies between the two are minimised by estimating the parameters that influence the measurements, including the misalignment. A manoeuvre was developed to exploit the sensitivity of the misalignment above oceans (Luthcke et al., 2000). These manoeuvres are easily implemented and give an excellent accuracy (Luthcke et al., 2000). These manoeuvres were later implemented in the real mission and gave indeed good results as the calibration manoeuvres were estimated to have a precision of 1 arcsec resulting in a pointing knowledge accuracy (2-sigma) of around 4 arcsec (Schutz et al., 2005).

It was also proposed to send a sample of the laser beam into the star trackers and using the stellar reference frame to measure the pointing of the laser altimeter (Sirota et al., 2005). Although a novel concept it was decided not to implement this solution as other solutions already provided the required accuracy for the mission. Also for GALA this solution is not deemed feasible.

4.2.2. Direct Detection

Another method proposed is the direct detection of the laser footprint (Lisano and Schiutz, 2001). This can be done in two ways, either the laser footprint is detected from above or detectors are place on ground. This was also studied for ICESat (Lisano and Schiutz, 2001) and later a system was designed an verified (Magruder et al., 2003) using detectors on ground. Finally this system was used, yielding good calibration results of 2.5 to 5 arcsec accuracy for the calibration (Magruder et al., 2005). Instead of using small detectors, which are only suitable for short ranges such as Earth orbiting satellites, a laser ranging ground station can also be used to detect the laser footprint for large distances. This has been done for MLA on the MESSENGER spacecraft at a distance of 23 billion kilometres or 0.16 AU (Smith et al., 2006, 2005) and has been tried by the HAYABUSA 2 spacecraft (Noda et al., 2017). It is this method that is most suitable for the calibration of GALA as also here large distances will be involved and specialised equipment is required for a successful calibration. This is the method used in this thesis and will be simulated and analysed to be able to conclude on its calibration accuracy.

4.3. Laser ranging

Laser ranging differs from altimetry in the sense that no reflection on a surface of a body is present. Therefore different concepts are of different importance compared to what was presented in Section 1.1. Also a transponder at the other end of the signal is now required and needs to be taken into account.

4.3.1. Satellite Laser Ranging

Satellite Laser Ranging (SLR) is mostly used to track satellites orbiting Earth, including the natural satellite, the Moon (Bender et al., 1973). A ground station equipped with a laser will fire laser pulses at satellites that are equipped with a laser retro-reflector and the accuracy of these systems can be considered very high these days, the precision of the travel-time measurement is in the order of picoseconds, or a few millimetres (Gurtner et al., 2005). Larger errors originate from modelling the position of the retro-reflector with respect to the centre of mass of the satellite and the propagation of the laser pulse through the atmosphere. The total accuracy is now going towards 1 cm or better for most systems present on Earth.

Most ground stations used for satellite laser ranging are united in the International Laser Ranging Service (ILRS) founded in 1998 (Tyahla and Noll, 2016). The ILRS provides a geodesy service to the International Association of Geodesy (IAG) and consists of the National Aeronautics and Space Administration (NASA) network, the European EUROLAS network and the Western Pacific Laser Tracking Network (WPLTN) and together the network consists of around 40 stations (Gurtner et al., 2005). Its applications consist of the maintenance of the International Terrestrial Reference Frame (ITRF) for which the specially developed geodynamic satellites LAGEOS-1 and -2 are used. These satellites are essentially spheres that consist only of retro-reflectors, which are ranged multiple times a day by multiple stations making sure the position of the centre of mass of the Earth is precisely determined for geodetic purposes. This can then also be related to the position of the Earth in the celestial reference frame where the ILRS produces measurements of the polar motion and the length of the day (Gurtner et al., 2005). Also the ILRS contributes to the measurement of the gravity field of the Earth since the orbits of the geodetic satellites is altered by the gravity field that is changing over time (Pearlman ' et al., 2002). Lastly the ILRS provides orbit verification measures. Many satellites determine their orbits using GPS or other measures but since laser tracking provides the best accuracy their orbit determination solutions are checked against laser ranging measurements providing the best validity of their models possible. Ground stations can have far superior capabilities compared to spacecraft based systems in terms of power and mass and thus can provide higher repetition frequencies, laser pulse energies, detector gains and many more, including larger telescopes although not all ground stations have these superior capacities available.

4.3.2. Transponder Laser Ranging

While SLR as presented in Section 4.3.1 depends on the reflection of the laser beam, a new type of laser ranging is envisioned where the signal is not reflected but received by another transponder (Degnan, 2002a). This is required for laser ranging at longer distances than the Moon since the losses due to reflection and the distance for the laser pulse to travel back to the receiver is now gone. Therefore, laser ranging at much larger distance is achievable making laser ranging to Mars (Oberst et al., 2012) or its moon Phobos possible (Dirkx et al., 2014b). A distinction can be made between one way and two way laser ranging.

One way

For one way laser ranging the transmitter and receiver are uncoupled compared to traditional laser ranging. The transmitter simply sends a signal to the receiver located elsewhere. The most obvious and classical case is the one where the transmitter is an Earth-based ground station and the receiver is a transponder located on a satellite or planetary lander. The advantage is that the superior capabilities of an Earth based laser can be utilised while for the spacecraft only a detector has to be installed which is much easier than a total laser altimeter in terms of power and weight.

However the main disadvantage is that both systems use unsynchronised clocks which immediately introduce offsets resulting in an error in the range measurements. (Dirkx et al., 2015) investigated this for ranging to Phobos and found a mean error of 0.3 meters and also found that this was indeed caused mainly by clock errors and thus to achieve a high accuracy, very high accuracy clocks are required.

Two way

In two way laser ranging, a tow way laser link is established using to transponders who can both sent and receive laser pulses. These two systems, terminal A and terminal B can operate in two modes, echo laser ranging and asynchronous laser ranging.

Echo ranging is performed by sending a pulse from terminal A to terminal B which is waiting for the pulse to arrive before sending a pulse back. However terminal B must detect a signal of A before it sends a signal at all, making the system not so reliable. The detection algorithm can be modified to make it possible to detect a pulse at lower signal to noise ratio but this will introduce more false detections and thus false echo's. So although this mode largely removes the problem of the clock errors, it has its own problems.

These problems can be overcome using asynchronous laser ranging where the laser pulses are independently transmitted to the other terminal as visualised in Figure 4.5. Here two independent pulses are fired at times t_{A1} and t_{B1} and later received at the other station.

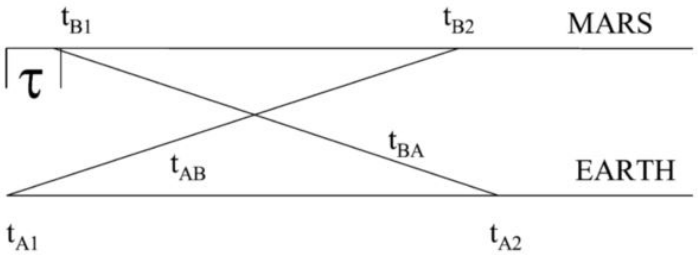

Figure 4.5: Visualisation of the time of transmitted pulses for an Earth - Mars case (Degnan, 2002a).

Then two measurements or four measured times are paired to each other after all data from terminal B, located not on Earth, is sent to Earth. This results in the range where use is made of the paired measurements where R is the range between the terminals (Degnan, 2002a):

$$R = \frac{c}{2}\left[(t_{A2} - t_{A1}) + (t_{B2} - t_{B1})\right] \tag{4.1}$$

$$\tau = \frac{(t_{A2} - t_{A1}) - (t_{B2} - t_{B1}}{2\left(1 + \frac{R}{c}\right)} \tag{4.2}$$

The offset in time τ between the clocks is given by Equation 4.2 (Degnan, 2002a) where a small correction term is introduced to cope with the instantaneous range rate between the terminals. (Dirkx et al., 2015) analysed this form of laser ranging and for the same case of ranging to Phobos concluded that it would give an accuracy of 2.5 cm, a significant improvement compared to one-way laser ranging.

4.3.3. Ground Stations

Ground stations are the key component of transponder laser ranging and laser ranging in this study is limited by the locations and capabilities of the ground stations. Therefore, this section will give a short overview of the existing ground stations and their typical properties.

Shown in Figure 4.6 are all ground stations that are part of the ILRS and their location on Earth. Most ground stations are located in the northern hemisphere and their locations are precisely known since most of them take part in experiments that deliver the international reference frames used for science. Ground stations differ much from space-born lasers as they are not constraint by power, weight and size. Therefore, ground stations offer much higher signal strengths and large receiver apertures. Also data storage is not a problem and the crew has years of experience in laser ranging applications.

A number of ground stations are selected to be studied based on their location and performance. Especially for laser ranging to JUICE, it is important to have both southern and northern hemisphere stations as the latitude at which JUICE will be as seen from Earth will differ throughout its trajectory.

Table 4.3 shows the ground stations and their properties starting with their telescope diameter. This property is one of the most important and fixed properties as its diameter increases the link budget significantly as seen in Equation 3.18. This property is also not likely to change within the next ten years, the time at which the laser ranging will probably take place. With the telescope also comes the optical throughput efficiency and the divergence angle of the laser transmitted. However, this is not the case for other properties such as the quantum efficiency, spectral bandwidth and pulse energy. Already Wettzell is using a better APD with a higher quantum efficiency than reported on the ILRS website (Schreiber, 2017; Tyahla and Noll, 2016) and also better APDs will be developed in the next ten years and this also holds for the pulse energy of the laser. New lasers can be bought or lend from other institutes when other laser properties are required. Ground stations require an angular separation between the Sun and the target and a minimum elevation of both 20 degrees.

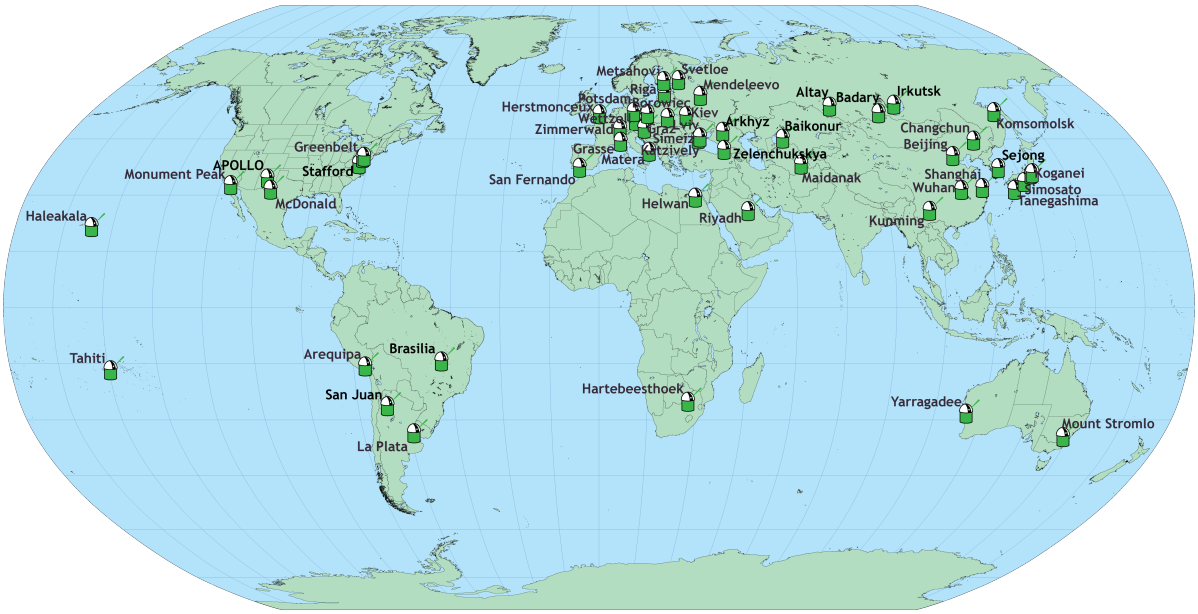

Figure 4.6: Overview ILRS ground stations (Tyahla and Noll, 2016).

Table 4.3: Overview of the ground stations and their reported properties (Tyahla and Noll, 2016).

Parameter	Wettzell	Grasse	Apollo	Mt. Stromlo	Goddard
Code	WETL	GRSM	APOL	STL3	GGAO
Latitude [deg]	49.1444	43.7546	32.780361	-35.3161	39.0206
Longitude [deg]	12.8780	6.9216	-105.820417	149.0099	-76.82770
Telescope diameter d_r [m]	0.75	1.54	3.5	1	1.2
Optical efficiency η_r [-]	0.5	0.22	0.4	0.35	
Spectral bandwidth $\Delta\lambda$ [nm]	12	0.12	-	2	
Receiver FOV Θ_{FOV} [arcsec]	9	7-20	1.4	12	130
Quantum efficiency η_q [-]	0.5	0.2	0.3	0.2	
Laser energy E_t [mJ]	200	300	115	2200	15
Optical efficiency η_t [-]	0.5	0.45	0.6	0.75	
Beam divergence angle $\theta_{\frac{1}{2}}$ [arcsec]	0.5-100	0.5-5	0.5	7	40

5

Pointing and Attitude modelling

Two concepts are of large influence on the calibration of GALA. The pointing of GALA and the attitude that will be used during laser ranging. The pointing will determine the pointing budget used for measurements during scientific operations as well as during laser ranging. The budget will govern what the final range error is for the measurements and it is of great importance that all involved are aware of their contributions to this budget. The attitude of the spacecraft is not perfect and therefore will introduce an error in the calibration. This will cause a loss of information for the calibration procedure and thus it must be investigated how and which information is lost.

Section 5.1 will introduce the concept of pointing errors as used in this thesis for GALA. Then it will compose a budget incorporating the various contributions from the different sources ultimately leading to a final pointing error for the scientific mission. However also a pointing error will be introduced during the laser ranging and this is also part of the result in this section. Further more the behaviour of the attitude errors will be introduced which are used in Section 5.2. There an attitude model is developed based on the pointing errors found.

5.1. Spacecraft Pointing

Pointing errors are at the heart of this study as one of these pointing errors is to be reduced by the envisioned calibration and are introduced in this section. Both the concept of pointing errors as set by ESA in their various forms is treated, as well as the pointing error for the GALA mission and the resulting pointing error budget. Finally time dependent pointing errors are introduced and analysed that will serve as an input for the laser ranging simulation model.

5.1.1. Pointing Errors

The pointing of a spacecraft is never perfect and will consist of several errors that will contribute in a pointing offset with respect to the desired pointing. This pointing error is specified as the angle $\Delta\phi$ between the desired and the actual pointing. Pointing errors are caused by different errors and one main separation is made between the pointing error caused by an error in the attitude control, the Control Error (CE) and the error caused by a relative position error, the Guidance Error (GE), both visualised in Figure 5.1. The GE is caused by uncertainties in the orbit of the spacecraft and although it is a position error, it can be translated into an angle and thus is used in the same way as the control errors. The pointing error caused by misalignment has the same effect as the control error in Figure 5.1, it will result in the misalignment angle $\Delta\phi_a$. However for the control error the origin lies in the attitude control system of the spacecraft while the misalignment error originates from multiple misalignments explained later. The control error is treated here as a single entity described by a single value given by the spacecraft manufacturer.

For each error two quantities exist; an absolute error, and an absolute knowledge error. The absolute error is the difference between the desired or commanded pointing and the actual pointing and is simply named the 'pointing error'. The knowledge error is the error between the actual pointing and the known (measured) pointing. Here the spacecraft pointing is for example measured by star trackers and accelerometers which also have a certain error in their measurements. For laser altimetry the knowledge error is the most important error as it is not very important where the laser is pointing as long as it is known with high accuracy as is

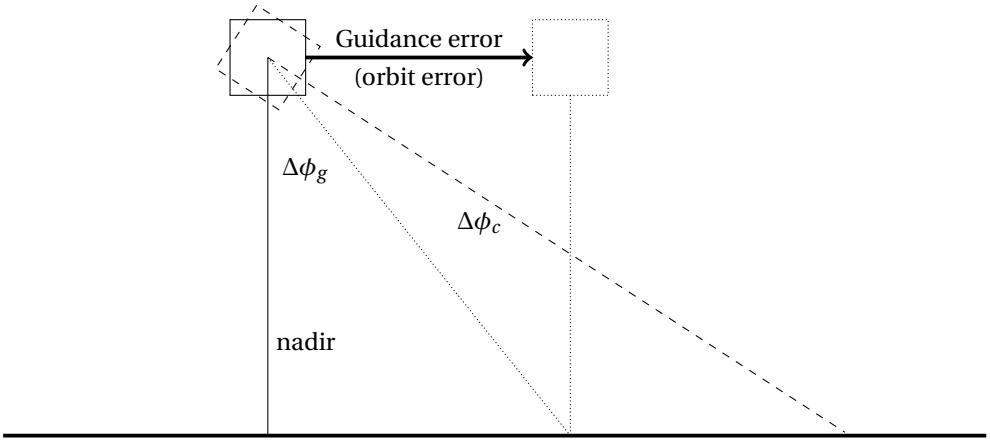

Figure 5.1: Pointing situation for a satellite pointing to a surface. The ideal and wanted case is a perfect nadir pointing of the spacecraft. However an orbit error will introduce the Guidance Error (GE) translated into the angle $\Delta\phi_g$. An error in the satellites attitude will introduce the Control Error (CE) which translates into the angle $\Delta\phi_c$.

reflected in the requirements set for GALA. When integrated, GALA should be integrated such that it points within 140 arcsec of the nadir direction. However this offset is also measured with an accuracy of 12 arcsec. So the difference between the desired and actual pointing is 140 arcsec while the pointing knowledge is 12 arcsec. For both the CE and the GE these two are defined as the Absolute Control Error (ACE) and Absolute Control Knowledge Error (ACKE) and the Absolute Guidance Error (AGE) and Absolute Guidance Knowledge Error (AGKE).

The concepts of absolute errors and absolute knowledge errors and the difference between guidance and control errors are important and often used in the following discussion and other sections. In practice, a certain location on Ganymede or Earth is selected to take measurements from. Then the spacecraft operator will determine when it is possible to take these measurements given the orbit predictions of the spacecraft. In this orbit prediction is an error which will translate into the AGE. Then the operator will aim the instrument by changing the spacecraft attitude introducing the ACE. After the measurements are taken and the data is comprehensively studied the orbit is reconstructed leading to an AGKE. This orbit reconstruction is often better than the prediction and thus the AGKE is often smaller than the AGE. The same holds for the attitude reconstruction introducing the ACKE, often with better accuracy than the ACE. Thus for most data analysis, only the pointing knowledge error is important where as the pointing error is useful preparing missions. This is also true for laser ranging, where the scan will be governed by the pointing error while the final calibration accuracy is determined by how well the attitude and orbit can be reconstructed afterwards.

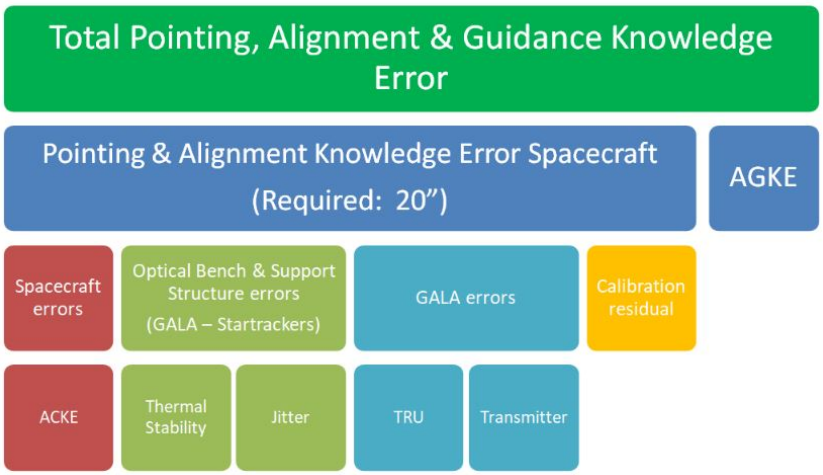

Figure 5.2: Overview of the various errors and there composition leading to the total pointing error

The combination of the ACKE and AGKE results in the final error that the total system delivers and that is used for analysis later. This Total Pointing, Alignment & Guidance Knowledge Error (TPAGKE), or simply put, the pointing error of GALA, is depicted in Figure 5.2 in the green on the top. It is the total error that is introduced into the laser and for GALA these consist of the two contributions given in blue in Figure 5.2, the AGKE, originating from the orbit determination, and the Pointing and Alignment Knowledge Error of the Spacecraft. Figure 5.2 also depicts which components are contributing to the latter error and here indeed the ACKE is the one error originating from the spacecraft, given in the red colour. The other errors originate from the optical bench and support structure, from GALA itself and finally from the calibration.

Figure 5.2 also includes two error sources for the optical bench, its thermal stability and its jitter. Jitter is in this case an unwanted vibration of the spacecraft and optical bench caused by the movability of the optical bench with respect to the spacecraft and the attitude control system. This will cause a constant vibration meaning the spacecraft is never completely frozen at any point in time. Thermal stability comprises the amount of pointing error that can be introduced by deformation of the structure due to fluctuations in temperature of that structure. Although the optical bench is especially designed to mitigate this effect, it is impossible to completely reduce this effect and thus is included. This effect also holds for every unit on a spacecraft, so also the TRU and the Transmitter experience this effect and also holds for the entire mission duration as the spacecraft can always heat up or cool down depending on its position and orientation. Thus it is impossible to get rid of this effect and it will always be included in any following pointing budget.

Another source of errors which holds for all components is the misalignment caused by mounting the unit onto another component. For example the transmitter is mounted on the TRU but it is impossible to do this perfectly and thus there will be a misalignment present between how it is supposed to be mounted and how it is actually mounted. A maximum deviation is allowed and specified as a requirement. Then after the mounting, another requirement requires the measurement of this offset with a certain accuracy, introducing the alignment knowledge of that component.

Note that this is all done on ground where gravity is present, introducing a force on any structure and thus deforming it. Once the spacecraft is launched and placed in orbit, this gravity environment will no longer be present and due to the change to a microgravity environment, the structure will get rid of the deformation and thus deform. This effect is named settling and affects more or less every unit on a spacecraft. Also the launch heavy vibrations can deform the structures but after the launch and exposure to a microgravity environment for a sustained amount of time, the settling has taken place and this error is assumed not to change over time.

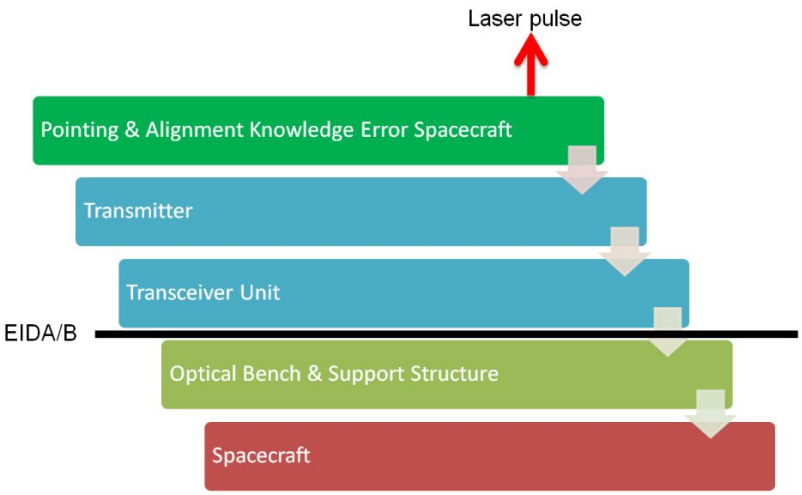

Figure 5.3: Flow down of the various components introducing pointing errors

The thermal stability, misalignment and settling all hold for each component which affects the transmitted laser pulse. This flow of error contributions is presented in Figure 5.3 showing the various components. This laser pulse is sent out by the transmitter which is mounted on the TRU as depicted in Figure 4.2. This entire unit is the responsibility of Deutsches Zentrum für Luft und Raumfahrt (DLR) Berlin but is mounted on a support structure which is mounted on the optical bench of JUICE. Between these two components, Figure 5.3 shows a black line, marking the border between the responsibilities in this discussion. Everything above

is the responsibility of DLR while everything underneath is the responsibility of ESA and Airbus Defence and Space. The requirements coming from the underneath the border towards DLR are written down in the Experiment Interface Document - Part A (EIDA) (European Space Agency (ESA), 2017) while the requirements vice versa are presented in the Experiment Interface Document - Part B (EIDB) (Deutsches Zentrum für Luft und Raumfahrt (DLR), 2017).

5.1.2. Pointing Budgets for GALA

All pointing errors introduced in the previous section will be used to construct the pointing budgets in Table 5.1. The structure of the pointing budget follows the structures introduced in Figures 5.2 and 5.3 but some concepts are required to correctly sum up the various pointing errors that were introduced.

Errors described in this thesis are not predictable and can therefore only be described by random process theory. They are also assumed to be caused by many independent random errors adding up to the error, thus by the central limit theorem, the error follows a Gaussian distribution 5.1 (Steinbrügge et al., 2015; European Space Agency (ESA), 2008, 2011, 2017; Deutsches Zentrum für Luft und Raumfahrt (DLR), 2017):

$$G(\mu_e, \sigma_e) \quad = \quad \frac{1}{\sigma_e \sqrt{2\pi}} \exp\left(-\frac{(e-\mu_e)^2}{2\sigma^2}\right) \tag{5.1}$$

Since the mean of the errors discussed here lies at zero, the error is completely described by the standard deviation and according to ESA standards, the error value given is the 2-sigma value of this Gaussian distribution and represents a 95% confidence level (European Space Agency (ESA), 2017). Thus most of the times the actual error is not known but it is 95% sure that the error lies within the value specified and this holds for all errors in the subsequent discussions. Thus all values given for errors throughout this theses are the 2-sigma values and are assumed to be independent (Deutsches Zentrum für Luft und Raumfahrt (DLR), 2017) and as such, the total error is given by:

$$\sigma_{total} \quad = \quad \sqrt{\sum_n \sigma_n^2} \tag{5.2}$$

Which will hold for all errors since they originate all from a separate structure (misalignment, thermal stability and settling) or have a completely different origin (control error, guidance error, calibration error).

All errors are specified with a 95% confidence level for a mixed statistical interpretation (European Space Agency (ESA), 2017). This mixed statistical interpretation means that the specified error e_r with the 95% probability P_c holds for all realisations k at every time t such that the probability P of an error e to be less than the required error value e_r is given by:

$$P\left(|e(k,t)| < e_r\right) \quad \geq \quad P_c \tag{5.3}$$

Each time the spacecraft would be rebuild and integrated is a realisation of the error. So the misalignment error randomly varies with respect to its range of possible realisations but once the spacecraft is integrated, the error is constant throughout the operational phase of the mission and can be defined by a standard deviation of the range of possible realisations. A time random error that does not depend on the realisation, such as torque disturbances in the control system and can in this case also be described by a standard deviation of that value that describes the range of the error in time. Thus all errors can be described and treated the same way (European Space Agency (ESA), 2011).

A requirement is specified by choosing the level of confidence and choosing e_r such that:

$$|\mu_{total}| + n_p \sigma_{total} \quad \leq \quad e_r \tag{5.4}$$

where n_p is the set at 2 since 2-sigma values are used here and μ_{total} is the mean which is zero in all cases here.

Equations 5.2, 5.3 and 5.4 only hold when the error is a linear sum of the contributing errors. For a pointing situation as depicted in Figure 5.4 this holds when the pointing errors is specified as an error about one axis. Here an error about the y axis will create e_y as shown in Figure 5.4. Now for GALA all errors are specified for two cases. Across Instrument Line of Sight (ILS) which are represented by x and y in Figure 5.4, or along

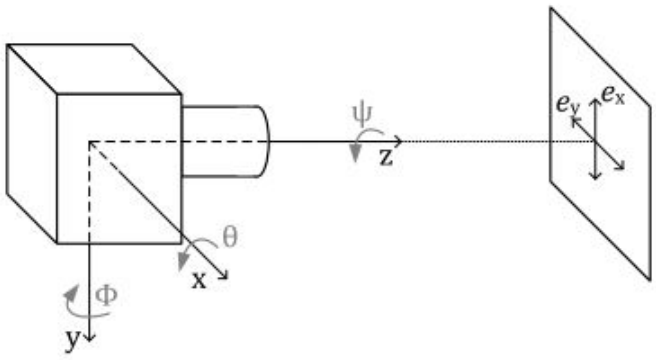

Figure 5.4: Pointing scene for GALA

the ILS, represented by the z axis. Since an error along z does not create an offset in pointing all errors are specified about x and y and always have the same value for both in this thesis. Thus when an error for the misalignment is specified of, for example, 10 arcsec, this means it is specified across the ILS, thus for both x and y it is the same value (Deutsches Zentrum für Luft und Raumfahrt (DLR), 2017). Then the total error for the ILS is given by Equation 5.6.

$$\phi \approx \sqrt{e_x^2 + e_y^2} \tag{5.5}$$

$$\phi_{max} \geq \sigma_{total}\sqrt{-2\log(1-P_c)} \tag{5.6}$$

However when the errors are added like this, the resulting error is does not follow a Gaussian distribution but a Rayleigh distribution (European Space Agency (ESA), 2011) and the error budget can be tested against the maximum error allowed using Equation 5.6. Now instead of a 2 sigma value, a 2.45 sigma value is required for a level of confidence of 95%. Now this will never be the case for the errors mentioned here since they only hold for one axis at the time, but it is important to note when one would compute the total pointing error.

Table 5.1 shows the budgets for mission operations in Ganymede circular orbit at an altitude of 500 km, the main mission phase for GALA, the budget during calibration and the budget for mission operations again, but now the calibrated case. Note that all values are at 95% confidence level as specified by ESA (European Space Agency (ESA), 2017; Deutsches Zentrum für Luft und Raumfahrt (DLR), 2017; European Space Agency (ESA), 2011). Also all errors are assumed to be uncorrelated. This assumptions is justified since every error is introduced by a separate unit with its own errors. For example the settling of the optical bench is uncorrelated with the settling of the transmitter as both have their own structure with its own properties. This is in accordance with ESA standards (European Space Agency (ESA), 2017; Deutsches Zentrum für Luft und Raumfahrt (DLR), 2017; European Space Agency (ESA), 2011). Taking into account the errors for each unit in Table 5.1, the first budget amounts to a total pointing error of 144 arcsec which is much higher than the 20-30 arcsec that is aimed for in subsection 1.1.1. During calibration it again the same ACKE of 10 arcsec is present but the orbit determination will be much better at 2 arcsec (European Space Agency (ESA), 2017). It is also assumed that GALA will operate at a stable thermal point thus no error is included for the thermal stability. Now left is only the calibration residual which is set at 10 arcsec for now, giving a total pointing error 14 arcsec. This is then used in the third pointing budget as the calibration error and here are again the thermal contributions present as are the ACKE and AGKE. Now the total error totals to 28 arcsec, much lower compared to the 144 arcsec. Thus the calibration does lowers the total pointing error a lot to within the acceptable range.

Table 5.1: Pointing budgets for GALA in three different situations. The first shows the budget when GALA would not be calibrated and operate in Ganymede orbit at an altitude of 500 km (GCO500), its mission phase. The second is the pointing budget during calibration, resulting in the calibration error. The third incorporates this calibration error and shows the pointing budget in GCO 500 with the calibration now in place.

Scenario:	No calibration in GCO 500 [arcsec]	Calibration Error [arcsec]	Calibrated in GCO 500 arcsec]
Spacecraft			
Absolute Control Knowledge Error (ACKE)	10	10	10
Absolute Guidance Knowledge Error (AGKE)	20	2	20
Optical Bench			
Settling	140	-	-
Alignment knowledge	14	-	-
Transceiver Unit			
Settling	6	-	-
Thermal stability	6	-	6
Alignment knowledge	14	-	-
Transmitter			
Settling	6	-	-
Thermal stability	6	-	6
Alignment knowledge	12	-	-
Calibration residual	-	10	-
Calibration error	-	-	14
Total Absolute Knowledge Error			
RSS Sum	144	14	28

5.1.3. Pointing Errors during Scanning

During the calibration, a scan is performed that must cross the ground station at some point. Therefore the maximum pointing error during calibration is to be computed and used to construct the scanning pattern. It is of uttermost importance that the ground station location lies within the scan window, defined by the maximum pointing error. Therefore a slightly different approach is used compared to the previous discussion. Table 5.1 presents all values at the 2 sigma or 95% confidence level which means there is still a 5% chance that the actual misalignment is larger. For an ideal Gaussian probability distribution there is no limit to what the maximum misalignment could be, but it is not possible to cope with an infinite misalignment. Therefore the 3 sigma value or 99.73% confidence level is used as the worst case to compute the pointing budget for the maximum misalignment as advised by ESA standards (European Space Agency (ESA), 2011). Table 5.2 presents the budget used to determine the maximum window and this is the window that should be at least scanned for during calibration. Table 5.2 uses the same numbers as the first case in Table 5.1 but now the 2-sigma values are changed to the 3-sigma values. The calibration error is of course left out and instead of using the knowledge errors ACKE and AGKE, now the ACE and AGE are used since based on these numbers, commands will be given instead of post processing the data. The total results in a window of -215 to +215 arcsec both in X and Y direction. However, there is always a possibility that all errors are in the same direction and therefore this worst case results in a window of -333 to +333 arcsec. The value of 333 arcsec is used throughout the rest of the thesis and defines the scan window in all subsequent discussions.

Table 5.2: Total scan window for GALA during laser ranging.

Contributor	Value [μrad]	Value [arcsec]
Spacecraft		
Absolute Control Error (ACE)	109	23
Absolute Guidance Error (AGE)	15	3
Optical Bench		
Settling	1018	210
Alignment Knowledge	102	21
Transceiver Unit (TRU)		
Settling	45	9
Thermal stability	45	9
Alignment Knowledge	102	21
Transmitter		
Settling	45	9
Thermal stability	45	9
Alignment Knowledge	87	18
Total Absolute Pointing Error		
RSS sum	1042	215
Worst case sum	1613	333

So far this discussion was focused on errors that do not change over time during laser operations. However, during operations, whether this is laser altimetry or ranging, the pointing of the spacecraft will change. In the following discussion the focus will be on the errors present during laser ranging that govern how the total pointing error changes over time using the definitions in Table 5.3 and Figure 5.5. Both types of error can be specified in time in multiple ways as visualised in Figure 5.5 for in this case the pointing error (PE). The Absolute Pointing Error (APE) is the instantaneous value of the pointing error e_p at any given time as defined in Equation 5.7, which equivalent to the Absolute Knowledge Error (AKE). The Mean Pointing Error (MPE) is the mean pointing error over a specified time interval, denoted by Δt in Figure 5.5 and presented in Equation 5.8. Then the Relative Pointing Error (RPE) is the difference between the pointing error at given time t and the MPE over a time interval containing that time t, see Equation 5.9. The equivalent knowledge errors are the Mean Knowledge Error (MKE) and the Relative Knowledge Error (RKE) respectively. RPE is also known as pointing stability in various other discussions. These definitions are in accordance with how the requirements for JUICE and GALA are specified and are in accordance with ESA practices (European Space Agency (ESA), 2008, 2011).

$$APE(t) = e_p(t) \tag{5.7}$$

$$MPE(\Delta t) = \frac{1}{\Delta t}\int_{\Delta t} e_p(t)dt \tag{5.8}$$

$$RPE(t,\Delta t) = e_p(t) - \frac{1}{\Delta t}\int_{\Delta t} e_p(t)dt \tag{5.9}$$

To see where these errors come from, let's assume that a certain command is given to the spacecraft to range towards the ground to commence laser ranging. The attitude control system will receive commanded attitudes and will try to achieve this attitude. However, the spacecraft is continuously disturbed and thus the attitude will deviate a bit from the commanded and desired attitude. The attitude control system will sense this deviation and respond in order to keep the spacecraft pointed as required and this sensing is also influenced by noise and errors in the sensors and the response is influenced by the drive mechanisms and their intrinsic error sources. An example of this continuous process is depicted in Figure 5.5 where the error

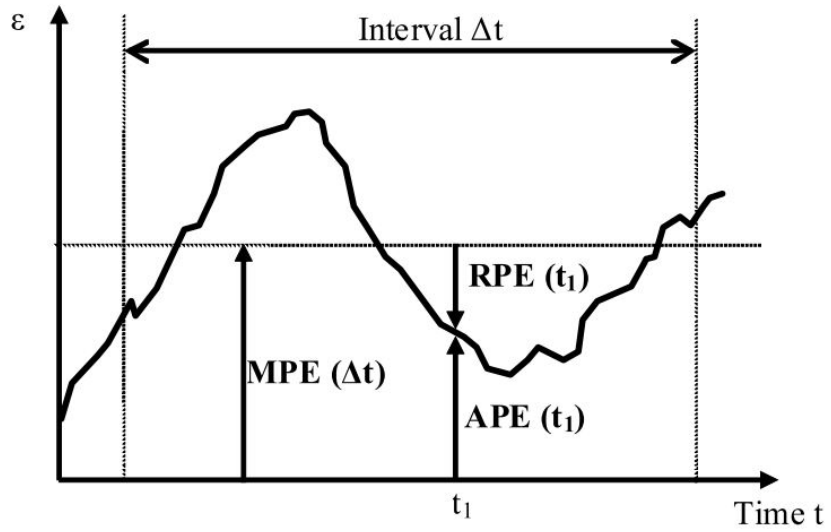

Figure 5.5: Errors in time (European Space Agency (ESA), 2008).

is shown in time. Now the ACE sets a boundary for the maximum deviation from the desired attitude, or error. For example, if a 2 sigma value of 15 arcsec is given, then 95% of the time, the ACE will be within 15 arcsec. Within this boundary it is allowed to continuously deviate from the desired attitude but a number of instruments require that this process is limited. For example for GALA operations it is important that the footprint does not wander to much on the surface from shot to shot (Deutsches Zentrum für Luft und Raumfahrt (DLR), 2017). Therefore, a RPE is specified over a certain amount of time restricting how much the attitude can change within the boundary.

GALA requires a RPE of 2 arcsec over 8.7 ms, 6 arcsec over 100 ms and 10 arcsec over 500 ms (Deutsches Zentrum für Luft und Raumfahrt (DLR), 2017). The first requirement is a result of the fact that the laser pulse time of flight is around 8.7 ms at an altitude of 1300 km, the maximum height at which GALA will operate. Now this laser pulse should stay in the field of view of the receiver and thus the attitude cannot deviate more than this, including aberration and blurring due to motion of the spacecraft. The last requirement over 500 ms makes sure that a consistent laser profile is obtained since the error is to be inside the laser footprint of 10 arcsec for at least 15 shots which is 500 ms at 30 Hz.

Other instruments require also a certain pointing stability and of these instruments, JANUS, the camera, has the most stringent requirements. JANUS specifies an RPE of 1 arcsec over 10 ms and 3 arcsec over 500 ms (European Space Agency (ESA), 2017). These values as given in Table 5.3 will be used in the rest of this study and will govern the attitude model used in Section 5.2. Note that the APE is comprised of the ACE and AGE and the same holds for the AKE which is comprised of the ACKE and AGKE.

5.2. Attitude modelling

The first step in simulating the laser ranging campaign is creating the attitude of the spacecraft resulting in pointing of the laser altimeter. For this the attitude will be described using the three Euler angles and the pointing situation will look like in Figure 5.6. Here the rotation angles around the x and y axes, θ and Φ are varied to create the scanning pattern while the rotation angle around z is assumed to be constant for the entire time and will not be modelled as it does not matter how the spacecraft is rotated around the z axis, as long as it remains constant.

A certain scan rate that is put on the rotation angles will govern the speeds at which the spacecraft rotates, known as slew rate. Together with the shot frequency of 30 Hz it will determine the spacing between the points. The maximum slew rates for JUICE are reported in Table 5.4 and for manoeuvres, the worst axis rate is to be used. This worst case axis rate is the performance under the worst conditions possible e.g. failing of certain control systems while still maintaining full control of the spacecraft. However during scanning a much lower slew rate will be required to make sure the laser pulses can be detected for a significant amount of time with each pass over the ground station, for example the MLA expirement used a scan rate of 0.0009 deg/sec (Smith et al., 2005). The scan rate, along with the duration of the scan will determine the spatial

Table 5.3: Summary of errors used in laser ranging with their corresponding values.

Acronym	Name	Short Definition	Value [arcsec]
APE	Absolute Pointing Error	The instantaneous value of the difference between the actual and desired spacecraft pointing	15
ACE	Absolute Control Error	The instantaneous value of the difference between the actual and desired spacecraft attitude	15
AGE	Absolute Guidance Error	The instantaneous value of the difference between the actual and desired spacecraft position	2
AKE	Absolute Knowledge Error	The instantaneous value of the difference between the actual and known (measured) spacecraft pointing	10
ACKE	Absolute Control Knowledge Error	The instantaneous value of the difference between the actual and known (measured) spacecraft attitude	10
AGKE	Absolute Guidance Knowledge Error	The instantaneous value of the pointing error introduced by difference between the actual and known (measured) spacecraft position	2
MPE	Mean Pointing Error	The mean value of the pointing error over a specified time interval	-
RPE	Relative Pointing Error	The difference between the instantenous pointing error at time t and the mean pointing error over a time interval Δt containing that time t	1 over 10 ms
RPE	Relative Pointing Error	The difference between the instantaneous pointing error at time t and the mean pointing error over a time interval Δt containing that time t	3 over 500 ms

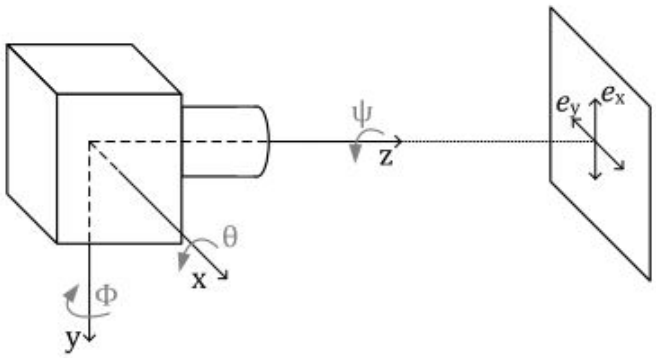

Figure 5.6: Pointing situation for GALA as used in the simulation. The two errors e_x and e_y are to be modelled and added to the commanded attitude. The depicted surface is the scan window to be scanned and will be dotted with the laser shots of which the position will then be influenced by the two errors.

resolution of the laser shots on the ground and the influence of this will be investigated in Section 8.3

Using the locations of the ground station and JUICE, the scan rate and the duration, a commanded attitude θ_{cmd} is created, the desired attitude that will be sent to the spacecraft as commands. However certain errors will appear that will deviate the commanded attitude from the real attitude θ_{SC} of the spacecraft. The noise and pointing errors will be added to the commanded attitude and finally a random misalignment, adhering the maximum expected misalignment from Section 5.1, is added.

Table 5.4: Slew rates for JUICE (European Space Agency (ESA), 2017)

	maximum rate [deg/sec]
X axis	0.32
Y axis	0.75
Z axis	0.21
Worst axis	0.17

5.2.1. Scan patterns

For the scan, different scan patterns can be used of which a sweep is the most common as also used by MLA (Smith et al., 2005). Straight scanning lines are created along the entire scan window separated by a certain distance resulting in a number of lines that consist of a number of points per line. Since the scan window is a square it is possible to create a scanning pattern where the spacing in both x and y is exactly equal through choosing a combination for the slew rate and duration. However when the slew rate is fixed while the duration is increased, only the number of lines will increase, decreasing the spacing between the lines. Figure 5.7 shows an example for the commanded attitude where the blue dots indicate a laser shot assuming an equal spacing with a duration of 4 hours and a slew rate of 0.006 deg/sec or 22.8 arcsec/sec, creating an equal spacing where the spacing between each shot is 0.76 arcsec both in x and y direction.

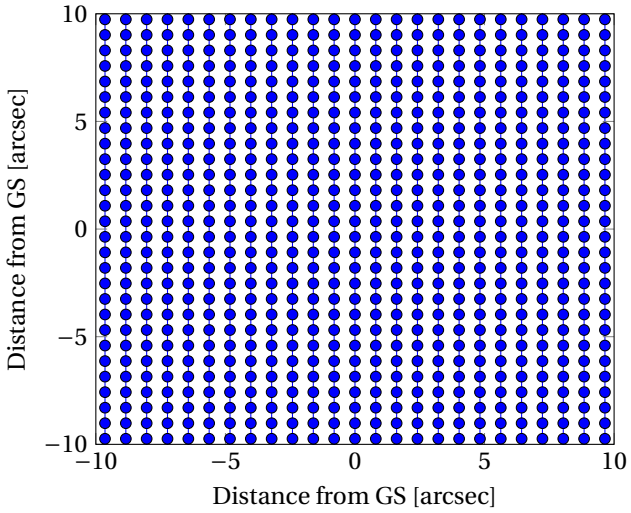

Figure 5.7: Example of a sweep scanning pattern.

The scan is started in the upper left corner going down for an entire line and when it reaches the last shot it shifts to the next line, going up again. This is a key property of this scanning pattern and will be noticed at the ground station when waiting to pick up the signal. Lets assume a line is reached during the scan that passes over the ground station. Going down along the line, it will at some point start to generate a signal at the ground station for a few seconds and then disappear again as can be seen in Figure 6.4, completing the line, shifting to the next and coming back again. As a line in this case takes 68 seconds to complete, it will mean that roughly every minute the ground station will start to receive a signal regardless of its position.

This is different for a vortex scanning pattern as depicted in Figure 5.8. Here the scan is started at the expected position of the ground station, at zero in x and y coordinates. Then, using straight lines, a scanning pattern is created spiralling outwards. When the ground station is at the expected location, it will receive an almost continues signal until the shots have spiralled out far enough that no signal is detectable any more. This makes it easier to acquire the signal since there is more time available before the signal fades and also the range gate can be optimised when the signal is present for a longer period of time. Therefore it is deemed interesting to take also this scanning pattern into account for this thesis. Depending on the slew rate and available scanning time, a number of spirals is determined and the desired attitude is created. Although the spacecraft attitude follows the perfect vortex, the shots are only fired with the finite 30 Hz so not every line consists of the same number of points and ends nicely in the corner. Also the spacing between each point

and its next point in time is still the same, however due to the pattern, the spacing between shots in different lines is different and thus it is no longer possible to determine an exact spacing distance between each point to its nearest neighbours making it different from the sweep pattern.

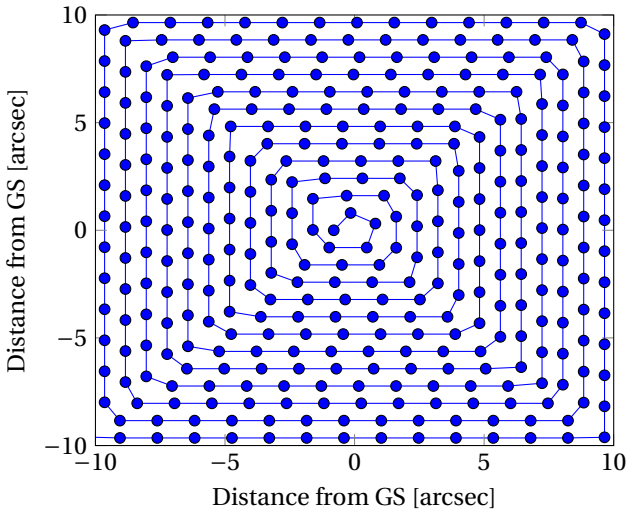

Figure 5.8: Example of a vortex scanning pattern.

5.2.2. Pointing errors

After the commanded attitude is created with one of the two patterns, the pointing errors and disturbances on the attitude are added. Taken from Table 5.3, the three important values that apply here, during laser ranging, are given in Table 5.5, starting with the APE of 15 arcsec. This means that the actual attitude will never have a deviation of the commanded attitude of more than 15 arcsec at 2 sigma or 95 % of the time the attitude will be within 15 arcsec of the commanded attitude. When generating the real attitude including the disturbances, it is possible to check the difference with the commanded attitude a large amount of times and then compute the 2 sigma deviation, checking if this is indeed true.

Table 5.5: Summary of errors used for generating the disturbed attitude

Acronym	Name	Short Definition	Value [arcsec]
APE	Absolute Pointing Error	The instantaneous value of the difference between the actual and desired spacecraft pointing	15
RPE	Relative Pointing Error	The difference between the instantaneous pointing error at time t and the mean pointing error over a time interval Δt containing that time t	1 over 10 ms
RPE	Relative Pointing Error	The difference between the instantaneous pointing error at time t and the mean pointing error over a time interval Δt containing that time t	3 over 500 ms

However it is possible to generate such a signal in many different ways and many instruments actually require the difference between each measurement to be bounded. This is reflected in the two RPE's set at two different time scales. Such a requirement requires that the instantaneous pointing error at a certain point in time is not more than the given value from the mean over which the requirement is specified. So for example for the first one, 1 arcsec over 10 ms, it means that when a point in time is chosen, a mean is determined containing this point and then the difference between this point and the mean is taken, which should not deviate more then 1 arcsec for 95 % of the time. So if this is checked a 1000 times, in 95 % of the cases this should be true. Thus the values in Table 5.5 are used as an requirement to the disturbed signal generated for the simulation.

When a spacecraft tries to reach the commanded attitude, it will turn towards the required attitude and it will take some time for the spacecraft to reach a stable attitude close to the desired attitude with some small jittering still present. Since no model of the attitude and control of JUICE is available yet, it is decided to create an attitude that follows a worst case scenario. In this scenario, the values from Table 5.5 are taken and it assumed that the spacecraft will never do better than these values. This is a safe assumption since in the case that the spacecraft performs better, there is still no way to know this. Furthermore in this scenario never a stable state is reached by the spacecraft, always a changing deviation will be present. If a stable state is used, it will be very hard to comply to these requirements since still a deviation 5% of the time is allowed. The worst case scenario is accomplished by assuming a random stationary process, meaning that the values in Table 5.5 are always describing the random process regardless of time and the disturbances are assumed to originate from control errors. Control errors are assumed to be Gaussian, which is standard practice in industry and also used by ESA (European Space Agency (ESA), 2008) and thus the disturbed attitude can be generated using Gaussian statistics.

The attitude disturbance model strives for the largest difference shot to shot which can be accomplished by generating a pure Gaussian disturbance with a mean at the desired attitude. However this would result in very large jumps in attitude, for example from a deviation of -15 arcsec to +20 arcsec which does comply to the requirement but is not deemed realistic for a spacecraft. Instead the deviation from the desired attitude is generated using a random walk, generated from a Gaussian distribution following Table 5.5. The interpretation of the RPE was given in Equation 5.9 given again here. The relation between the time interval Δt and the time t can be interpreted in different ways and depends on the application (European Space Agency (ESA), 2008).

$$RPE(t,\Delta t) \quad = \quad e_p(t) - \frac{1}{\Delta t}\int_{\Delta t} e_p(t)\,dt \tag{5.10}$$

- A time t is randomly chosen and the mean is computed over the time interval $t-\frac{1}{2}\Delta t$ to $t+\frac{1}{2}\Delta t$, where t is thus in the middle of the interval.
- A time t is randomly chosen and the mean is computed over the time interval $t-\Delta t$, meaning that the relative error is the end state of the attitude at this interval.
- A time t is randomly chosen and the mean is computed over the time interval $t+\Delta t$, meaning that the relative error is the begin state of the attitude at this interval.
- A time interval Δt is randomly chosen and a random time t within this interval is chosen.

The first one is defined as the worst case in the ESA pointing error handbook (European Space Agency (ESA), 2011) and allows indeed for the most deviations in the attitude. Thus Equation 5.10 is altered into 5.11 and will be used to check for the requirements put on the disturbed attitude by choosing many random points and calculating their RPEs.

$$RPE(t,\Delta t) \quad = \quad e_p(t) - \frac{1}{\Delta t}\int_{t-\frac{1}{2}\Delta t}^{t+\frac{1}{2}\Delta t} e_p(t)\,dt \tag{5.11}$$

First a random walk is generated with a time step of 500 milliseconds and an 2-sigma of 3 arcsec, following the fist RPE requirement. This random walk is bounded such that it keeps the 15 arcsec APE requirement. The bound is created by detecting a deviation of more than 12.5 arcsec which activates a different random walk where the next step is only allowed to decrease the deviation and not increase it any further. Thus the deviation will decrease to a value of lower than 12.5 arcsec and is then allowed again to both increase or decrease the deviation. This was found to be a very suitable algorithm to acquire a total deviation of 15 arcsec for 95% of the time. This signal is the long period attitude disturbance and is smoothed to remove the sudden large jumps as they are not deemed realistic at this scale as shown in Figure 5.9a. This signal adheres to the APE of 15 arcsec but the RPEs at 500 millisec and 10 millisec are too low. Therefore two high frequency noise signals are added with 2 sigma values of 3 and 1 arcsec, recreating the RPEs as requested. After extensive testing and tuning the boundary of the random walk, the disturbed signal is created as shown in Figure 5.9.

The high and low amplitude noise is created by using the prescribed amplitude and then finding a time interval per which a new value is generated. So for the high amplitude noise the time interval is 40 ms as given in Table 5.6, so every 40 ms, a new deviation is created using a Gaussian distribution. This creates a signal

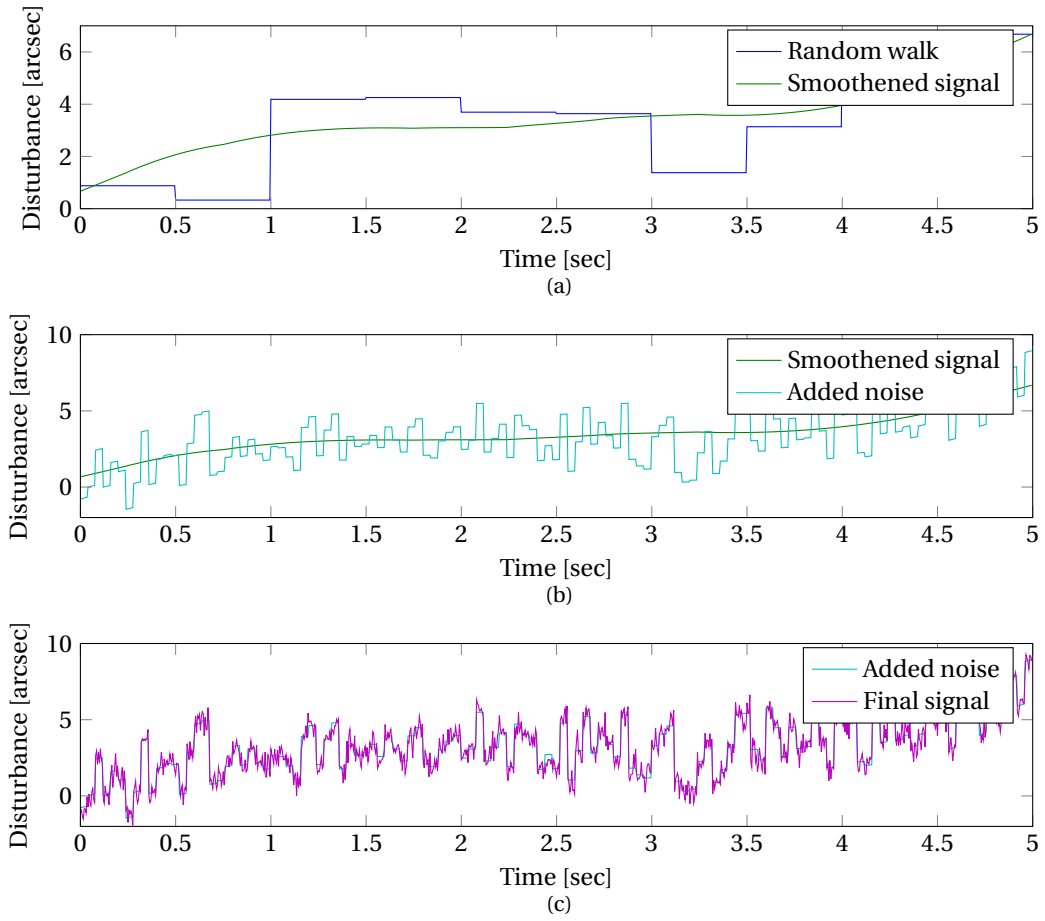

Figure 5.9: Synthesis of the disturbances on the attitude by creating a random walk and smoothing this (a) and introducing a random Gaussian with 2 sigma values of 3 (b) and 1 (c).

Table 5.6: Summary of values used to created disturbed attitude

	2-sigma value	Time interval
Random walk	3 arcsec	500 ms
High amplitude noise	3 arcsec	40 ms
Low amplitude noise	1 arcsec	5 ms

with an RPE of 3 arcsec and the same goes for the low amplitude noise. As these specifications apply to each axis, for each axis a noise signal is created that is then added to the commanded attitude. The misalignment error is simply a bias error that is assumed constant during the entire laser ranging time. This is practically achieved by making sure that the laser is warmed up by operating it already of one to two hours before laser ranging is commenced. Doing this ensures that the laser is at a thermally stable point such that deformations due to thermal fluctuations can be neglected. For each simulation, the misalignment is randomly generated using the maximum values from 5.1.

This model creates a worst case attitude disturbance and probably is performing worse than the real control system installed on JUICE. The used RPE's are the most stringent requirements from the EIDA European Space Agency (ESA) (2017) and thus the model is for the short period deviations deemed realistic. The long period random walk is deemed less realistic as the control system is probably performing better than de worst case created here in the sense that it tries to go to a more stable situation. The deviations will then be larger at the end of scan lines, since the scan line is shifted to the next one, created a larger deviation and then it will get more stable as time progresses. It would be helpful to retrieve information on these settling times for the scan lines or to acquire a sophisticated model that includes both the spacecraft physics and the control

system performance. However the design is not yet such a level that this is readily available at this point in time.

It is also possible to adhere to the requirements set in Table 5.5 by adding up purely Gaussian errors. It is interesting to see what the difference is compared to the random walk and if indeed the random walk is the worst case possible. Such a signal is depicted in Figure 5.10 where the different frequencies can easily be distinguished. Two different Gaussian distributions are used here, one with a 2-sigma deviation of 7.5 arcsec which is used over a time of 2.25 sec, exactly creating a disturbance that is within 15 arcsec for 95% of the time and also 95% of the time within 3 arcsec over 500 ms. Finally a high frequency noise is added to make sure the signal also adheres the RPE of 1 arcsec over 10 ms. The differences between the two models for the attitude disturbance will be treated in Section 8.2 where a comparison will be made.

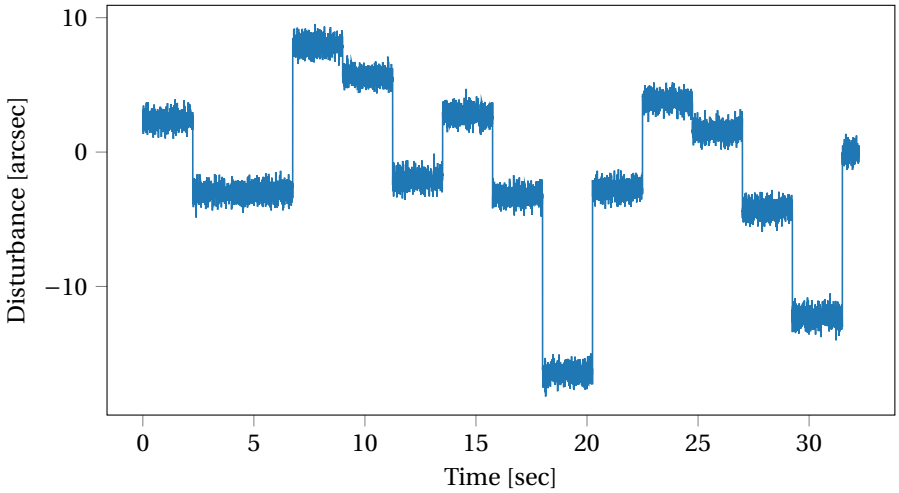

Figure 5.10: Attitude disturbance created using only purely Gaussian statistics.

6

Development of the simulation tool

The accuracy of the calibration will not depend on a single shot and instead a large amount of shots will be combined in order to improve the accuracy of the calibration. To be able to determine the accuracy of this procedure a tool is developed where the trajectory of JUICE determines the geometry of the laser ranging simulation while the actual laser ranging is simulated using the tool. The purpose of this chapter is to guide the reader through the various steps performed in the tool and show that this tool is working correctly and can be used to make a qualitative and quantitative assessment of a laser ranging campaign. Section 6.1 will elaborate on the lay out of the model and introduce the various blocks of which it is composed. Then Section 6.2 will explain how the location of the ground station is estimated. Now that the entire model is complete it is verified for its correct working in Section 6.3 after which it is validated using two previous experiments in Section 6.4.

6.1. Model Flow

The simulation consists of several parts where certain tasks are performed. The first part deals with setting up the operation of JUICE by creating the scan pattern based on the slew rate, scan window and the chosen scan pattern following Section 5.2. This results in a commanded attitude for each laser shot. Here it is assumed that this information is also available when laser ranging is performed real life. In the real situation, each laser shot is timed and also the time of the commands to the spacecraft are timed. Thus combining this information will lead to a commanded attitude for each shot. Since the shots are fired at a frequency of 30 Hz and the clocks on GALA and JUICE are much better than required to time shots at 30 Hz, it is a reasonable assumption that this information will be available. For example the clocks on GALA are able to time at sub nanosecond level while the time between each shot is 33 millisecond. The next step is to add the disturbances encountered by the spacecraft during laser ranging. For both the x and y attitude coordinates a disturbed signal is created. This is the actual, true attitude of the spacecraft and this will be used to generate the rest of the simulation as shown in Figure 6.1.

SPICE (Navigation and Ancillary Information Facility (NAIF), 2017) is used to determine the positions of JUICE and the ground station and elevations of JUICE and the Sun. Using the positions, a vector is created for each laser pulse resulting in the distance r to the ground station and the range z required by Equation 3.3 to determine the amount of photons reaching the ground station for each pulse. Then the mean number of detectable photons is determined using Equations 3.18 and 3.19.

6.1.1. Pulse detection

Laser shots will be detected using a linear operating APD as discussed in Section 3.5, that is essentially open all the time receiving photons continuously creating a voltage that corresponds to the intensity of the received signal, which can be read out and recorded by digital equipment. Later this data can be assessed in various ways to see if any pulses can be discriminated from the noise. Pulses will appear as an sudden increase in signal due to the temporal profile of the pulse and if multiple pulses at a fixed frequency are detected, it will also provide evidence that these are pulses as noise is randomly distributed and not with a fixed frequency. This can even be done visually where a print out is used of all the pulses received in time and intensity.

However to be able to run many simulations and produce a statistical significant result an automated way

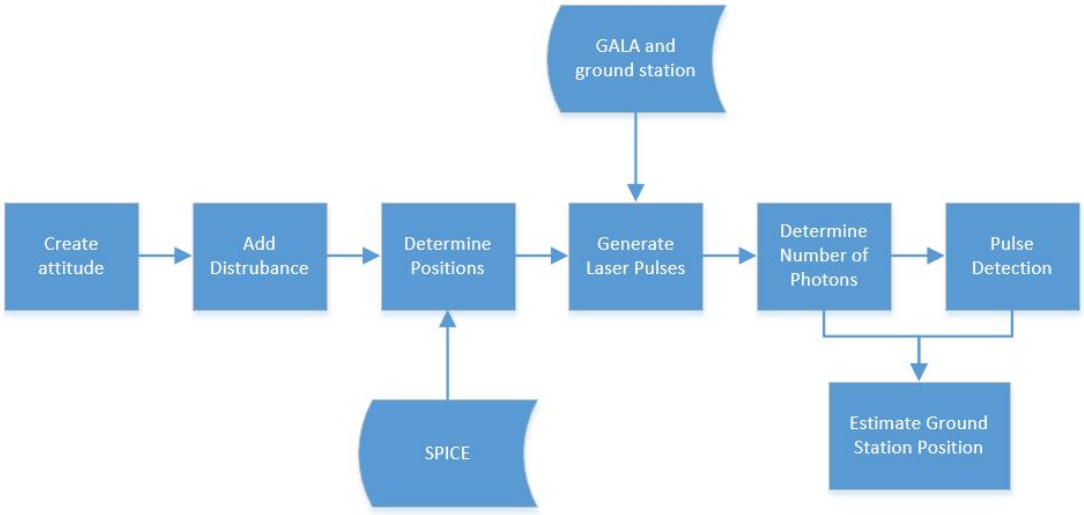

Figure 6.1: Flow diagram for the simulation model

for detection of the pulses is used by employing threshold detection as was explained in Section 3.5 using range gates and range bins. Since the APD is essentially open all the time and the frequency of the pulses is 30 Hz, each second is divided into 30 range gates of a length of 0.033 sec, which is essentially the worst case range gate length. The bin size is chosen such that it captures 99% of the Gaussian laser pulse produced by GALA and is set at 17.4 ns. It is assumed that the range gates are synchronised with the laser shots such that every range gate contains one laser shot exactly. For each pulse or range gate then the pulse intensity of the shot is computed along with its noise levels. Thus the number of range gates and pulses are the same.

Based on the intensity of the received signal and the threshold se,t each range gate is assigned a probability of detection of the pulse in accordance with Equation 3.34. Based on the probability, it is decided whether or not the pulse is detected by generating a random number and check if this number is above or below the given probability. The same procedure is done for the probability of false detection governed by Equation 3.37. Then both detections are combined into the information available to estimate the position of the ground station as will be discussed next in Section 6.2.

6.2. Estimation of the ground station location

Two types of data are available from the simulation at this point, photoelectrons intensities for each shot, and information on whether or not a detection took place in a range gate. At this point it is not clear if photoelectrons intensities will be available since this will depend on the equipment used and furthermore the precision of these measurements is unknown if the equipment is not precisely known. Therefore also estimation of the ground station using only pulse detections will also be investigated as it is for sure that this information is available.

The first idea behind the estimation of the ground station is that the pulse hitting the ground station the closest will indicate the most probable location of the ground station. Thus finding the highest intensity among the data is the simplest concept for finding the ground station. If no intensity data is available one could see when the detected shots were fired, corresponding to an attitude of the spacecraft and estimate using this the location of the ground station. For example a number of shots were detected when a sweep was made when the attitude of the spacecraft was at 100 arcsec from the proposed ground station location. Thus a misalignment of 100 arcsec is present made up by the misalignment and the attitude knowledge error. Let's assume that a certain threshold was set such that a pulse was detected up to 10 arcsec from the middle of the laser beam. Thus the middle of the laser beam could be at either 90 or 110 arcsec from the ground station. Furthermore the difference between the desired attitude and the actual attitude is 15 arcsec as explained in Section 5.1. Thus the middle of the laser beam could actually be at 75 or 125 arcsec from the ground station when a pulse was detected. Thus the estimation accuracy will be around 25 arcsec or worse, depending on the threshold set. For example at closer distance, using a low threshold, a pulse is still detectable even at 15

arcsec from the middle of the Gaussian beam profile. This estimation accuracy of 25 arcsec is to large to be used in the total pointing budget in Table 5.1 giving the need for a more sophisticated estimation method.

To do better than in the aforementioned discussion, a estimation procedure is developed that makes use of the Gaussian intensity profile for a laser pulse. This will create distribution of detected shots following this Gaussian profile. The Gaussian beam profile given in Figure 3.1 shows a clear top intensity at the middle of the profile. If the position of this highest intensity could be estimated the accuracy would be much better. This could be achieved by setting a very high threshold such that only pulses around the top would be detected. However then only a few pulses would be detectable, reducing the total chance of detection to an unacceptable low level. Furthermore the 15 arcsec uncertainty in pointing of the spacecraft would still be present. If one would just fire away as many shots as possible, statistically, the amount of detected shots should increase when the distance to the ground station decreases. Ideally the distribution of detected shots will be exactly the same as the Gaussian beam profile and thus a top can be identified and used as the ground station location. Now it does not matter if the shots are fired with an error of 15 arcsec since the distribution of detected shots gives away when it was fired. When a sweep is made by the spacecraft and a high number of shots is detected, this will likely be a sweep close to the ground station. A sweep further away will generate less detections and a sweep closer will generate even more detections. Combining all this information, the Gaussian pulse shape can be reconstructed with a certain accuracy and from this the location of the highest intensity can be determined. This point is then the position of the ground station and with this method both errors rising from the pulse shape and the attitude are resolved.

Following this concept an estimation algorithm is developed. The first step is to make a rough estimation of the location of the ground station. The pulse with the highest intensity is taken as the initial position of the ground station and serves as the starting location for the rest of the estimation.

In the ideal case, the shots and their strengths should follow a Gaussian distribution since the signal was a Gaussian as discussed in Equation 3.3. Thus using the data, a Gaussian curve can be fitted using Equation 6.1, which is a simplified version. The ground station position can be varied through Equation 6.2 and the peak intensity I_0 and the width of the pulse w are also estimated.

$$I(r) = I_0 \exp\left(\frac{-2r^2}{w^2}\right) \tag{6.1}$$

$$r = \sqrt{(x - x_{GS})^2 + (y - y_{GS})^2} \tag{6.2}$$

To fit the data a least squares curve fitting algorithm is used that employs the Levenberg-Marquardt method (Moré, 1978). Here the method is used to find a local minimiser when $F : R^n \text{ -> } R^m$ with $m \geq n$ for:

$$\Phi = \frac{1}{2}\sum_{i=1}^{m} f_i^2(x) = \frac{1}{2}||F(x)||^2 \tag{6.3}$$

Where

$$f_i(x) = y_i - M(\boldsymbol{x}, t_i) \tag{6.4}$$

Here y_i is the measured data corresponding to t_i, i.e. the measured detections or photon intensities. $\mathbf{x}$ are the independent variables, the x and y coordinates of each shot and t_i are the parameters to estimated, the ground station position, the width and the peak intensity. Least squares fitting is computationally efficient and when the errors are assumed to be normally distributed with a zero mean and equal variances, the least squares estimate coincides with the maximum likelihood estimate. And even when this is not the case the Markov-Gauss theorem states that least squares estimate provides an estimate with the smallest variance. This makes least squares curve fitting a good candidate for this purpose. The Levenberg-Marquardt method can be seen as an damped Gauss-Newton method and is more robust and widely used for this type of problem. It can be used to determine the ground station position immediately using the signal strengths acquired by the simulation.

However this does not work immediately when given only data about whether or not the pulse is detected since detected and non-detected pulses are simply represented by a 1 and 0, respectively. Fitting a Gaussian to just 1's and 0's does not work and thus an immediate step is performed to make a distribution of detected shots as mentioned before. Instead of having pulse shot locations with a 1 or 0, a grid is created with a certain grid size. For example a grid size of 2 by 2 arcsec is used to create a grid pattern and in each grid the detected

pulses are counted. Then for each grid location, the number of detected pulses is assigned. From the Gaussian curve, more pulses should be detected if the ground station is closer by and thus it is possible again to fit Equation 6.1 to the grid locations with their number of detected pulses. A range of grid sizes ranging from 1 arcsec to 7 arcsec is used to find the ground station position and in the end the mean of these locations is used as the final result.

Using the known x and y position of the ground station and the estimated x and y position of the ground station, an estimation error is determined. This error is just the difference between the estimation and true position and is the final outcome of the simulation. This will be done in two cases, using the signal intensity data and using the detected pulses. In practice one would analyse the data extensively and try numerous approaches to identify pulses and from there estimate with what attitude these pulses were sent. Here it is assumed that each signal is distinguishable from each other one, thus it is always known which received pulse belongs to which sent pulse in time. Then from the time, the commanded attitude can be found and it is also assumed that this is known. Then automatically the ground station position is determined by the simulation, providing a way to test this a large number of times and gain statistics on this approach.

6.3. Verification

The simulation is verified in various ways to ensure the correct working. First the correct working of the photon intensities and the ideal scan pattern is verified. Then the attitude disturbance is added and this is checked again. Based on the pulse intensities the pulse detection should function correctly as will be verified next. After this signal noise is added and the false detections are verified for multiple thresholds. Based on this the estimation of the ground station is verified when no attitude disturbance is present. Table 6.1 presents the used values for GALA and the ground station Wettzell used in this reference case where the quantum efficiency is set to the worst case of 0.2 and the bandwidth of the spectral filter to the common value of 2 nm. This reference case is option 2.3 discussed in Chapter 7 and here laser ranging is performed at a distance

Table 6.1: Summary of values used for the reference case for verification.

Property	Value
Pulse Energy	0.025 J
Beam divergence angle (half cone)	10.3 arcsec
Pulse width (1-sigma)	2.9 ns
Shot frequency	30 Hz
Aperture diameter	0.75 m
Field of View (half cone)	9 arcsec
Receiver efficiency	0.5
Quantum efficiency	0.2
Spectral bandwidth	2 nm
Case identifier	2.3
Mean range	33501982 km (0.23 AU)
Start time	2024 OCT 17
Stop time	2024 OCT 17

of 0.22 AU to Wettzell for a duration of 4 hours. Two options are available, night time ranging and daylight ranging. Initially everything will be verified using night time ranging only to be able to assess and compare results, the simulation will then run from 2 AM to 6 AM. When also solar noise is included for pulse detection, the simulation will be run from 5 AM to 9 AM, where the Sun also rises. In this case, an elevation change of both JUICE and the Sun is present and the Sun rises above the horizon during this time interval providing also solar noise. The elevations of JUICE and the Sun are presented in Figure 6.2 showing the 17th of October 2024 from midnight to midnight. JUICE has a fairly high elevation reaching 70 degrees at its maximum and laser ranging could start at night but after some time the Sun rises above the horizon, inducing solar noise in the simulation which can then also be verified for its correct working.

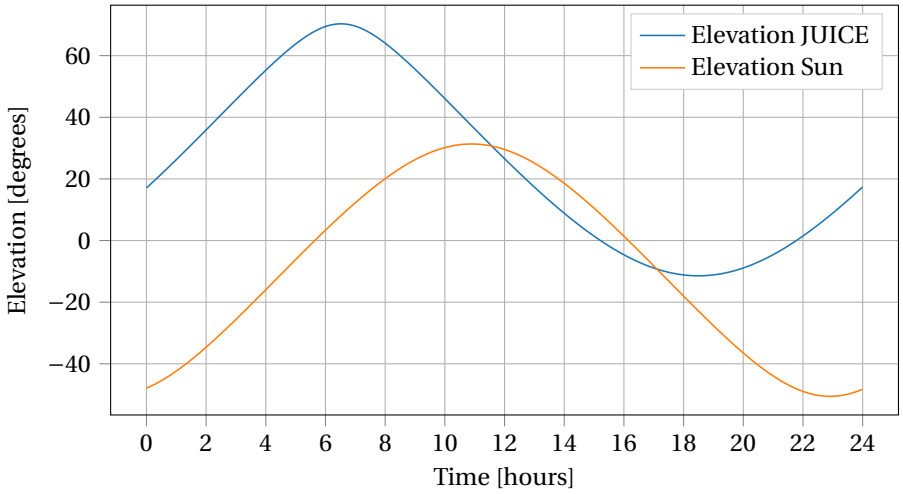

Figure 6.2: Elevations of JUICE and the Sun as seen from the Wettzell ground station from midnight to midnight.

6.3.1. Photons Intensities

The first step is to determine if everything works correctly when no disturbances are introduced. For the model to successfully simulate the received intensity, the link budget in Equation 3.18 is the first step in the verification. This was evaluated for the reference case and reviewed by the team in Wettzell (Schreiber, 2017). The team agreed with the link budget presented in Figure 6.3 which simulates a single pass directly over the ground station.

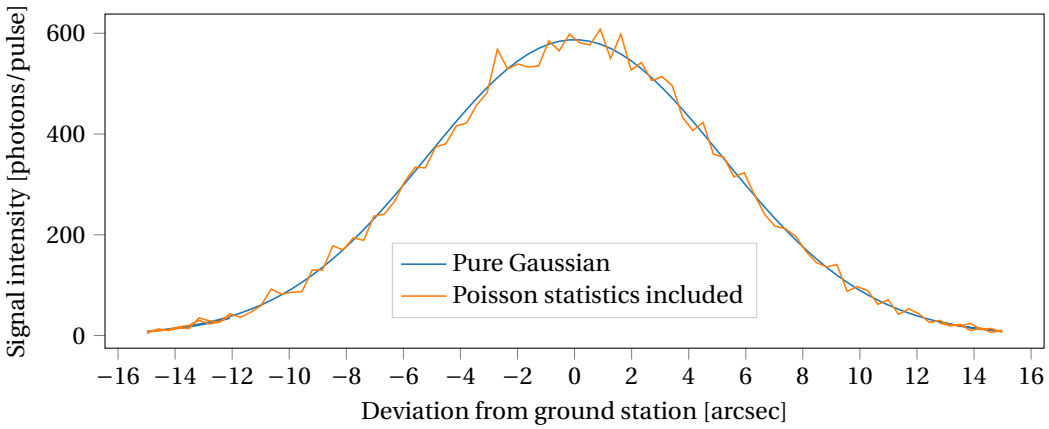

Figure 6.3: Signal intensity during one pass exactly over the ground station.

Both the perfect Guassian shape from Equation 3.3 is visible as is the included Poisson statistics introduced in Equation 3.19 that creates a more random signal around the perfect Gaussian. Since the values were agreed on by the team at Wettzell (Schreiber, 2017) and represent, after careful checking, realistic numbers, the model is verified to produce correct photon intensities.

This result can be used for all shots and the result is shown in Figure 6.4a where the dots indicate the mid point of each laser pulse and the colour indicates the number of received photons for that pulse. Only a window around the ground station of 40 by 40 arcsec is shown, where the ground station itself is located exactly at 0,0, since beyond this window nothing significant is received. Thus this figure shows the view from JUICE and its attitude.

The Gaussian pulse shape is clearly visible with its centre almost exactly at the ground station. The peak intensity does not concentrate exactly at the ground station for two reasons; during the scanning the elevation changes a bit and thus it can be possible that a shot just next to the ground station has a higher intensity because the elevation is increased. The other effect is the Poisson distribution used for modelling the detected

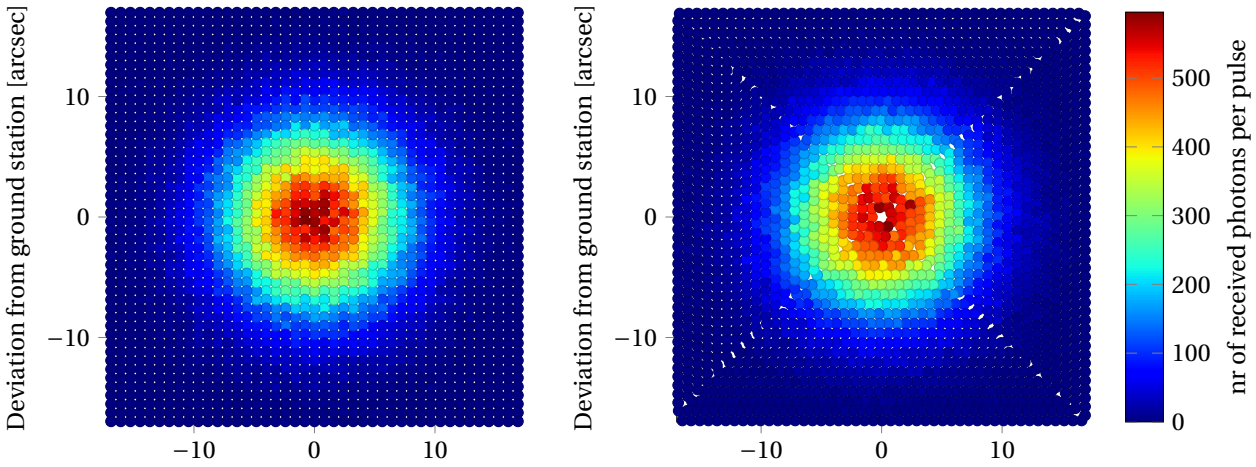

(a) Sweep scan pattern

(b) Vortex scan pattern.

Figure 6.4: Scatter plots showing the pulses and their intensities for the reference case.

photons, generating received photons that do not follow a Gaussian exactly thus verifying the correct function of this functionality. Further more it can also be seen that the half cone divergence angle of 10.3 arcsec is a fairly good indicator for where the number of pulses goes to a very low level, visible in both figures. The same results are attained for a vortex scan pattern where the difference of the pattern is clearly visible in Figures 6.4b and does follow a proper vortex pattern as envisioned.

Disturbed Attitude

Now the attitude disturbances as discussed in Section 5.2 is added to the simulation. Here again the commanded attitude pattern is created and the pulses are fired at the right time as commanded. However due to the unknown attitude disturbance, the shots will be fired with an different attitude than was commanded since the knowledge of the attitude is now limited. Figure 6.5a shows the effect of this and the result is indeed very different. Here the information on the pulse locations is still the same as in Figure 6.4a but the pulses were transmitted with a different attitude than commanded and thus end up somewhere else, creating different intensities than one would expect. Sometimes the disturbance causes a vertical sweep that is close to the ground station, to be further away than expected and vice versa. The vertical shifts are caused by the deviation in y attitude that causes a sweep to be earlier or later at the ground station. The horizontal spread is caused when a sweep is performed with a deviation in x, where sometimes a sweep is already close to the ground station while it should not be, and the other way around. Thus the intensity pattern becomes more spread out in a random manner. This random behaviour is clearly visible in Figure 6.5b where the locations of the shots is shown when the attitude knowledge would be perfect. These dots represent the actual locations of the transmitted shots with their intensity and shows what is actually simulated. There the Gaussian shape is again clearly visible and thus the idea of estimating the location based on the Gaussian shape of the pulse intensity should still work. Using this simulated information from Figure 6.5b, the intensities are combined with the knowledge about the location of the transmitted pulses resulting again in Figure 6.5a. This is the information available for the ground station location estimation.

Figures 6.6a and 6.6b show the same results but now for the vortex scan pattern. Again the real attitude shows the Gaussian shape as expected while the commanded attitude is very different. In this case the view from the commanded attitude strongly depends on the misalignment as here no misalignment is present, the ground station is located exactly where the pattern starts. When the ground station would be far away from the middle of the vortex, the commanded attitude would resemble much more that of the sweep scan, except when the ground station is located near a corner where the movement changes from horizontal to vertical or vice versa. In all these cases the simulation provided expected results and thus it is verified that the addition of the attitude model functions as envisioned.

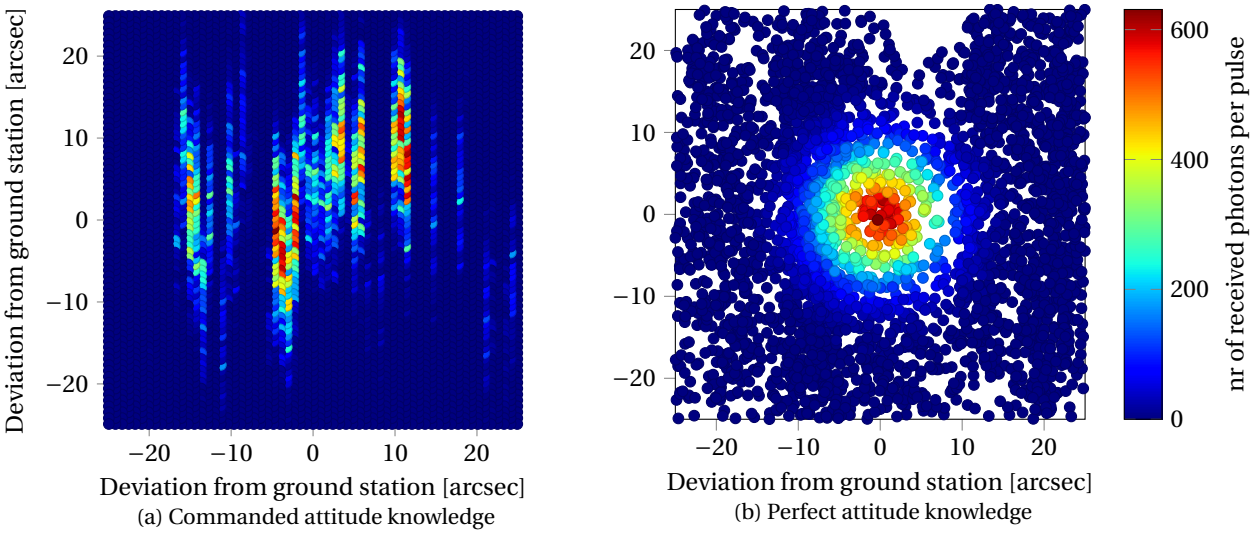

(a) Commanded attitude knowledge (b) Perfect attitude knowledge

Figure 6.5: Scatter plots for a sweep scan pattern showing the pulses and their intensities for the commanded attitude knowledge and the perfect attitude knowledge.

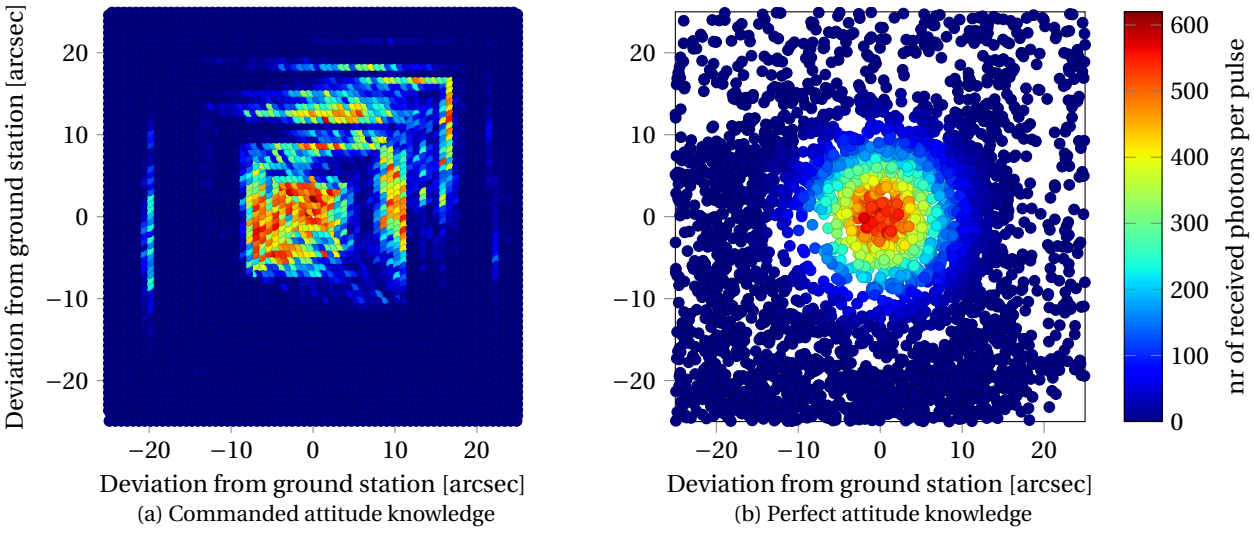

(a) Commanded attitude knowledge (b) Perfect attitude knowledge

Figure 6.6: Scatter plots for a vortex scan pattern showing the pulses and their intensities for the commanded attitude knowledge and the perfect attitude knowledge.

6.3.2. Pulse Detection

From the simulated photon intensities, the correct number of detections should follow. Using the single pass of the ground station as presented in Figure 6.3, the probability of detection should also follow the intensity of the signal accordingly as governed by Equation 3.34. This is shown in Figure 6.7 where for the same pass the probability of detection is plotted. As soon as the laser shots get close to the ground station and cross the threshold of 15 the probability starts to rise rapidly. The fluctuations are caused by the Possion fluctuations in the intensity of the signal and are thus expected.

Another important part of pulse detection is the fact that also false pulses will be identified due to the dark noise and the solar noise as was discussed in Section 3.5 leading to Equation 3.38. Figure 6.2 showed the elevations of the Sun and JUICE and indicates that during the laser ranging, the Sun rises and should start to generate noise. This is visible in Figure 6.8 where the solar noise rises along with the elevation of the Sun. It does not follow the Sun elevation exactly since the elevation of JUICE also influences the noise as was discussed in Equation 3.22. The probability of false detection rises accordingly with the solar noise. Three different threshold settings are plotted to show the behaviour of the probability of false detection. This

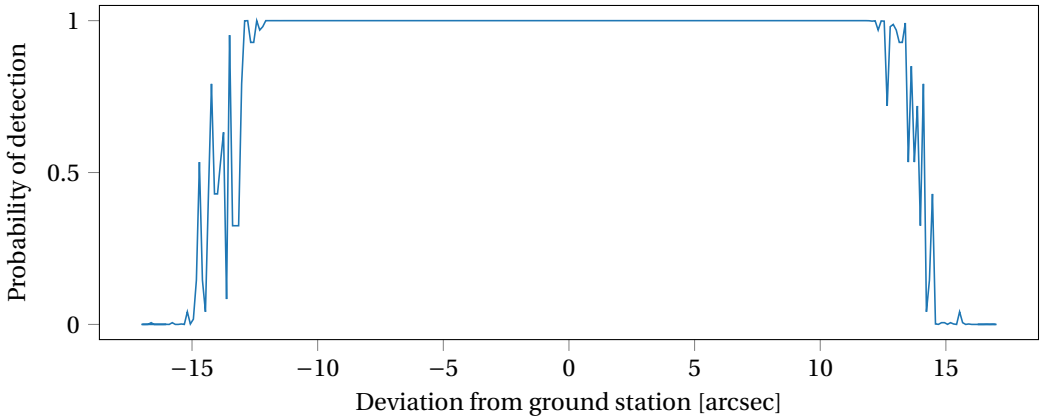

Figure 6.7: Probability of detection for a single pass directly over the ground station with threshold set at 15 photoelectrons.

number is determined using a worst case range gate of 0.033 seconds and a bin size of 17.4 ns which includes 99% of the laser pulse of GALA. The dark noise is set at 4 kHz, the reference value. A threshold of 5 produces a probability of false detection of 1 for most of the time and is thus in this case not a good setting. A threshold of 10 results in a maximum PFD of 0.02 while 15 results in 10e-6. Thus by setting the threshold just a bit higher, the probability is heavily influenced as expected.

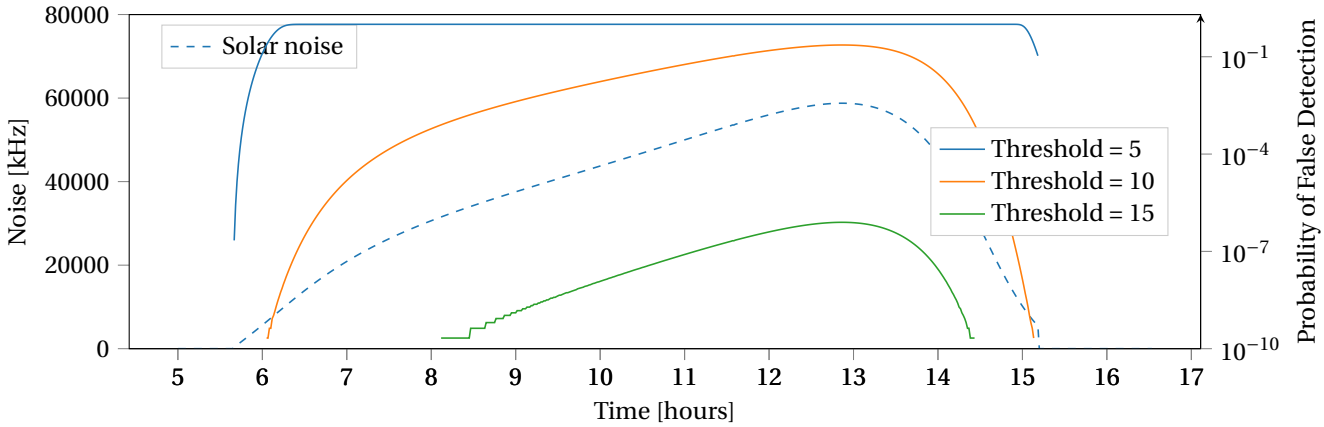

Figure 6.8: Probability of false detection for three different threshold settings for the entire day.

The noise levels were verified by reproducing the values found in (Degnan, 2002a) for the scale energies required to overcome the different noise contributions. It was found that this matched the values found by Degnan within an acceptable error. However a noise count of around 400 kHz was mentioned during the visit to Wettzell (Schreiber, 2017) and this is clearly much lower and not reproducible by this model using these values. This could be because all values such as solar irradiance, efficiencies and field of view are ideal values and because of the assumptions are creating the worst case scenario for the solar noise. However it is also possible to induce the practical value found by Wettzell and check that case. However then the signal strengths should also be corrected but there is no information available to base this on. In the end it is the contrast between detected pulses and false detections that will determine the final result when ranging is background noise limited and thus it is deemed acceptable that for both the noise and the signal the same models and values are now used creating an equal assessment.

This contrast is illustrated in Figure 6.9a where again a scatter plot is shown as before where a blue colour indicates an undetected shot and a red a detected one. Both successful detections as well as false ones are included and although the noise level is fairly high, the location of the ground station is still clearly visible. Note the increasing noise from left to right due to the rise of the Sun, increasing the elevation and thus the noise.

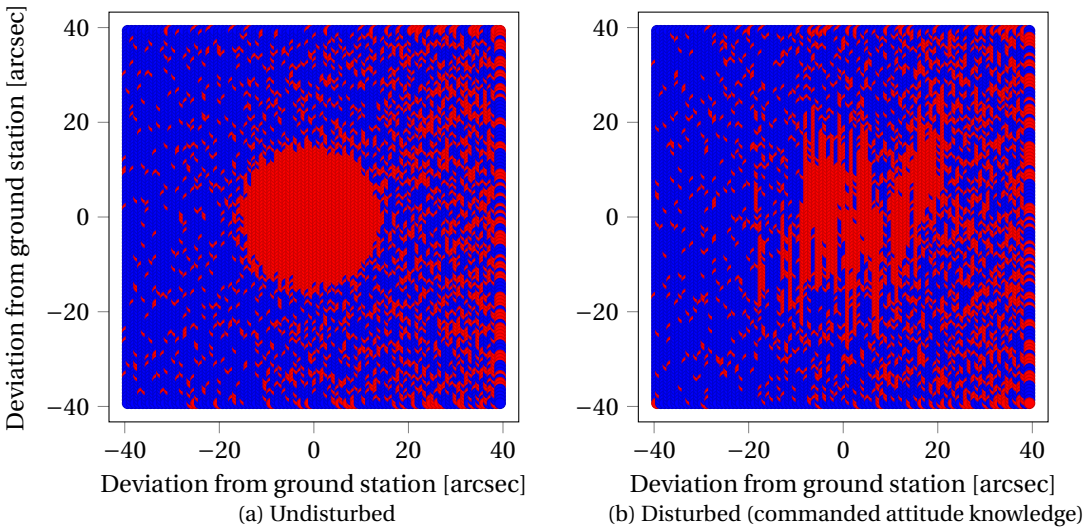

(a) Undisturbed

(b) Disturbed (commanded attitude knowledge)

Figure 6.9: Scatter plots with detected pulses shown in red for a threshold set at 7 photoelectrons.

This verifies the correct functioning of both the detection of pulses and the false detections. From comparing the profile around the ground station with the probability of detection in Figure 6.7 it the sudden border of the pulse detections around the ground station is explainable by the sudden drop in detection probability. Also the the results from the disturbed attitude in Figure 6.9b show the expected behaviour compared to Figure 6.5a and thus is working correctly.

6.3.3. Estimation of ground station

From both the signal intensities and the detected pulses, the ground station position should be estimated reliably in order to be able to conclude something on the accuracy of this estimation. Therefore the estimation is first tested under the most simple conditions, no attitude disturbances and good photon intensities. Furthermore no Sun noise is allowed for now and the reference case from Table 6.1 are used to be able to assess the algorithm without being influenced by other parameters.

The misalignment is randomly generated for its x and y position for each run with the a maximum magnitude that falls within the scan window and each time the difference between this generated misalignment and the estimation is taken as the error. A sweep scan is used set at 0.006 deg/s leading to an equal spacing in x and y of 0.76 arcsec between the shots.

Figures 6.10a and 6.10b show the convergence of the average error and the standard deviation. The simulation was run 1000 times and for each run the average and standard deviation are updated, converging to the average and standard deviation of the 1000 runs in total. Also the change of these values are shown and it can be concluded that after 500 runs, the change of the quantities is less than 1% and thus is converged to its final value. Also when running the simulations using a vortex scan pattern, the same rate of convergence is found. Therefore it can be concluded that indeed the estimation is consistent over many runs and can be reliably used.

The average error in this case is 0.035 arcsec for the x coordinate and 0.014 arcsec for the y coordinate and the standard deviations are 0.024 arcsec and 0.018 arcsec respectively. Given a spacing of 0.76 arcsec between each shot the algorithm performs well and is able to estimate the ground station position very precisely and much better than the value proposed in Table 5.1 of 10 arcsec. The estimation for y seems to be better than for x and this can be explained by the scanning pattern. In the sweep scanning pattern, each sweep is done at a fixed x location and then the sweep is performed by changing y gradually. Then a sudden step in x is performed starting the next sweep. This is reflected in the data as well and thus for the y position, smooth gradually increasing data is available while for x this is not the case. This effect is not present when a vortex scanning pattern is used and thus the errors and standard deviations should be approximately the same in that case. This is confirmed by running the same simulations but then for a vortex scanning pattern. The results are shown in Table 6.2 where indeed the average errors in x and y are 0.055 and 0.057 respectively and also the standard deviations are close to each other for x and y. The mean errors for x and y should approach zero and this is indeed the case with a the largest mean at 0.091 arcsec as found in Table 6.2.

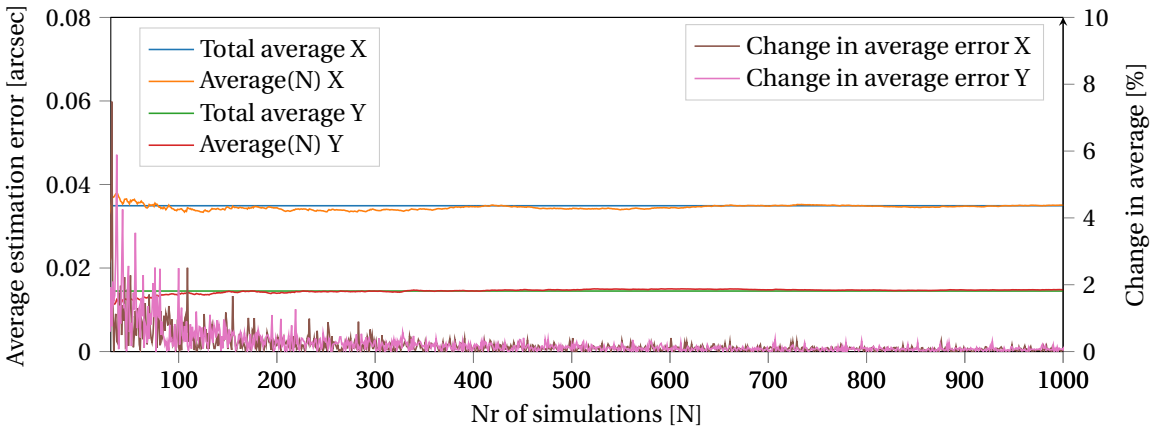

(a) Convergence of the average estimation error

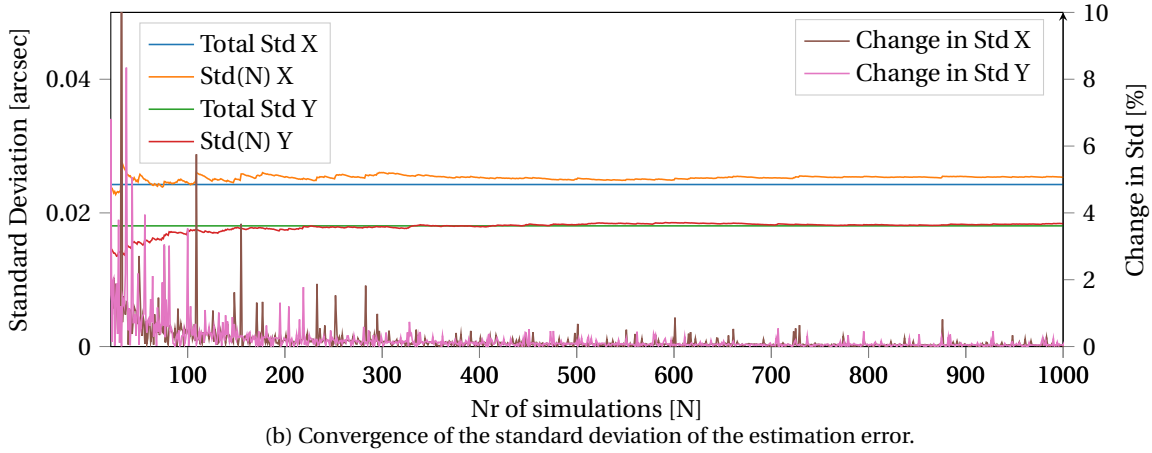

(b) Convergence of the standard deviation of the estimation error.

Figure 6.10: Convergence and accuracy of the ground station estimation using a sweep scan pattern.

Now the same set of simulation settings are used but this time the estimation is done using the detected pulses. Again a convergence within 500 runs is found for both the average and the standard deviation and the resulting values are summarised in 6.2. As expected, the estimation errors are larger since essentially information is lost through the process of detection. However the worst accuracy is still 0.11 arcsec which is still very good. Again the difference between x and y is seen when using the sweep while this difference is gone when using the vortex.

When the estimation is done using photons, it is also worth to have a look at the estimation of the peak intensity I_0 and the divergence angle w that were given in Equation 6.1. Both these quantities also converged as rapidly as the other quantities and the mean peak intensity is almost 500 photoelectrons for the sweep pattern and 433 photoelectrons for the vortex pattern. Their standard deviations are almost the same at 72 and 77 photoelectrons. From Figure 6.3 it can be seen that the number of photoelectrons should be almost 600 so the estimation is not very good. A possible explanation is the fact that for this high peak intensity a shot directly at the ground station is required and the chance for that is very low. Also the Poisson statistics used for the photoelectrons produces a large uncertainty, especially in the higher photon regimes. However the estimation of the width w which is essentially the divergence angle of GALA is very accurate with a mean of exactly 10.32 arcsec and only a standard deviation of 0.02 arcsec. This result is in line with the accurate determination of the ground station position since the width is important for locating the top of the Gaussian curve, where the ground station is located.

For pulses these numbers are meaningless but here it is interesting to see how many pulses are detected as this should also converge to a stable mean. This is again the case and the number of detected photons is 1134 and 1098 for a sweep and vortex scan pattern respectively. The standard deviation is here 45 and 54 which is less than 5% of the total. With a detection threshold set at 10, the pulses are detectable up to 15 arcsec

Table 6.2: Verification results.

Scanning Pattern Photons / Pulses	Sweep Photons	Vortex Photons	Sweep Pulses	Vortex Pulses
Average error X [arcsec]	0.035	0.055	0.11	0.079
Average error Y [arcsec]	0.014	0.057	0.067	0.079
Mean error X [arcsec]	0.034	0.001	0.091	0.001
Mean error Y [arcsec]	9.85e-5	0.002	0.0052	0.001
Standard deviation X [arcsec]	0.024	0.071	0.096	0.099
Standard deviation Y [arcsec]	0.018	0.073	0.083	0.100
Mean I_0 [photoelectrons]	494	433	-	-
Standard deviation I_0 [photoelectrons]	72	77	-	-
Mean w [arcsec]	10.32	10.32	-	-
Standard deviation w [arcsec]	0.022	0.027	-	-
Mean number of detected pulses	-	-	1134	1098
Standard deviation detected pulses	-	-	45	54

away from the ground station, meaning that with a pass directly over the ground station around 40 pulses are detectable. Given the spacing of the shots, around 1150 shots should be detectable and this is indeed close to 1134 shots for the sweep pattern. Since the vortex pattern is not so nicely spaced it is an expected result that the number of detected pulses is a bit lower for the vortex pattern and that the standard deviation is a bit larger as it depends more on where the ground station is located in the pattern.

When processing the results from the runs, some outliers were detected where the algorithm was not able to produce a good result due to failure of the fit. These outliers were filtered out since it is very clear with these high precisions when an estimate is not good. The number of outliers were found to be 2-14 out of 1000 runs, which is considered a very low number. With the convergence of all discussed values, their high precision, and the robustness of the estimation it is verified that this estimation procedure is reliable and can be used further in this study.

6.4. Validation

The aim of the model developed in this chapter is to predict how the laser ranging experiment would perform for the real case. Since the model development is until now purely based on a theoretical discussion a more practical discussion is required to validate the model. For this the MLA experiment and the Hayabusa 2 experiment will be used in this section to make an thorough assessment. The goal is to see how well the model predicts the findings reported by the teams during the experiment. These two experiments are selected since they are the only examples available of a similar calibration as envisioned for GALA. The laser altimeters themselves were already introduced in Section 4.1.3 and here the discussion focusses on the experiments performed.

6.4.1. Validation with MLA experiment

The successful two way laser link established by MLA carried by MESSENGER and the GGAO in 2005 is the only other experiment performed in the same fashion as envisioned for GALA and therefore worth investigating in order to validate the simulation model. Several opportunities were available between May 24 and 31 2005 of which the attempt on May the 27th was most successful and will be the case simulated here.

That day the laser ranging started at 17:11 PM and lasted around 5 hours and 40 minutes (Coyle et al., 2006) scanning a window of 3.2 by 3.2 millirad or 660 by 600 arcsec (Smith et al., 2005, 2006) using a sweep scan pattern consisting of 100 lines each 32 microrad apart and a slew rate of 16 microrad/sec. These values were used as input to generate the sweep scanning pattern and it is well within the capabilities of the simulation to generate this scanning pattern.

Furthermore the used values are summarised in Table 6.3 that are used for the calculations where the receiver efficiency, quantum efficiency and spectral bandwidth are the reference values used throughout this study as no information was available on this. MLA position was generated using the SPICE database

available for the MESSENGER trajectory (Navigation and Ancillary Information Facility (NAIF), 2012). The reported maximum elevation and time indeed coincide with the found elevation using SPICE on the 27th on May and it is thus verified that the trajectory is the same.

Table 6.3: Summary of values used for the MLA laser link experiment.

Property	Value	Source
Pulse Energy	0.018 J	(Smith et al., 2005)
Beam divergence angle (half cone)	40 μrad	(Smith et al., 2005)
Pulse width (1-sigma)	2.5 ns	(Smith et al., 2005)
Shot frequency	8 Hz	(Smith et al., 2005)
Aperture diameter	1.2 m	(Smith et al., 2005)
Field of View (half cone)	130 arcsec	(Noda et al., 2017)
Receiver efficiency	0.5	
Quantum efficiency	0.2	
Spectral bandwidth	2 nm	
Mean range	24e9 m	(Smith et al., 2006)

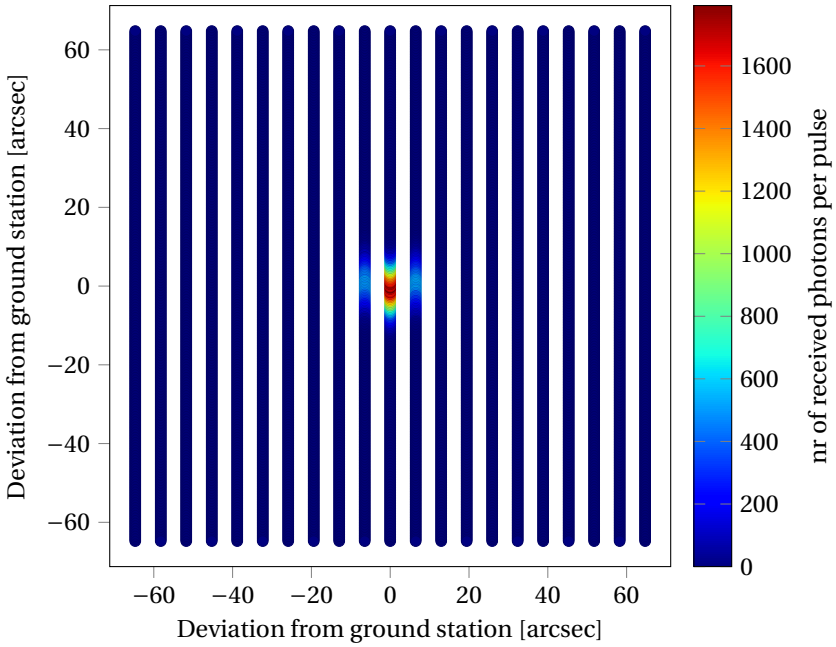

Figure 6.11: Sweep scan of the GGAO laser ground station from MLA for a distance of around 24 million kilometres.

Using this scan strategy, the laser pulses from MLA should be visible only during 3 sweeps for only a few seconds (Smith et al., 2005) which is confirmed in Figure 6.11 which shows the result of the simulation. Since this is exactly as expected, the simulation is validated for its scan pattern and shot generation. Also the link budget confirms that the signal is only visible for these three sweeps and only for some seconds. The results also show that at the peak, more than 1600 photons per pulse are available while most are in the 200-800 photons per pulse range. This allows for a high threshold setting since this laser ranging is also done during daytime, thus receiving noise from the Sun. However no information about threshold settings or the detector APD used are available. What is available is a description of the local weather and some pictures from the sky where many thicker clouds can be seen (Coyle et al., 2006). These clouds pose two problems starting with the fact that they block incoming laser pulses from MLA when they are crossing in the line of sight increasing the chance of no detection. Furthermore, the ground station laser was continuously firing laser shots at MLA during the experiment at a high frequency of 240 Hz. The clouds reflect part of these pulses creating echo's at

the receiver (Coyle et al., 2006). In the presence of so many clouds and such a high frequency, the incoming signal was almost continuously polluted with echoes while the MLA laser pulses are shot only with 8 Hz.

This signal was later analysed and 16 to 24 MLA pulses were identified (Smith et al., 2005). Figure 6.11 shows the detected shots, using a threshold of 50 photons which filters out most of the noise. Also a reduced detection probability of 33% was used to incorporate the effect of the clouds.

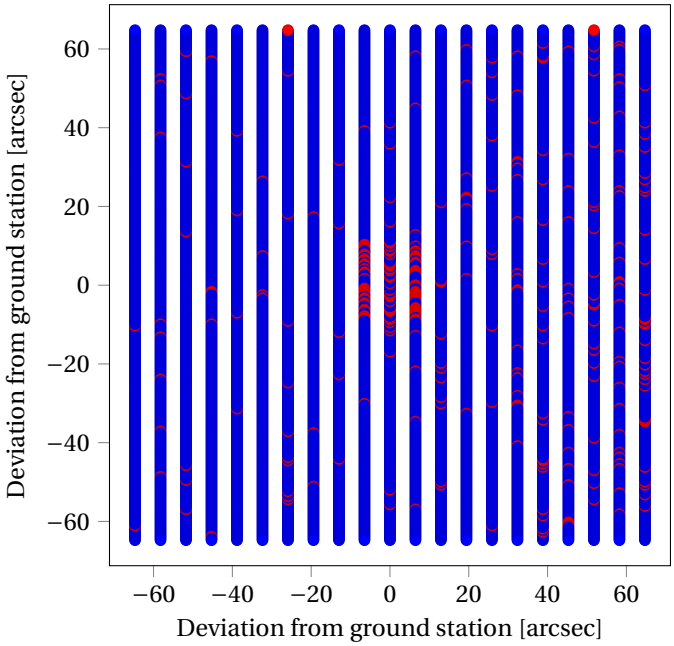

Figure 6.12: Detected pulses including both false detections as well as pulse detections. The location of the ground station is still clearly visible in the middle for three sweeps.

Here the three sweeps of the ground station that should be visible are clear and a total of around 60 shots should be detectable. From the information available, the detected shots all originate from the same pass and thus with 60 shots over three passes, around 20 shots should be detected per pass, close to the detected shots in the real experiment.

These findings indicate that weather conditions play an important and unpredictable role in laser ranging, especially with a low frequency and low number of detectable passes over the ground station. If no reduced detection probability was added to the simulation, around 150 shots should be detectable. That is, if they are all distinguishable from the noisy signal including echoes. This indicates another difficulty for laser ranging that is for now not including in the simulation.

6.4.2. Validation with Hayabusa 2 experiment

The Hayabusa 2 spacecraft carries a LIDAR which was also used to conduct a laser link experiment (Noda et al., 2017). After an Earth flyby on the 3th of December 2015, several opportunities were available for laser ranging using the Mt. Stromlo laser ranging station in Canberra, Australia. Since this is the only other laser ranging experiment conducted in more or less the same fashion as envisioned for GALA, it is worth investigating this case and validate the model developed for this study.

The LIDAR laser ranging experiment was conducted on December 11 and 15 in 2015 at a distance of around 6.6 million kilometres which is a very small distance compared to distances envisioned for GALA. However the properties of the laser transmitter as given in Table 6.4 show a large difference compared to GALA in the fact that the beam divergence angle is 1.25 millirad or 257 arcsec, much larger than GALA at 10.3 arcsec, resulting in a much lower signal strength than one would expect for GALA at this distance.

The operations are different from GALA since not a sweep or vortex scan pattern was used, but instead the scan windows was divided up into smaller blocks. The spacecraft would be aimed to each block for a certain amount of time, before switching to the next block. 4 days were available to scan a window 1 by 1 degrees and 2 hours of scanning were available per day, totalling up to a scan duration of 8 hours, not far from GALA operations. However only 92 scans per hour with 17 detections could take place, summing up to

1564 detections per hour or 12512 for the total duration, almost 1 shot per 2 seconds on average. Using this information it was decided to simulate one 2 hour scan using a frequency of 0.43 Hz and a scan window of 0.5 by 0.5 degrees or 1800 by 1800 arcsec, mimicking a one day scan. A sweep scan pattern was selected to get an idea and the scan speed was set such that the shots are evenly spaced in the scan window. These scans were conducted at night, so no solar noise is present (Noda et al., 2017).

Table 6.4: Summary of values used for the Hayabusa 2 LIDAR laser link experiment.

Property	Value	Source
Pulse Energy	0.015 J	(Noda et al., 2017)
Transmitter efficiency	0.8	(Noda et al., 2017)
Beam divergence angle (half cone)	1.25 mrad	(Noda et al., 2017)
Pulse width (1-sigma)	2.9 ns	(Noda et al., 2017)
Shot frequency	0.43 Hz	
Aperture diameter	1.8 m	(Noda et al., 2017)
Field of View (half cone)	10 arcsec	(Noda et al., 2017)
Receiver efficiency	0.8	(Noda et al., 2017)
Quantum efficiency	0.2	(Noda et al., 2017)
Spectral bandwidth	2 nm	(IRLS, 2017)
Total loss	0.1 - 0.5	(Noda et al., 2013, 2017)
Mean range	6.6e9 m	(Noda et al., 2017)

Other values used for the simulation are summarised in Table 6.4 including the laser energy and its efficiency and the ground station properties. Note the total loss factor of 0.1 (Noda et al., 2017) or 0.5 (Noda et al., 2013) that is added for the link budget calculations. It is not stated why these loss factors are included and why they differ from paper to paper but their influence is clear, the total link budget is decreased by a factor 2 or 10. A receiver efficiency of 0.8 is considered very high for a ground station so an extra loss factor of 0.5 is not questionable. One could also include here the degradation of the laser, since (Noda et al., 2013) mentions an energy of 10 mJ only. The position of Hayabusa 2 was generated using SPICE databases generated to study this mission (Japan Aerospace Exploration Agency (JAXA), 2017)

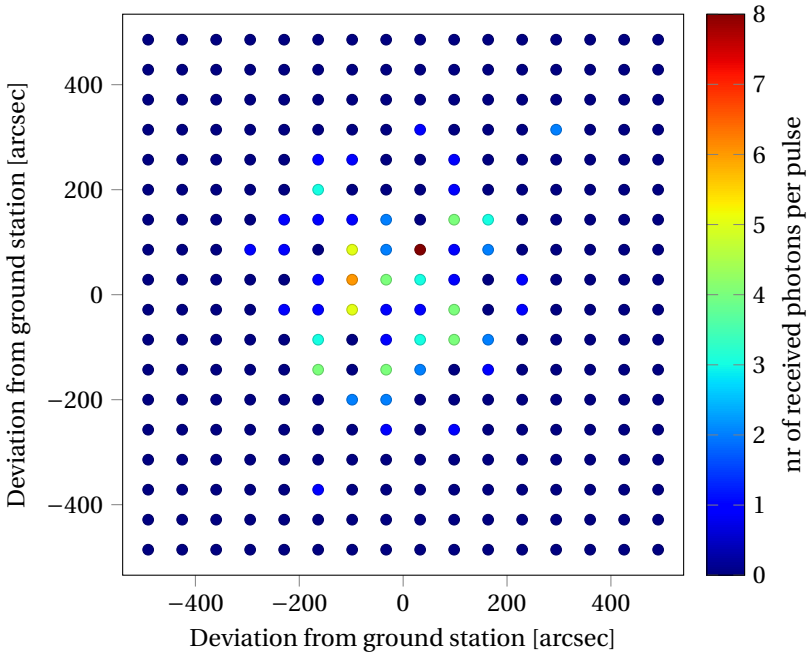

Figure 6.13: Sweep scan of the Mt. Stromlo ground station by the Hayabusa 2 LIDAR.

Figure 6.13 shows the scatter plot of the sweep scan over the ground station with its signal strengths. A

maximum of 5 photons is available for detection but only for a few shots, roughly the same order of magnitude as predicted by (Noda et al., 2013) and (Noda et al., 2017) where a number of 10.8 photoelectrons was found. However here a different way of determining the link budget as there a constant signal intensity over the footprint is assumed. However the difference might just explain why no signal was detected at all during the experiment. Most shots show a strength of 1-3 photons which is in the regime of the dark noise produced by the silicon APD used (Noda et al., 2017). Therefore detection of these shots will highly depend on the noise levels of the APD as also already mentioned in (Noda et al., 2013). If it was not possible to reduce the noise levels to such low levels, no shots would be detectable at all.

Single photon detection was employed for detection of the laser shots and therefore it is difficult to compare this simulation with the actual experiment. When the standard settings are used in the simulation, a threshold of 3 photons is required to filter away most of the noise. Then Figure 6.14 shows the shots that could be detected, which are only 13 shots spread to different sweeps over the ground station such that maybe only 2-3 shots per sweep are detectable.

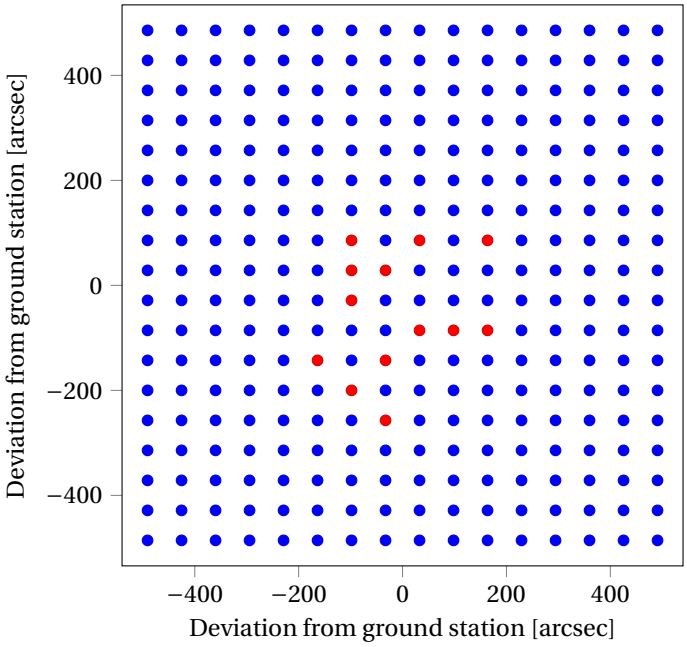

Figure 6.14: Detected shots for the Hayabusa scan indicating only 13 detectable shots.

Two main comments can be made about the laser ranging experiment of Hayabusa 2. With this low firing frequency and the high scan window to cover, only a low number of shots will be directed towards the ground station. Thus the main reason for such low number of detectable shots is the scan window and frequency. With such low number of shots over the ground station, everything must be perfect to actually detect them. In the presence of a cloud or other unknown and unpredictable events, the already small chance is gone and nothing will be detected at all. The other comment can be made about the low signal intensity due to the high divergence angle. (Noda et al., 2013) suggests that detection is possible up to 0.3 AU if a 1 photon threshold is used, using an APD in Geiger mode. However as explained in Section 3.2 a large number of shots is required to filter out the noise afterwards, not available with a shot frequency of 1 Hz for the LIDAR.

In the end no shots were detected by the ground station (Noda et al., 2017) and the foregoing discussion points out why this can be expected. The simulation can explain this with the simulated signal strengths and the shot distribution and thus it is validated that it can serve as a good indication for expected outcomes of a laser experiment. In the simulation however still some shots should be detectable using threshold detection and with sufficiently low noise. However issues such as clouds, attitude disturbance, misalignment, laser degradation and single photon detection were not taken into account and with this low amount of shots detectable, these could exactly be the reason why no shots were detected.

7

Trajectory analysis

JUICE will take a 7.5 year journey to Jupiter including flybys of Earth, Venus and Mars and serves as a fixed constraint for laser ranging and therefore laser ranging will be incorporated into the trajectory. However detailed data is available on the trajectory as all institutes cooperating in the mission are preparing their designs and mission operations based on it. In order to determine realistic conditions for the laser ranging campaigns, the JUICE trajectory is analysed for possible opportunities for such a campaign. First an overview of the trajectory is given in Section 7.1 after which the constraints on opportunities are discussed in Section 7.2. Alongside with the constraints, also favourable conditions will be determined and this will lead to the selection of a number of options which will be presented in Section 7.3. Options for laser ranging can also be optimised in terms of elevation, duration and range and this is the final aim of this chapter, leading to the selection in Section 7.5. Here a number of options is finally selected that will serve as the options that are to be studied.

7.1. Overview

The JUICE mission will consist of a cruise phase where the spacecraft will use an interplanetary transfer trajectory to reach the orbit of Jupiter and insert itself into a Jupiter orbit. From here a Jupiter tour and a Ganymede tour will be at the heart of the mission (Dougherty, 2011; Grasset et al., 2013; European Space Agency (ESA), 2014). However in terms of duration, the heart of the mission lies at the cruise phase as it will take more than 7 years to reach Jupiter while the Jupiter and Ganymede tours will last 2 and 1 years respectively.

It is the cruise phase that is of interest for this analysis since here various conditions and, most prominently, distances are present. The cruise phase is depicted in Figure 7.1. It consists of the launch in 2022 followed by Earth-Venus-Earth-Mars-Earth flybys. After the last Earth flyby, the spacecraft will head for Jupiter and is inserted in Jupiter orbit. Afterwards the distance will remain between 4 to 6 AU. Since the distance is a major parameter for laser ranging, the interesting part for this analysis is up until the arrival at Jupiter.

The distances to the various planets are presented in Figure 7.2 and are derived from the JUICE CReMA 3.0 Spacecraft Planet Instrument Camera matrix Events (SPICE) kernels based on the mission scenario 'mantra_juice_jup_a5d_141a_lau_c5e_016.oem' (Boutonnet and Varga, 2016). During the entire thesis work, this version of the kernels, as released by ESA is used. Here the various flybys can be clearly seen when the distance diminishes to almost zero AU. JUICE will be launched by an Ariane 5 ECA rocket and a direct escape will follow, leaving little time for calibration of the instruments while JUICE is in Earth orbit (Dougherty, 2011).

7.2. Constraints and considerations

JUICE will not be able to perform laser ranging activities throughout the entire mission. Several constraints and limitations are in effect as JUICE also carries 10 other experiments and instruments that also want to perform measurements and will need downlink bandwidth. Thus only limited time and resources will be available for each instrument and therefore optimal opportunities should be selected. Optimal opportunities are optimal in terms of detectable pulses. This means that a higher link budget is more favourable and a longer scanning duration is favourable and these should be optimised. Furthermore the spacecraft design

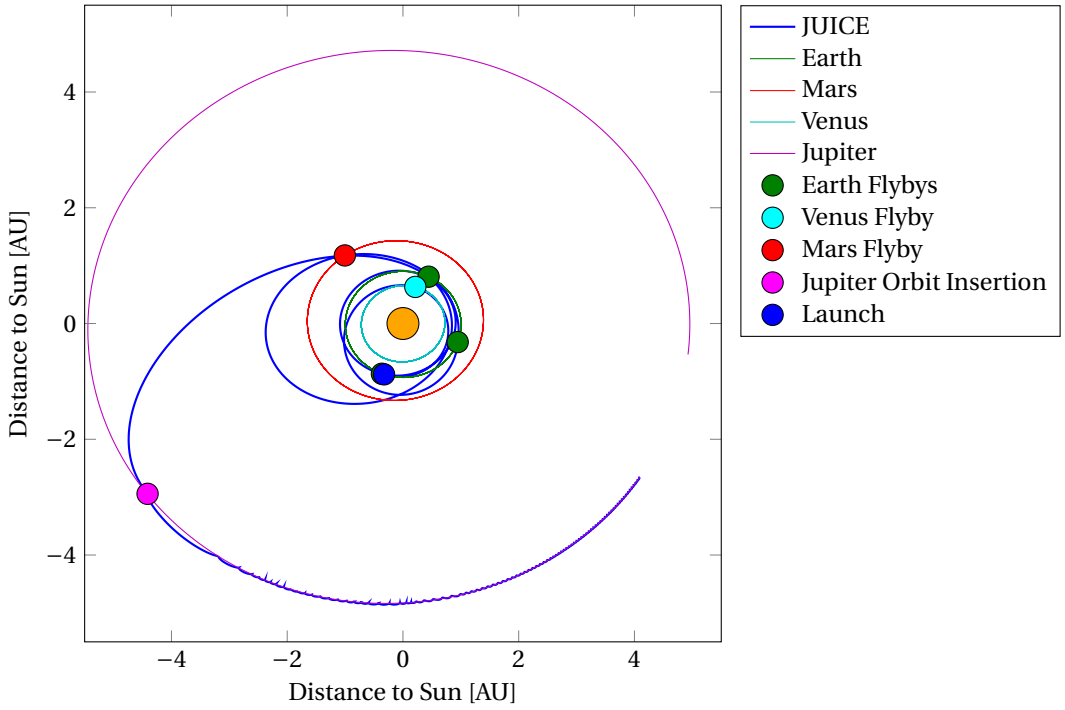

Figure 7.1: Overview of the JUICE trajectory.

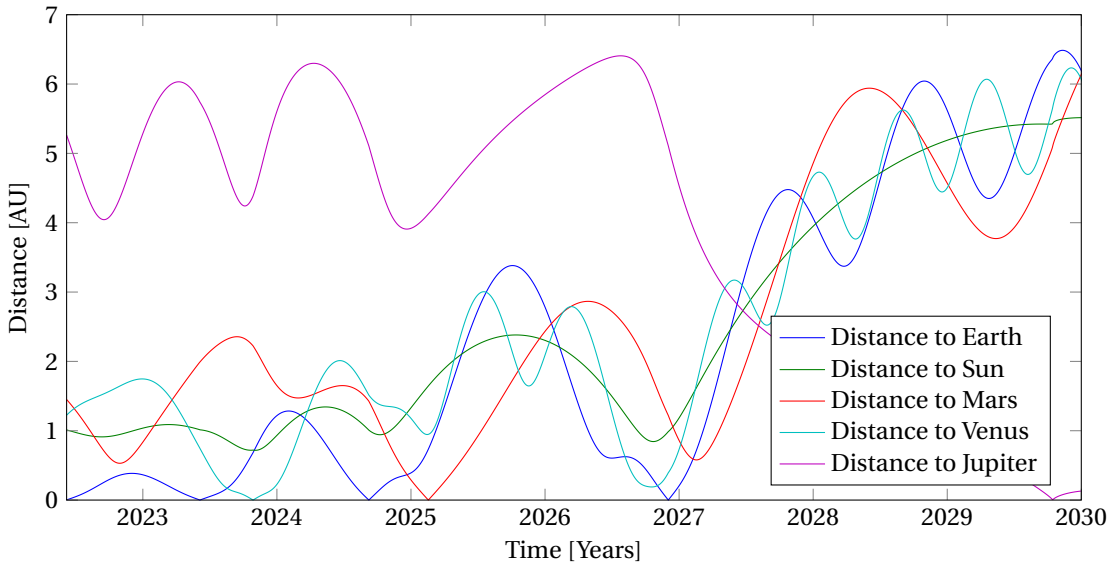

Figure 7.2: Distances during the JUICE interplanetary cruise phase.

and the considerations by ESA will put constraints on laser ranging that have to be accounted for in this analysis. Thus two aspects are treated here; hard constraints and limitations in due to angular separation requirements and High Gain Antenna (HGA) sun pointing and considerations that will optimise the link budget and the scanning duration.

7.2.1. Angular separation between Sun and Instrument Line of Sight

In order to detect the signal of the laser, the noise should be at a sufficient low level to allow for detection. As the Sun produces many photons, the telescopes of GALA and the ground station should not look directly in the Sun and even have a minimum angular separation between the Sun and their Instrument Line of Sight

(ILS) in order to reduce the stray light from the Sun. The detector telescope of GALA will feature a baffle which will be designed to reduce stray light and will reject stray light when the angular separation is larger then 20 degrees. With smaller angles some stray light will reach the detector, this increases with smaller angles up to a point where the detector will heat up to much due to Sun light. Therefore the limit is set at an angular separation of 2 degrees and the favourable condition is an angle of 20 degrees or more between the Earth and the Sun as seen from JUICE.

7.2.2. High Gain Antenna Sun Pointing

Another implication of the spacecraft design is that the HGA acts as a sunshield to make sure JUICE does not overheat during part of the cruise. The HGA should be pointing at the Sun whenever the distance of JUICE to the Sun is lower than 1.3 AU. This puts severe constraints on the number of opportunities as no laser ranging can be performed near Earth. However JUICE is allowed to deviate from HGA Sun pointing for the limited time of 1 hour. This provides at least some options for laser ranging near Earth. Another opportunity lies where the angle between Earth and Sun as seen from JUICE is exactly 90 degrees with a margin of a few degrees. In this case the HGA can keep pointing at the Sun while GALA points at Earth.

7.2.3. Link budget

As shown in Equation 3.18, the link budget is largely governed by the distance between the transmitter and detector. Thus the lower the distance, the higher the link budget. Therefore an opportunity is more favourable when the distance is smaller. This will serve as an input for the analysis, selecting opportunities with lower distances where other conditions may be less favourable. The smaller distance will then compensate for this since the link budget is better. This is for example the case for opportunities near Earth flybys. Although the duration is limited to 1 hour only due to thermal constrains, the much lower distance will result in more detectable pulses, compensating for the shorter duration.

Another factor for the link budget is the elevation of JUICE. The lower the elevation, the smaller the link budget as shown in Equation 3.11. Therefore this will be taken into account when analysing the trajectory.

7.2.4. Ground station conditions

Since part of the noise at the ground station is caused by atmospheric scattering of Sun light, it is favourable to operate the ground station during darkness. This condition can be translated to an angular separation between the Sun and JUICE as seen from Earth of more than 90 degrees to make sure this is the case. Another possibility is to make sure the elevation of the Sun at the ground station is lower than zero degrees, this is however dependent on its position on the Earth surface and thus will vary per ground station.

Ground stations have a limit on the minimum elevation of the target and this is commonly set at 20 degrees elevation. Thus JUICE should be visible by the ground station at an elevation of 20 degrees or higher. This is related to the latitude of JUICE with respect to the Earth reference frame. At some intervals in the trajectory, a ground station on the southern hemisphere will be preferable, other times one in the northern hemisphere is preferable.

Finally the weather at the ground station will determine if laser ranging is possible at all. In case of clouds, laser ranging is not possible and the opportunity is missed. This is mitigated by selecting only opportunities that can last for multiple days or can be mitigated by using multiple ground stations with different locations on Earth. So the ground station must be able to target JUICE for multiple days after each other. The minimum days for the laser ranging campaign is set at 7 days.

7.3. Requirements Analysis

The constraints and requirements are strict and will eliminate certain parts of the trajectory of laser ranging options. Therefore first an analysis of these will be made leading to certain options. Here no optimisation is possible or favourable and thus only eliminating options is considered.

7.3.1. Angular separations

The angular separations between Earth and Sun as seen from JUICE and between Sun and JUICE as seen from Earth should both be at least 20 degrees European Space Agency (ESA) (2017); Schreiber (2017). The angular separation between Earth and Sun is presented in Figure 7.3a and becomes smaller as JUICE is further away from Earth, as one would expect. The red dots show when the separation satisfies a minimum of 20 degrees, identifying where laser ranging would be optimal in terms of noise reduction. The angular separation

between JUICE and the Sun as seen from Earth is not a limiting constraint as shown in Figure 7.3b. Only in the case when JUICE passes the Sun in front or behind it poses a problem. Otherwise the angular separation is always many times larger than the Field of View (FOV) of any telescope on Earth for these purposes. In Figure 7.3b the blue dots represent optimal cases for this constraint and for better overview also the optimal opportunities for the separation between Sun and Earth is plotted again. It can be clearly seen that this is the limiting case for laser ranging.

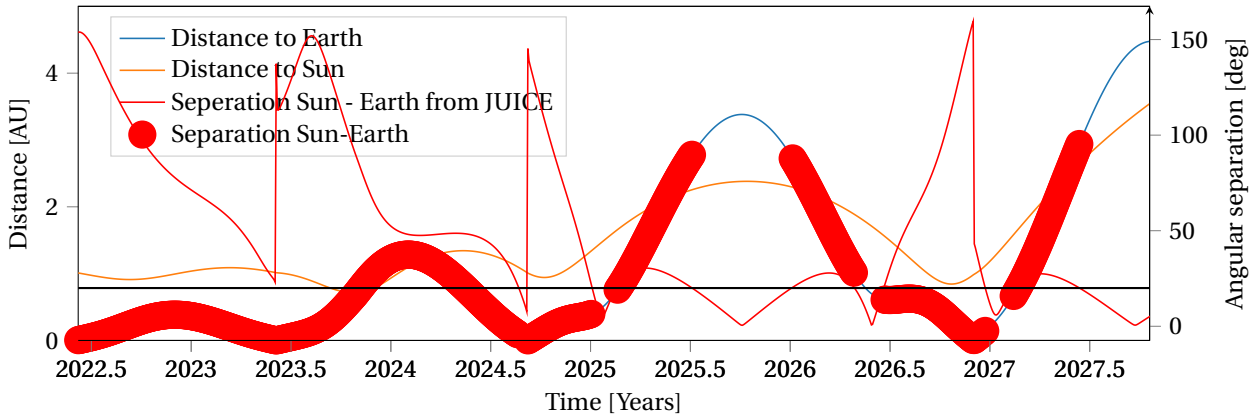

(a) Angular separation Sun and Earth as seen from JUICE.

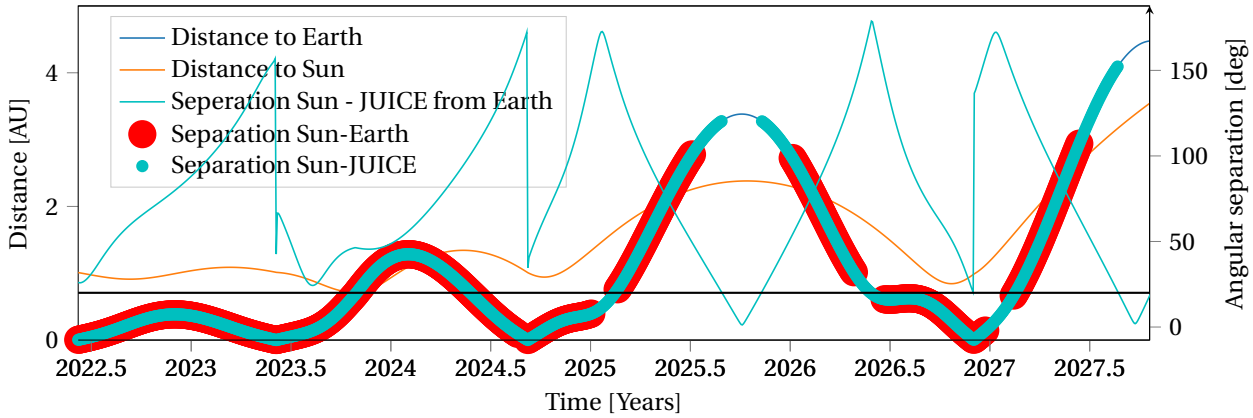

(b) Angular separation Sun and JUICE as seen from Earth.

Figure 7.3: Angular separations for the JUICE trajectory up to 4.5 AU. The black line shows the 20 degrees constrain and the coloured markers show where in the trajectory this is satisfied. Figure 7.3a indicates the separation angle between Sun and Earth as seen from JUICE on the right axis, while 7.3b shows the separation of angle between the Sun and JUICE as seen from Earth on the right axis. In 7.3b also both constrains are plotted by the markers on top of each other for comparison.

7.3.2. Sun pointing of the High Gain Antenna

The required Sun pointing of the HGA has two consequences, a limited duration of one hour and laser ranging beyond 1.3 AU distance from the Sun. However, during the trajectory certain geometry allows the HGA to be Sun pointing while GALA can point to Earth. Here the angle between the Sun and Earth as seen from JUICE is 90 degrees and thus laser ranging can be performed while the HGA is pointing at the Sun. An angle of exactly 90 degrees will never happen in nature and is therefore not a realistic requirement but instead an offset is allowed of 3 degrees from the 90 degrees which is deemed reasonable by ESA. What the maximum offset can be is currently under investigation by the mission team but a few degrees is considered not a problem. Increasing the allowed offset will increase the number of days that laser ranging is possible, providing more back up days in case of bad weather or other issues.

As Figure 7.4 illustrates, four possible options exist for the case where the HGA remains Sun pointing. Also indicated are the three periods where JUICE is far away enough from the Sun for laser ranging without the Sun pointing constraint. The closest opportunities are at the end of the first period, the beginning and end

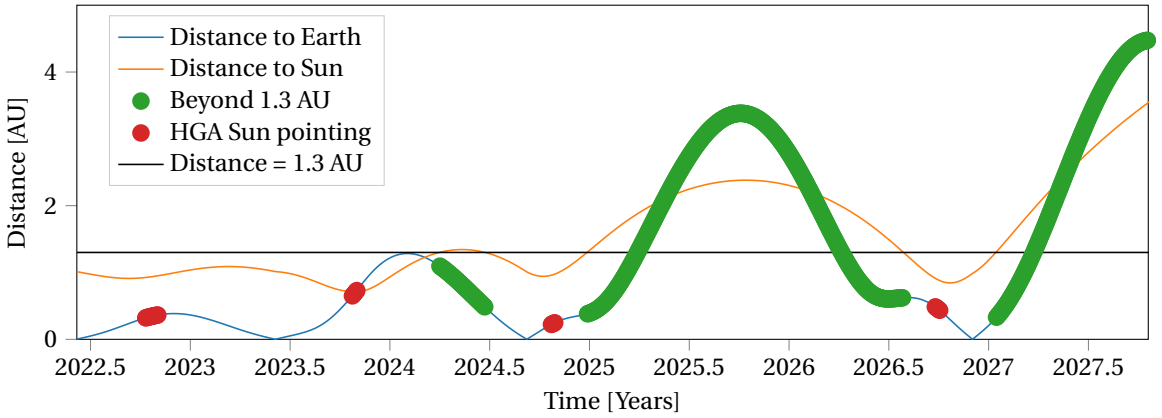

Figure 7.4: The trajectory of JUICE showing at which distance the constrains set by the HGA are met. Green markers indicate where the distance of JUICE to the Sun is more than 1.3 AU, represented by the black line. The red markers indicate a 90 degree angle between Sun and Earth as seen from JUICE. Here the HGA can maintain Sun pointing during laser ranging.

of the second, and the beginning of the third period. The closest opportunity is the one at the beginning of the third period, in the beginning of 2027 and the distance is here around 0,33 AU. All these four options are considered as opportunities since this minimises the distance. Of course laser ranging can be done further away if this is required as long as the link budget allows. The four HGA Sun pointing opportunities range in distance from 0,22 AU to 0,74 AU and take place throughout the trajectory. The options further away than the closest option beyond 1.3 AU show no advantage with respect to distance. However, the opportunity at 0,22 AU does and this is the closest option available for laser ranging with a duration longer than 1 hour.

7.3.3. Total overview

The most promising option in terms of link budget is laser ranging as close to Earth as possible. This is possible just before and after an Earth flyby. When the closest options that have a Sun distance of at least 1.3 AU are included and at least laser ranging for 10 days is set as an requirement, three cases can be distinguished. The first is where JUICE has a distance with respect to the Sun larger than 1.3 AU. The second is when the HGA can maintain Sun pointing and the third one is just before and after Earth flyby where laser ranging is only possible for one hour.

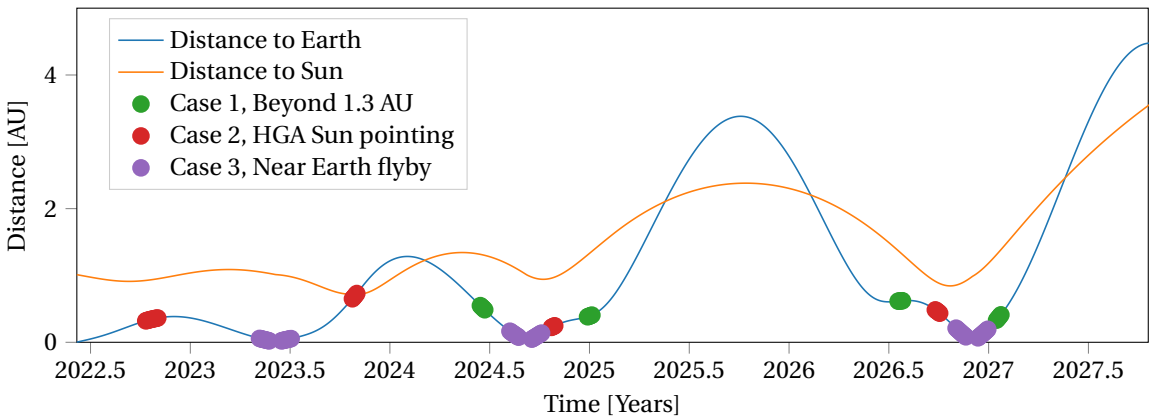

Figure 7.5: Overview of the distances to Earth of the three presented cases indicated by the markers on the trajectory of JUICE.

Figure 7.5 shows the overview of the different options available. Four options beyond 1.3 AU are selected, corresponding to the smallest distance to Earth for this case. The options before or after Earth flyby correspond to 10 to 20 days after and before Earth flyby.

7.4. Ground Station Analysis

Table 7.1 shows an overview of interesting ground stations. Mt. Stromlo and Goddard originate from the validation of MLA and Hayabusa 2 in Section 6.4 and are interesting since one is in the southern and one in the northern hemisphere and both have the capability to do laser ranging at 1064 nm wavelength. Wettzell is interesting since close cooperation with the GALA team exists and Grasse, although not very different in location, is interesting since it features a larger telescope. This also is why the Apache Point Observatory Lunar Laser-ranging Operation (APOLLO) ground station is included here as it may allow for laser ranging at greater distances.

Table 7.1: Overview of the ground stations and their reported properties by IRLS (Tyahla and Noll, 2016).

Parameter	Wettzell	Grasse	APOLLO	Mt. Stromlo	Goddard
Code	WETL	GRSM	APOL	STL3	GGAO
Latitude [deg]	49.1444	43.7546	32.780361	-35.3161	39.0206
Longitude [deg]	12.8780	6.9216	-105.820417	149.0099	-76.82770
Telescope diameter [m]	0.75	1.54	3.5	1	1.2
Optical efficiency [-]	0.5	0.22	0.4	0.35	
Spectral bandwidth [nm]	12	0.12	-	2	
Receiver FOV [arcsec]	9	7-20	1.4	12	130
Quantum efficiency [-]	0.5	0.2	0.3	0.2	
Laser energy [mJ]	200	300	115	2200	15
Optical efficiency [-]	0.5	0.45	0.6	0.75	
Beam divergence(half) [arcsec]	0.5-100	0.5-5	0.5	7	40

7.4.1. JUICE Latitude

Since different ground stations are available at different latitudes, it is interesting to analyse the latitude of JUICE as seen from Earth shown by Figure 7.6. It can be seen that especially right after each Earth flyby, JUICE has a positive latitude, more ideal for ground stations in the northern hemisphere such as Wettzell and Grasse. These Earth flybys are clearly visible as they case a sudden jump in the latitude and indeed here the distance to Earth is almost zero in Figure 7.6. However for some parts JUICE is on the southern hemisphere and the visibility will be low from these ground stations. Therefore it is beneficial to include also a ground station located on the southern hemisphere.

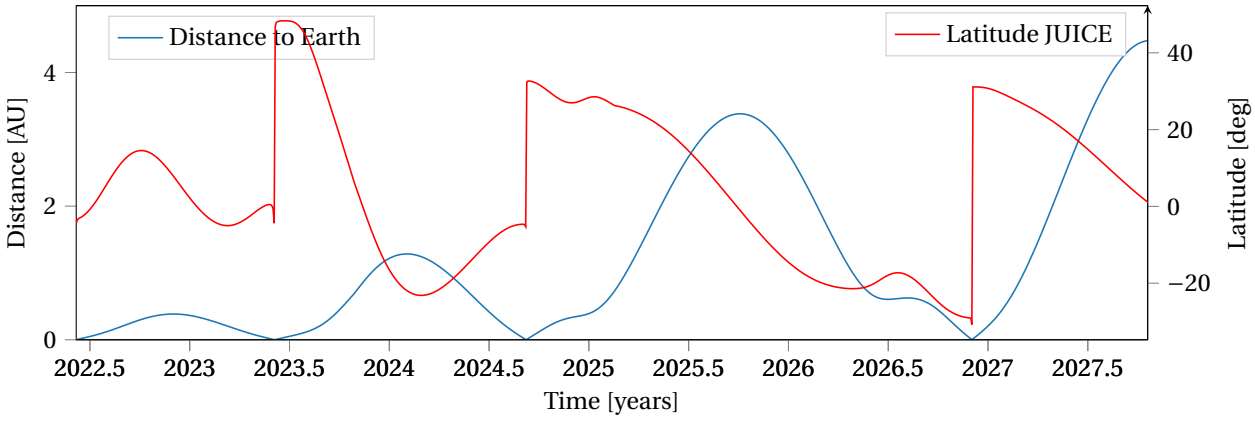

Figure 7.6: Latitude of JUICE during the trajectory towards Jupiter.

Generally speaking, a latitude between -20 and +20 degrees is most favourable throughout the trajectory. Unfortunately, in this region almost no ground stations are available. Other stations in Table 7.1 do not vary much in latitude with only a maximum difference of 10 degrees. Therefore two ground stations will be used to analyse the entire trajectory, Wettzell and Mt. Stromlo. Most of the time Hartebeesthoek will have JUICE at

a bit higher elevation and thus the duration can be increased a bit and the elevation is a bit more favourable. This is generally also the case for Grasse, Apollo and Goddard compared to Wettzell unless the latitude of JUICE gets close to that of Wettzell or Mt. Stromlo. Therefore they serve as a good worst case scenario, for example switching to Grasse will give a larger telescope and a bit higher elevation. Later when cases are discussed using Grasse, the Grasse conditions will be given when required.

7.4.2. Visibility Duration

Another consideration for successful laser ranging is the possible duration. Increased duration results in more shots fired and for the same scan window a smaller spacing between the shots is possible. Both will increase the number of detectable shots and the chance for successful laser ranging and therefore a longer duration is preferred. The maximum duration available is the time that JUICE is above an elevation of 20 degrees at the ground station presented in Figure 7.7 on the right axis where the duration is determined rounding to round hours, explaining the steps in the plot. The requirement of 20 degrees is set by local law since the lasers used should not harm any people accidentally. Using these two ground stations, almost the entire trajectory is available for laser ranging with a minimum of 4 hours as shown in Figure 7.7. Thus this does not pose a severe limitation on laser ranging and even durations up to 15 hours should be possible. However this will also mean that in many occasions also the Sun will rise and cause atmospheric noise in the detector, making detection more difficult.

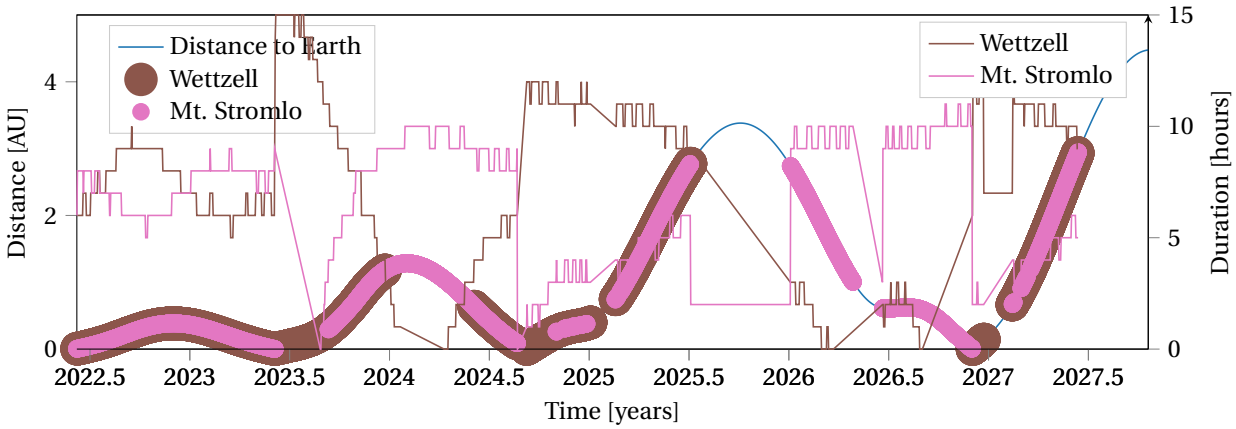

Figure 7.7: The maximum durations of visibility available for laser ranging for the ground stations Wettzell and Mt. Stromlo. Durations are rounded to full hours and here the markers indicate when at least four hours of laser ranging are available for the ground station indicated by the marker.

7.4.3. Elevation JUICE

However not only the length of an option is favourable for laser ranging, also the elevation of JUICE during scanning will determine the link budget and here a higher elevation is favourable for laser ranging due to the atmospheric transmission as given in Equation 3.11. Figure 7.8 shows the mean elevations when JUICE has a minimum elevation of 20 degrees and is thus visible for the two ground stations under consideration. Here a large difference is found between the ground stations due to their different latitudes and the trajectory of JUICE. Given the range of options it is safe to say that a mean elevation of above 40 degrees can be achieved for laser ranging. The maximum mean elevation is at 60 degrees which corresponds to a very high maximum elevation close to 90 degrees. This is especially the case in the second half of 2023 where the latitude of JUICE corresponds almost with the latitude of Wettzell as depicted already in Figure 7.6. Thus a significant optimisation is possible by selecting an appropriate ground station, given the latitude of JUICE.

7.4.4. Nighttime Ranging

Since solar noise is only present during daytime, it is favourable to analyse the trajectory to find opportunities to use night time laser ranging conditions at the ground station. For this the elevation of the Sun should be below zero at the ground station and JUICE should be visible above an elevation of 20 degrees. Also included are the minimum angular separations as discussed before. Note that as soon as JUICE is on a trajectory

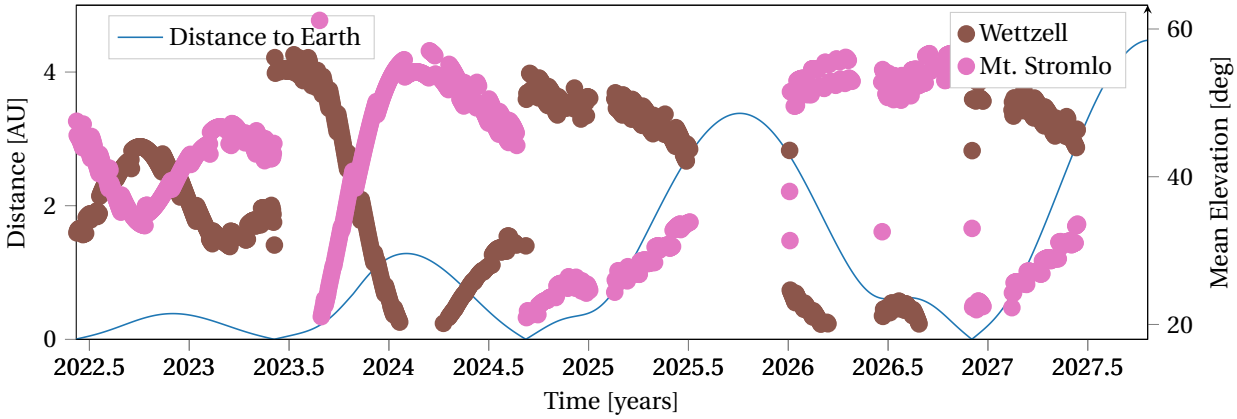

Figure 7.8: Mean elevations of JUICE with a minimum elevation of 20 degrees indicated with the markers where each colour represents the Wettzell and Mt. Stromlo ground stations. Only options where JUICE achieves an elevation of more that 20 degrees for at least four hours are indicated.

further away from the Sun and ahead or behind Earth orbit, it is possible to perform laser ranging. Therefore it is possible to perform night time laser ranging almost the entire trajectory for at least a short amount of time. However it only is profitable if laser ranging can be performed for more than 4 hours. Four hours is considered here since it delivers a reasonable calibration as will be discussed in Chapter 8. This is reflected in Figure 7.9 where the possible laser ranging options during the night for Mt. Stromlo and Wettzell are presented. Plenty of options for laser ranging beyond a Sun distance of 1.3 AU exist, especially in 2027 for both stations and also near Earth options are be available. Otherwise night time ranging is somewhat limited throughout the trajectory.

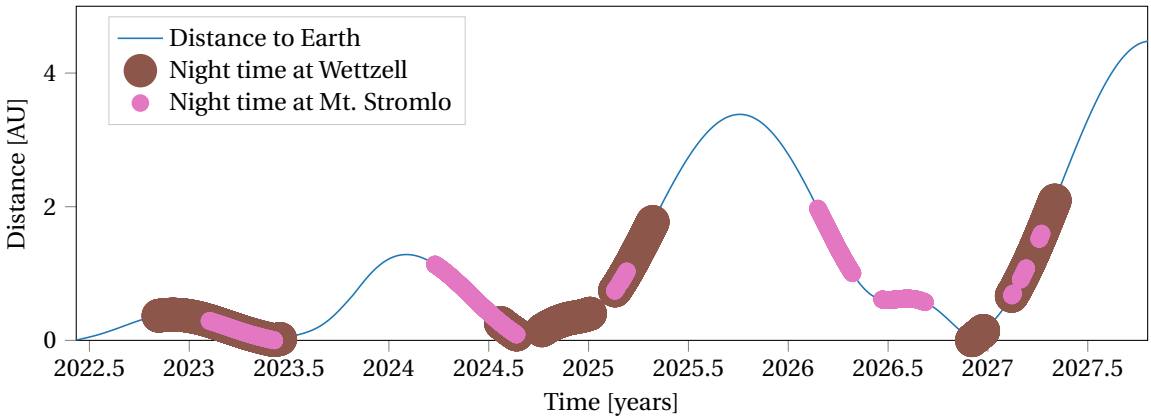

Figure 7.9: Laser ranging options indicated by the markers during night time for more than 4 hours for both ground stations.

7.5. Results

After discussing and analysing the requirements and considerations separately, the final options will be a combination of all of them. Each case presented in Section 7.3 is discussed separately and for all options given in this section a number of requirements is met; the minimum separations angles of 20 deg as mentioned in Subsection 7.3.1 and a minimum elevation of JUICE of at least 20 deg for at least 4 hours as discussed in Subsection 7.4.2. A next step is performed by optimising for duration, distance, elevation and night time ranging using the considerations from Section 7.4. This will finally yield the most optimal laser ranging options on the trajectory of JUICE.

7.5.1. Case 1: Beyond 1.3 AU

Laser ranging when JUICE is beyond a distance from the Sun of 1.3 AU is possible as shown in Figure 7.10, where for convenience also the distance to the Sun is plotted. The first options are in 2024 just before the first Earth flyby. Then in the beginning of 2025 there is another option for Wettzell which is the closest option possible. Then throughout 2025 and the first half of 2026, many options are available which also holds for the start of 2027. Especially the start of 2027 is interesting as this will be the last opportunity for laser ranging before JUICE will reach Jupiter. Therefore any settling effects due to thermal or vibrational influences during the first 5 years in cruise will be also taken into account if GALA is calibrated at this point. Thus it will provide the most updated calibration before start of the science missions. If somewhere earlier also a successful calibration was performed, the scan window can be made smaller since some contributions will not be present any more and then it is possible to perform the scan with a very slow slew rate, producing much more points that are detectable and thus increasing the chance of detection and the accuracy of the alignment error estimation.

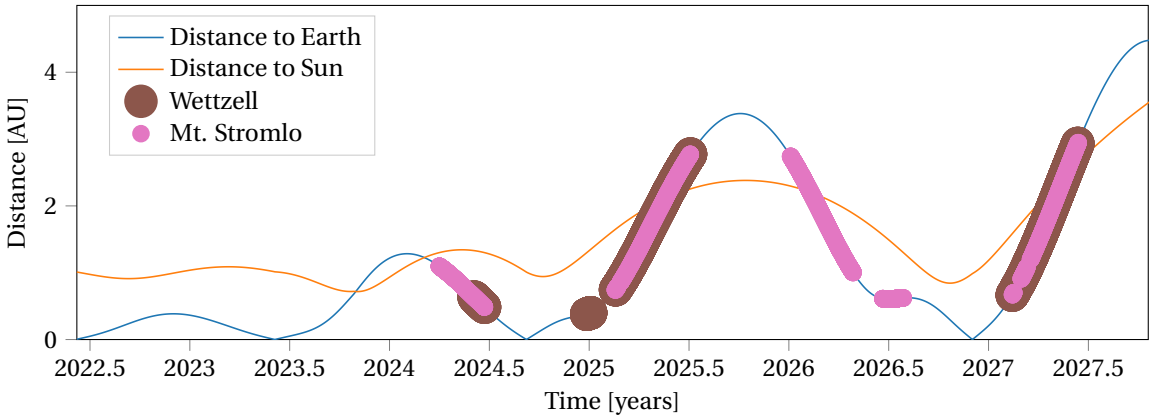

Figure 7.10: All options for laser ranging beyond a distance to the Sun of 1.3 AU. The markers indicate when the mentioned requirements are met for the two ground stations.

Optimum results can be considered when only night time ranging is allowed and the duration and mean elevation are maximised as shown in Figures 7.11a and 7.11b for both ground stations. The first good option is mid 2024 where 7 hours of laser ranging is possible to Mt. Stromlo. After this the closest option with high elevations and durations show up for Wettzell at the start of 2025. This is the most optimal option with its high durations and elevations and most prominently, the smallest distance to Earth. However only 7 days are available under this conditions and thus not many back up days are possible. Mt. Stromlo shows another option mid 2026 and the fourth option is in the first half of 2027 for Wettzell. The options are summarised in Table 7.2 where four opportunities are identified of which option 1.2 is the most optimal in terms of duration and distance.

Table 7.2: Overview of optimum options for laser ranging beyond 1.3 AU distance to the Sun during night time.

Nr	Ground Station	Start	End	Range [AU]	Mean Elevation [deg]	Duration [hours]
1	Mt. Stromlo	26/03/2024	17/06/2024	0.8	-	-
1.1	Mt. Stromlo	07/06/2024	17/06/2024	0.52	54	7
2	Wettzell	21/12/2024	28/12/2024	0.39	-	-
1.2	Wettzell	21/12/2024	28/12/2024	0.39	51	11
3	Mt. Stromlo	15/06/2026	22/07/2026	0.62	-	-
1.3	Mt. Stromlo	15/06/2026	25/06/2026	0.61	54	9
4	Wettzell	06/02/2027	26/04/2027	1.32	-	-
1.4	Wettzell	07/02/2027	17/02/2027	0.74	54	10

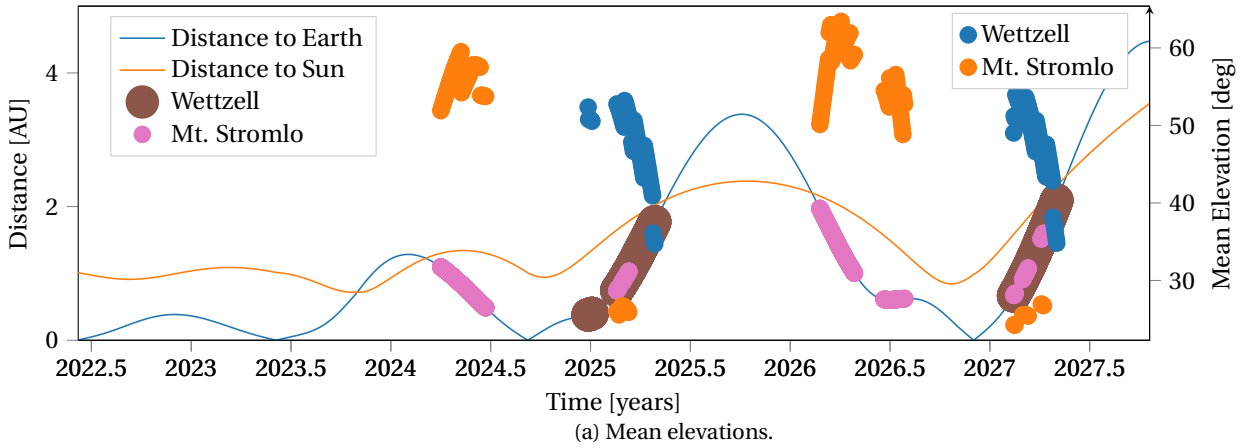

(a) Mean elevations.

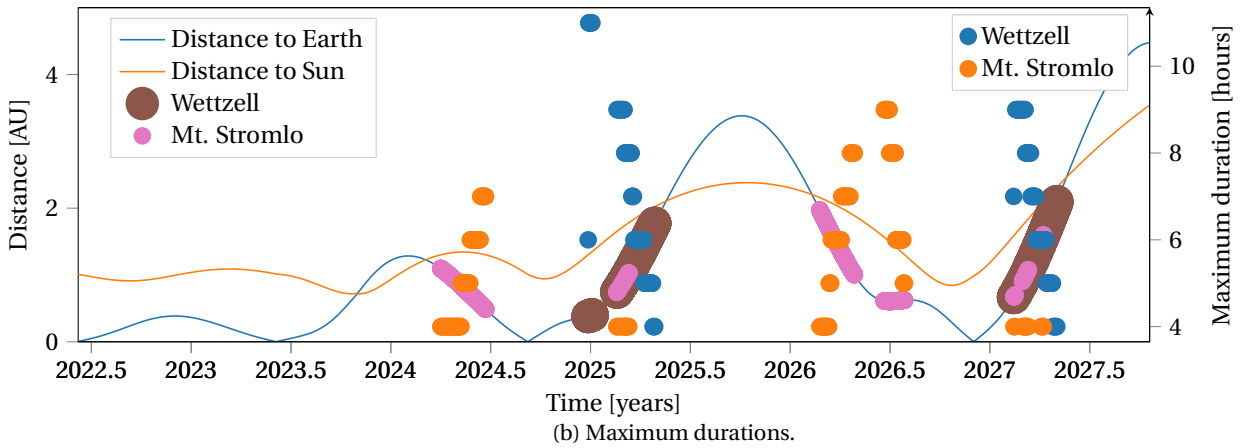

(b) Maximum durations.

Figure 7.11: Night time laser ranging options beyond 1.3 AU distance to the Sun. Markers indicate possible options for the two ground stations while in combination with the mean elevations and maximum durations.

7.5.2. Case 2: High Gain Antenna Sun Pointing

For the second case, all four options are visible by a ground station as shown in Figure 7.12. The advantage of this case is that a smaller range is available compared to the first case, increasing the link budget. A disadvantage is the number of days available since with a maximum allowable offset from sun pointing of 3 degrees, most options are around 5-7 days. Furthermore only the third option, 2.3 is possible during night although only partly. If the full 10 hours visibility is to be used, the Sun will start to rise at some point.

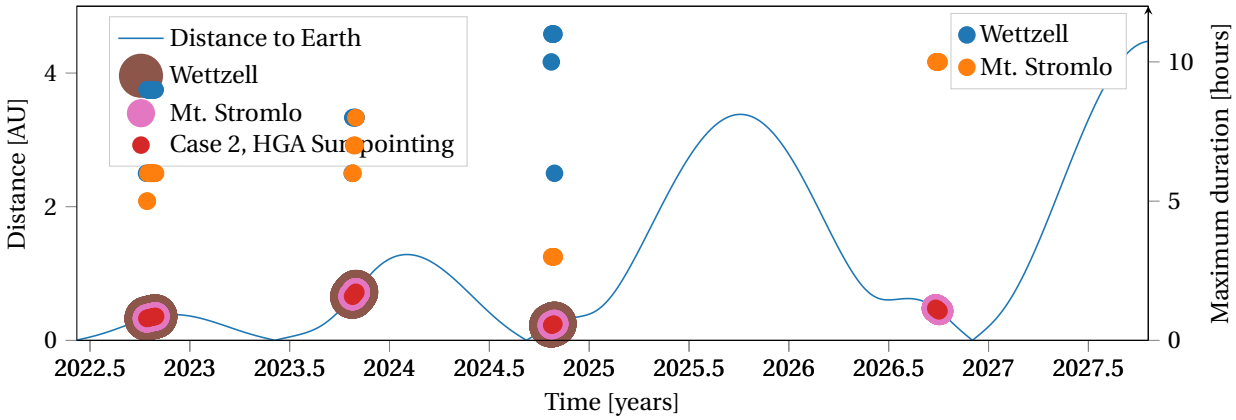

Figure 7.12: All options where the High Gain Antenna can remain Sun pointing due to an angle between the Sun and Earth of 90 deg as seen from JUICE. The right axis indicates the maximum duration available for laser ranging for the respective ground station.

Table 7.3 shows the options with their identifier. Note that the first day of option 2.3 is used throughout this study for reference as it provides still significant signal strength with a realistic distance, elevation and duration. Option 2.2 is around the same time as the Venus flyby and this option is probably not feasible but this is currently under investigation of the mission team.

Table 7.3: Overview of optimum options for laser ranging while maintaining HGA Sun pointing

Nr	Ground Station	Start	End	Range [AU]	Mean Elevation [deg]	Duration [hours]
2.1	Wettzell	08/10/2022	24/10/2022	0.34	43	9
2.2	Wettzell	19/10/2023	26/10/2023	0.68	39	8
2.3	Wettzell	17/10/2024	23/10/2024	0.23	52	10
2.4	Mt. Stromlo	20/09/2026	26/09/2026	0.46	55	10

7.5.3. Case 3: Near Earth flybys

Due to their small distance compared to the other options, case three provides excellent opportunities in terms of available signal strength. However the duration is limited to one hour only and this will severely impact the operations of the spacecraft and the ability for estimation of the ground station location. Therefore a strategy as adopted for the Hayabusa 2 LIDAR can be used where the scan window is divided into multiple smaller ones of which one per day can be scanned (Noda et al., 2017). Therefore the minimum time of these options is set at 20 days, allowing enough days as backup and for dividing the scan window. Figure 7.13 provides an overview of the options including the mean elevations. All options are available by either one of the ground stations and also the elevations are acceptable providing an elevation above 20 degrees for at least 4 hours. The ranges given in the summary in Table 7.4 indicate a high variability with a minimum range of 6 million kilometres and the maximum being almost 4 times more at 21 million kilometres. Also indicated is the possibility to do laser ranging at night or not and this also varies a lot. Currently these options are under investigation of the mission team since spacecraft operations are also required for the flybys. This includes lining up the spacecraft for an accurate flyby by using some burns just before the flyby. A positive side effect is that the position of the spacecraft is probably available with high precision both after and before the flyby, providing measures to decrease the range gate and thus be able to cope with more noise. Another side effect

of the flybys is that the flyby will never be as perfect as calculated in this trajectory model. Therefore the trajectory will be different after each flyby, although minor, especially for this case the dates are subject to chance depending on the accuracy of the flyby.

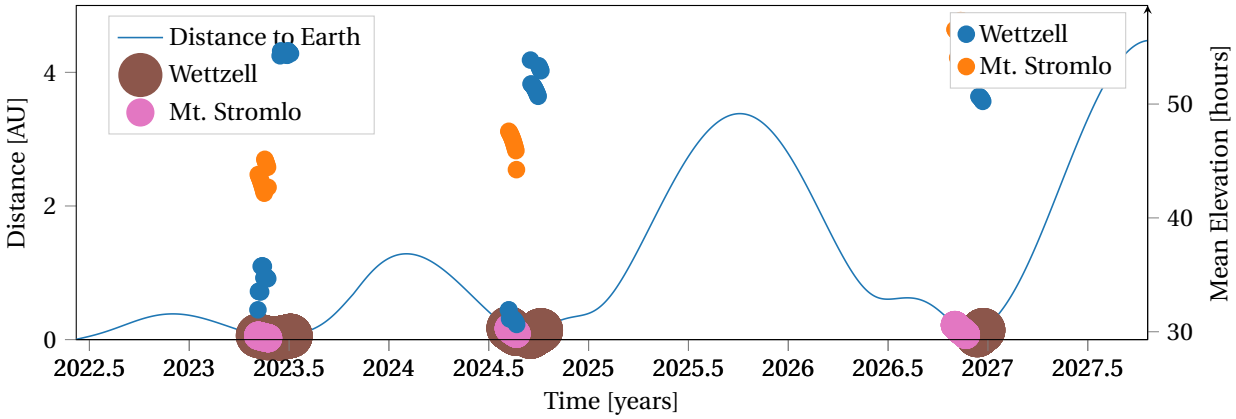

Figure 7.13: All options for laser ranging near Earth indicating also the mean elevations for the ground stations on the right axis.

Table 7.4: Overview of options for laser ranging near Earth flybys.

Nr	Ground Station	Start	End	Range [million km]	Mean Elevation [deg]	day/night
3.1	Mt. Stromlo	01/05/2023	20/05/2023	6	44	night
3.2	Wettzell	10/06/2023	30/06/2023	5.8	55	day
3.3	Mt. Stromlo	01/08/2024	20/08/2024	17.6	47	night
3.4	Wettzell	10/09/2024	30/09/2024	13.8	52	day
3.5	Mt. Stromlo	26/10/2026	16/11/2026	21.3	56	day
3.6	Wettzell	06/12/2026	26/12/2026	20.4	53	night

7.5.4. Best Options

From the previous discussions, a best option can be selected for each case yielding the best results. These are summarised in Table 7.5 and will be used later for analysis. Especially option 2.3, which provides a common range and duration is used as the reference case as it does not yield an extreme distance, elevation or duration and combines night time with day time ranging. Option 1.2 is chosen since it offers the smallest distance to Earth for case 1, combined with a reasonable elevation of JUICE. Furthermore the duration available is very long such that many shots can be fired during the scanning. Option 2.3 is the closest option for case 2 and the only one available during the night. Thus this will reduce the noise significantly making detection easier. Option 3.1 is chosen also because of its distance. It is the one the closest to Earth for case 3 and since the duration is limited to 1 hour for all of these options, this option will perform the best.

Table 7.5: Overview of optimum options for each of the three cases.

Nr	Ground Station	Start	End	Range	Mean Elevation [deg]	Duration [hours]
1.2	Wettzell	21/12/2024	28/12/2024	0.39 AU	51	11
2.3	Wettzell	17/10/2024	23/10/2024	0.23 AU	52	10
3.1	Mt. Stromlo	01/05/2023	20/05/2023	6 million km	44	1

8

Results and Discussion

With the development of a robust simulation tool it is possible to produce a statistical significant value for the calibration error. This calibration procedure is influenced highly by the distribution of the detected laser pulses. Therefore it is interesting to see which characteristics govern the laser ranging calibration and in what way. Section 8.1 will introduce the settings for which the simulations are run to be able to compare the variable settings in a fair way. Section 8.2 will compare the two developed attitude models and give a thorough discussion on the results obtained. Then Section 8.3 will discuss the influence of the slew rate after which Section 8.4 will elaborate on the influence of the threshold in both day and night time conditions. Section 8.5 investigates the influence of the distance on the calibration which is the largest contribution on the signal intensities. The final aim of this chapter is to conclude on a calibration accuracy which is done in Section 8.6 after which the influence of it on the science mission is discussed in Section 8.7.

8.1. Simulation Settings

The simulation requires many parameters as inputs for the calculation of the shots and their intensities. This holds for the ground station properties, GALA properties, scanning strategy and positions of GALA and the ground station. In order to be able to compare certain inputs it is necessary to define settings or inputs that can change and those that will stay the same. Table 8.1 summarises the fixed settings that will be used throughout this chapter. All sections will use the reference case to make a fair comparison when other settings are changed. The worst and best case will be used only in Section 8.6 to see if the calibration accuracy can be improved by changing these settings.

Table 8.1: Settings for the three test cases.

Parameter	Reference Case	Worst Case	Best Case
Telescope diameter [m]	0.75	0.75	0.75
Optical efficiency [-]	0.5	0.22	0.5
Quantum efficiency [-]	0.2	0.2	0.7
Spectral bandwidth [nm]	2	12	0.3
Receiver FOV [arcsec]	9	20	9
Dark Noise [kHz]	15	100	4
Case identifier	2.3		
Mean range	33501982 km (0.23 AU)		
Start time	2024 OCT 17		
Stop time	2024 OCT 17		
Duration	4 hours		

The first part of Table 8.1 is a selection op appropriate ground station characteristics and is composed by selecting the worst, best and representative values from Table 4.3 in Section 4.3.3. The first three settings, the telescope diameter and optical and quantum efficiencies all influence the strength of the signal. The

telescope diameter is the one used by Wettzell and the optical efficiency for the reference case was agreed upon with the Wettzell team (Schreiber, 2017). The worst case value of 0.22 corresponds to the lowest value found in Table 4.3 as is also the case for the quantum efficiency. The other three settings influence the noise on the signal by the dark noise and the Sun elevation that generates the solar noise. How much of the solar noise is detected depends largely on the spectral filter bandwidth, the size of the telescope and the quantum efficiency while the chosen APD and its settings and temperature determines the dark noise. The selected spectral filter bandwidths and the receiver FOVs represent the ranges found in Table 4.3 while the selected dark noises were discussed in Table 3.1 in Section 3.4. The reference case represents a representative ground station, focused on the performance by Wettzell, the envisioned candidate for laser ranging.

The second part of Table 8.1 shows the laser ranging option used which is the same as used in Chapter 6. The most important parameter coming from selecting the option is the distance. This will highly influence the link budget and this effect will be discussed in Section 8.5 and is one of the variable settings.

The other variable settings will influence the distribution of the laser shots. Since the calibration procedure is based on the distribution of detected shots it is interesting how the calibration will perform when varying the distribution. The distribution can be influenced by the slew rate, the laser ranging duration, the scan window and the scanning pattern. Starting with the scanning patterns explained in Section 5.2, two options are available, a sweep scanning pattern and a vortex scanning pattern. The sweep scanning pattern can be equally spaced by using the same amount of shots in both x and y direction through a combination of slew rate, scan duration and scan window. Only equally spaced sweep scan patterns will be considered since an unequally spaced pattern will deteriorate the estimation in x or in y. When for example the number of shots per sweep is greater than the amount of sweeps, there will be more information available for the y axis estimation. Since the goal is to have a fair comparison and to produce one number that can be used both for x and y, as is done in Section 5.1 where the pointing budgets were discussed, equal spacing will be used.

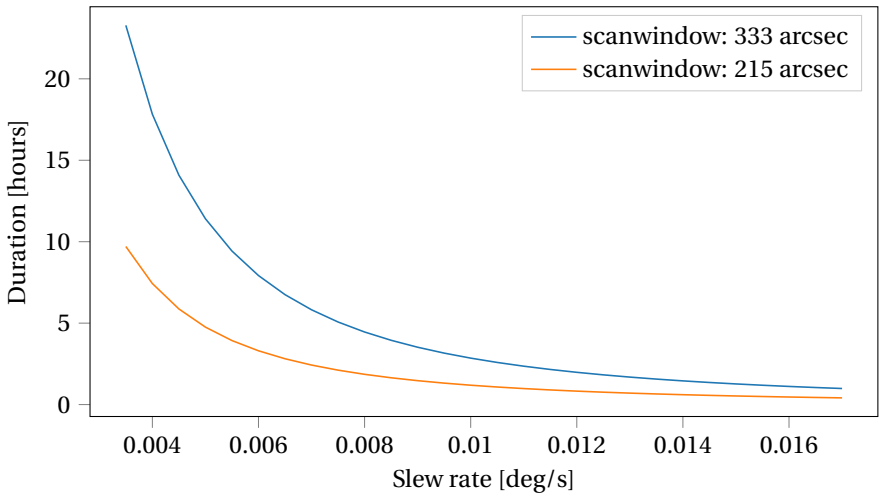

Figure 8.1: Durations for the two scan windows.

Thus by choosing a combination of the other three variable settings, the scan duration, window and slew rate, an equal spacing is created for the sweep scan pattern. Since the slew rate is the same for the vortex pattern, the shot to shot distance in the same scanning line is also the same and only the shot to shot distance from line to line, or vortex ring to vortex ring, is different. Table 5.2 defined the scan window that should be scanned for laser ranging at 333 arcsec and 215 arcsec. Since this is a fixed value, the duration and slew rates can be determined as shown in Figure 8.1. For the scan windows a line is plotted indicating the slew rates and durations. The maximum duration that is generally available was found to be 10 hours. In Chapter 7 it can be seen that it is possible to have a slew rate below 0.004 deg/sec for the smaller scan window of 215 arcsec. However for the large scan window, this results in very high durations, not possible if only one ground station is to be used. A possible way to overcome this problem is to use multiple ground stations located at such a distance from each other, that a continuous visibility of JUICE remains. This is certainly possible in the northern hemisphere where enough laser stations are available at approximately the same latitude as the Earth turns around. Table 8.2 summarises slew rates for common durations and the two scan windows. The rates range from 0.0034 to 0.017 deg/s which are acceptable values within the capabilities of the spacecraft

(European Space Agency (ESA), 2017) and serve as the input values further in this chapter. The effect of the slew rate will be investigated in Section 8.3.

Table 8.2: Common slew rates including the maximum and minimum rates.

Scan window / Duration	1 hour	4 hours	8 hours	10 hours
215 arcsec	0.011 deg/s	0.0055 deg/s	0.0039 deg/s	0.0034 deg/s
333 arcsec	0.017 deg/s	0.0084 deg/s	0.0060 deg/s	0.0053 deg/ss

8.2. Influence of Attitude Models

As discussed in Section 5.2, the attitude of the satellite is not perfect and is modelled using Table 5.5. Two models were created here which will be compared in this section. This section also discusses more in depth all results from the simulation while other sections will focus only on the final calibration accuracy. For both models, ground station estimations were done using photon intensity information as well as pulse detections. Also both scan patterns were simulated and the overview of all these results in summarised in Table 8.3. The photon intensities with the shot distributions are compared for the two models in Figures 8.2 and 8.3 which will help in the discussion on the differences.

Table 8.3: Overview of the results of the simulation for the two attitude disturbance models, the random walk and the pure Gausian model.

		Random	Walk			Pure	Gaussian	
Scanning Pattern Photons / Pulses	Sweep Photons	Vortex Photons	Sweep Pulses	Vortex Pulses	Sweep Photons	Vortex Photons	Sweep Pulses	Vortex Pulses
Average error X [arcsec]	2.6	2.16	1.92	1.63	1.26	1.42	1.03	1.08
Average error Y [arcsec]	3.01	2.14	2.14	1.62	1.44	1.38	1.05	1.04
Mean error X [arcsec]	0.21	0.040	0.11	0.091	-0.018	-0.0003	0.06	-0.015
Mean error Y [arcsec]	0.033	0.066	0.32	0.10	0.078	0.05	0.13	0.15
Standard deviation X [arcsec]	3.19	2.68	2.37	2.04	1.59	1.82	1.29	1.36
Standard deviation Y [arcsec]	3.74	2.69	2.62	2.06	1.78	1.73	1.33	1.31
Mean I_0 [photoelectrons]	165	131	-	-	172	150	-	-
Standard deviation I_0 [photoelectrons]	50	34	-	-	45	42	-	-
Mean w [arcsec]	18	19	-	-	17.5	17.6	-	-
Standard deviation w [arcsec]	3.1	2.5	-	-	2	2	-	-
Mean number of detected pulses	-	-	1130	1095	-	-	1131	1098
Standard deviation detected pulses	-	-	172	146	-	-	116	113

The main result here is the difference in how good the estimation procedure can locate the position of the ground station. Where the standard deviation for the random walk is 2.06 to 3.74 arcsec, the standard deviation for the pure Gaussian is 1.31 to 1.78 arcsec. The estimation is almost twice as bad in case of the random walk. Thus it can be confirmed that the random walk is the worst case of the two, as was the goal of the attitude modelling in Section 5.2. In both cases the means are indeed around zero and the average errors follow the standard deviation, again the averages are worse for the random walk.

This difference in performance can be explained by looking more closely to the main difference of the two models which were depicted in Figures 5.9c and 5.10. The pure Gaussian attitude model has much higher shifts in attitude as this can jump suddenly from 20 to -20 arcsec. However since it is nicely Gaussian distributed, the overall shot distribution should not be biased but evenly spread. This is different for the random walk that randomly walks within the bounds and thus can deviate from the commanded attitude for a longer time and will not make sudden jumps. Since the random walk can deviate from the commanded attitude for a long time, the commanded scanning pattern will be followed worse than for the Gaussian case. For example for the sweep scan pattern, when one sweep has a large deviation away from the ground station and therefore does not produce detectable shots, the next sweep could have a deviation towards the ground station and therefore produce better shots then expected. Using the same reasoning as above, also a higher standard deviation in detected pulses is expected for the random walk and this is indeed the case since the standard deviation is 146 compared to 113 for the detected pulses. The same holds for the standard deviations of the peak intensity I_0 and the divergence angle w. The standard deviations of I_0 for the random walk lie at 50 photoelectrons compared to 42 for the Gaussian case and the standard deviation for w is 3 arcsec compared to 2 arcsec for the pure Gaussian. This all ultimately leads to the fact that the estimation error is lower for the pure Gaussian which is an expected result.

The differences in the two models can also be shown by plotting the shot distribution over the ground station. Figures 6.5 and 6.6 compare for both patterns the two models. Here two large effects can be seen that make the models different. First, the spread seen in the commanded attitude is much larger for the pure Gaussian when comparing Figures 8.2a and 8.2c. This is expected since the deviation is allowed much further away from the desired attitude than for the random walk. The random walk is bounded while the Gaussian is not bounded by 15 arcsec, only in its final distribution this is a bound. Secondly, looking at the real attitudes for the pure Gaussian in Figure 8.2d, the desired pattern is still visible. For the sweep pattern, the sweeps are visible and for the vortex pattern one can still make up the individual vortexes although they are shifted. This is not the case for the random walk in Figure 8.2b, here the shot distribution seems to be very random and it is not possible to make up the shape of the commanded scan pattern in these figures. One of the causes for this, is that the random walk is allowed to walk at a very high frequency while the Gaussian model is fixed to a slower frequency in order to fulfil the 3 arcsec stability over 500 ms. However the Gaussian model is allowed to have very large fluctuations causing the higher spread for the commanded attitude.

In the long run, the larger spreading in the commanded attitude for the pure Gaussian does not create a larger standard deviation for the estimation error since the estimation is better for the pure Gaussian. Thus the better retained scan pattern results in a better estimation of the ground station position. This confirms the initial reasoning that the attitude model should be a worst case with a random spread of the shots as is possible. This is clearly achieved by the random walk model compared to the Gaussian model and thus in the remaining study, this model will be used.

The verification in Section 6.3 showed and discussed the resulting estimation errors of the ground station when the attitude of the spacecraft is not disturbed. When the disturbance is included in the simulation, information about where the shots hit the target is lost. The shot will be fired at a different position which is uncontrollable and the only information available is the commanded attitude. However still roughly the same average number of shots should be detectable since the scan window is larger than the deviation in the attitude and thus it should still be possible to determine the mid point of the Gaussian pulse shape and estimate the position of the ground station. This is confirmed in Table 8.3 with a mean number of detected pulses which is the same as found during the verification in Table 6.2. Since the positional information of the shots is spread out, the Gaussian that is fitted will be more spread out to cope with this effect. This is also confirmed in Table 8.3 when photon estimation is used where the mean divergence angle or width w is estimated to be 18-19 arcsec, more than the actual 10.3 arsec produced by GALA. A more spread out shape also should result in a lower peak intensity at the ground station and this is also confirmed with a mean I_0 of 165 and 131 photoelectrons while in Table 6.2 values of 494 and 433 were found.

Although the estimation uses a more spread out Gaussian when the attitude is disturbed, it is the mid point that determines the ground station and this is still within acceptable levels. The standard deviations are 3.74 to 2.69 arcsec when using photons for the estimation and 2.62 to 2.06 arcsec when using pulse detection. This is indeed much better than using the maximum standard deviation of the attitude error of 7.5 arcsec plus the divergence angle of the laser at 10.3 arcsec. There is a difference between the two scan patterns as the vortex pattern is consistently better than the sweep pattern by roughly 1 arcsec when photon estimation is used and 0.5 arcsec for pulse detection. However, a vortex pattern is only different around the four lines originating from the mid point towards the corners. Here a scan line will shift from horizontal to vertical

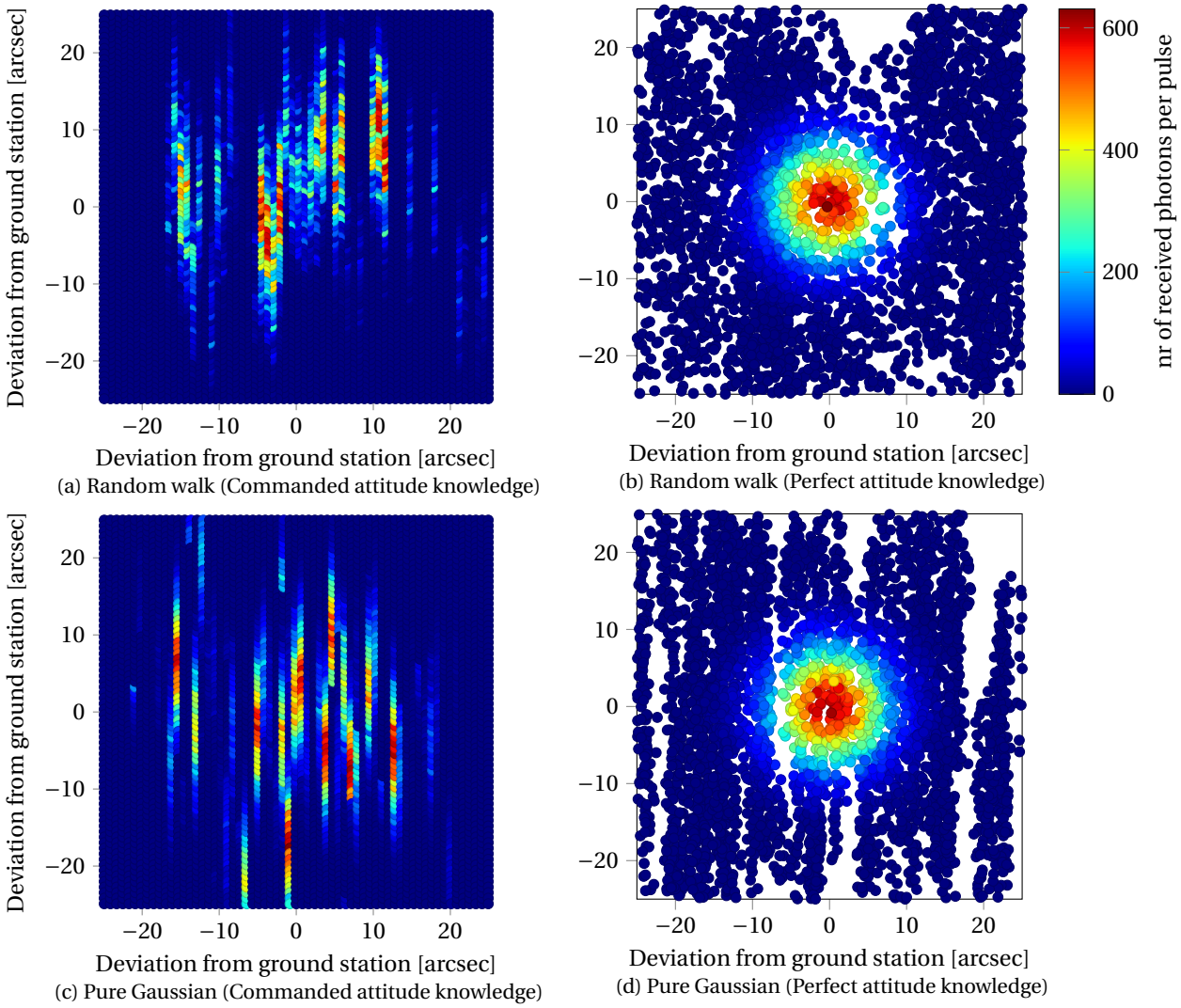

(a) Random walk (Commanded attitude knowledge)

(b) Random walk (Perfect attitude knowledge)

(c) Pure Gaussian (Commanded attitude knowledge)

(d) Pure Gaussian (Perfect attitude knowledge)

Figure 8.2: Comparison of the shot distributions and intensities of the random walk and pure Gaussian attitude disturbances using a sweep scan pattern for both cases. The left figures indicate the measured shot distribution using the commanded attitude knowledge for the two different models. Here the distribution is caused by the errors from Table 5.6 and this will be used for the ground station estimation later on. The right figures show the actual true shot distribution, which would be the information available if the attitude knowledge was perfect.

direction or vice versa when it goes around the corner. Between the corners, the pattern is exactly like the sweep scan pattern although above and underneath the mid point, the sweeps are in horizontal direction, while left and right of the mid point, the sweeps are in vertical direction, just like the sweep scan pattern. Only the spacing from line to line is different for the vortex pattern but otherwise the vortex rotates the scan direction of a sweep pattern by 90 degrees for almost 50% of the time. In the long run this yields a slightly lower standard deviation and a more stable estimate of the estimation accuracy since there is no difference for the x and y coordinate any more. Therefore it is decided to use the vortex pattern for further analysis in this chapter. Also the estimation errors and standard deviations will not be separately shown for x and y but the average is used since one could simply rotate the spacecraft around the z axis and repeat the pattern and get the result for x now for y and vice versa. Note that also from now on, the computed error will be the standard deviation as this is the value that is the final aim for this chapter.

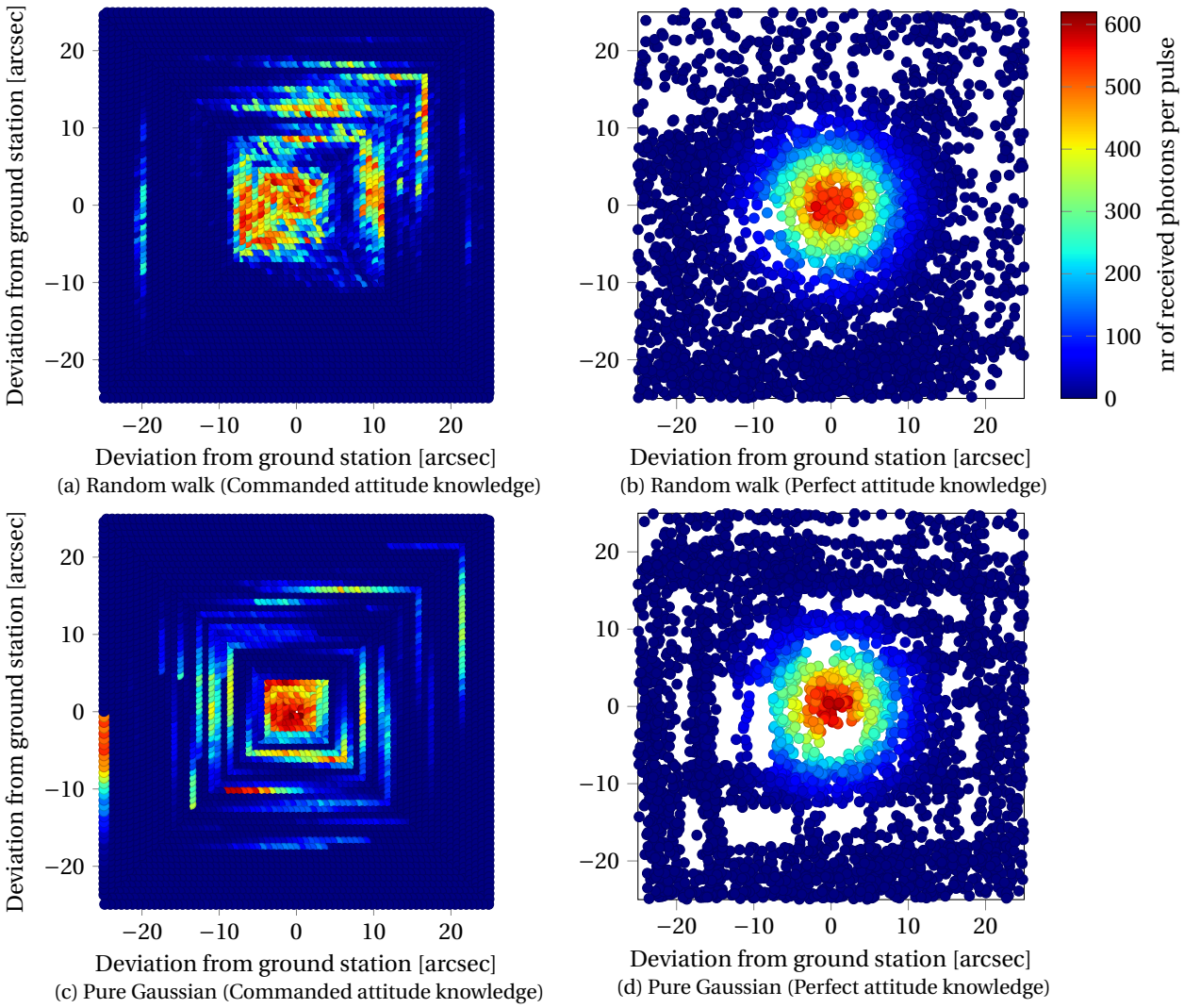

(a) Random walk (Commanded attitude knowledge)

(b) Random walk (Perfect attitude knowledge)

(c) Pure Gaussian (Commanded attitude knowledge)

(d) Pure Gaussian (Perfect attitude knowledge)

Figure 8.3: Comparison of the shot distributions and intensities of the random walk and pure Gaussian attitude disturbances using a vortex scan pattern for both cases. The left figures indicate the measured shot distribution using the commanded attitude knowledge for the two different models. Here the distribution is caused by the errors from Table 5.6 and this will be used for the ground station estimation later on. The right figures show the actual true shot distribution, which would be the information available if the attitude knowledge was perfect.

8.3. Influence of Slew rate

The slew rate is the largest contributor that governs the spacing between the shots and is, besides the scan pattern, the most important setting for the spacecraft operations. Section 8.1 discussed which settings are available and here the influence will be discussed. Besides the frequency which is fixed at 30 Hz this setting will determine how close the shots are fired with respect to each other and it will determine how long it takes to scan the entire scan window as was depicted in Figure 8.1. Given the 30 Hz and the scan rate a number of lines will cross the ground station that are detectable resulting in a number of detected pulses as depicted in Figure 8.4. Here the relationship between the mean number of detected pulses and the slew rate is shown which behaves as expected since it decreases with an increasing rate for a duration of four hours. The mean drops to a few hundred pulses when the entire scan window is to be scanned within 1 hour. Here the shots are more than 2 arcsec away from each other while more than 3000 pulses are detected when a slew rate of 0.0035 deg/s is used resulting in a spacing of 0.42 arcsec between each shot in both horizontal and vertical direction. Laser ranging was simulated for the 2.3 reference case as set up in Table 8.1, during night time. Each time the slew rate was changed and the ground station position was estimated, this was done 1000 times for every slew rate. It is interesting to see how the ground station estimation behaves for the different slew rates. A faster rate basically provides less information to the estimator and this is reflected by the estimation error in Figure 8.4. It increases with slew rate due to increased spacing between each shot and a decreased number of detected shots and this seems to be an almost linear relationship. For a very slow slew rate, it is even possible to get the standard deviation below 2 arcsec but this will require very long laser ranging that is practically not possible to carry out during only night time as was shown in Table 8.2. Here it will take 10 hours and the scan window of 215 arcsec to be able to us this slow rate. However an important result is that even for high scan rates the estimation accuracy does not diverge and is still acceptable and also no increase in outliers was observed. Thus the scanning can be done in various settings and adapted to fit the duration possible and accepted by ESA.

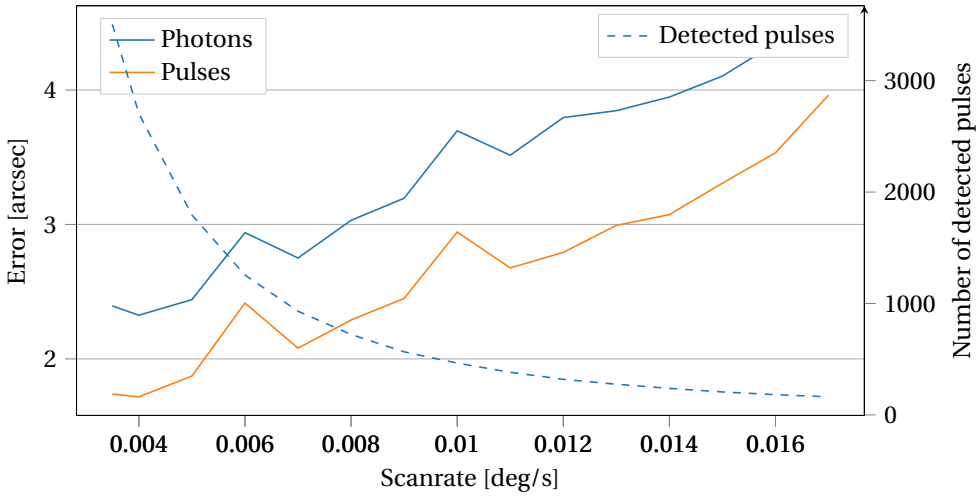

Figure 8.4: The standard deviation of the ground station estimation error for different slew rates for a scan duration of 4 hours. Both the estimation errors using the photons as well as the pulses are given. The right axis indicates the number of detected pulses for the scan rate. The peaks are statistical artefacts deviating from the mean trend.

8.4. Influence of Threshold

Whether or not the received number of photons indicate a shot or not will be decided using threshold detection as explained in Sections 3.5 and 6.1.1. This threshold is used to discriminate the signal from the noise but by setting a threshold also signal is lost in the case it is lower than the threshold. As seen in Section 8.3 , loss of information will probably lead to a higher estimation error. However the threshold is a very different setting compared to the spacecraft operations as it is based on the received noise levels that is governed by the equipment used at the ground station. Also by this setting, spacing of the laser shots is not changed but the information is lost in a different way, basically setting a border at some distance from the ground station

where it is no longer possible to detect shots. For a certain threshold one can govern the amount of pules detected and how far from the ground station these are detected. Thus as the threshold increases the scatter plot of detected pulses converges towards the ground station. This effect will first be studied using night time ranging. Afterwards the influence of the threshold is investigated when laser ranging is performed in day light, as this is where threshold is required most and makes a large difference.

8.4.1. Night time ranging

For night time ranging again the reference case 2.3 is used for Wettzell. A four hour scan is done and the threshold is varied for each run. Figure 8.6 shows four typical examples of the distribution of the detected shots. The initial idea was that the number of shots would converge towards the ground station as the threshold is increased. Although part of the spread of the detections in Figure 8.6a is gone in Figure 8.6d, still a large spread is present due to the attitude errors. Figure 8.6a still suffers from some false detections and these are clearly gone in Figure 8.6b. The higher thresholds reduce the amount of detections to just over 100 detections for the highest threshold leaving only some scattered detections with still a large spread.

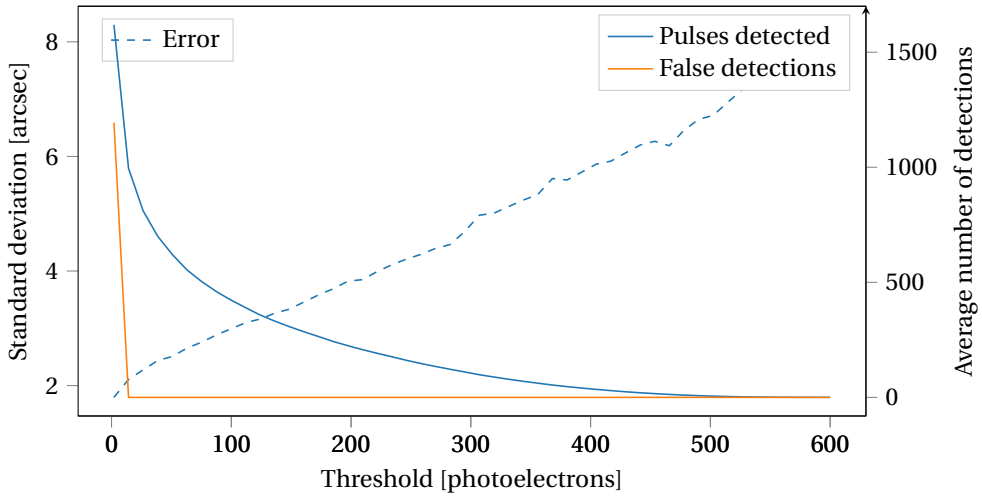

Figure 8.5: Number of detected pulses for the chosen thresholds for a scan duration of 4 hours.

Figure 8.5 shows the results of the estimation for the various levels of threshold. Here the estimation error ranges from 2 to 8 arcsec and interestingly enough is a worse result than when the slew rate is increased where the maximum error was only 4 arcsec in Section 8.3. This is mostly since at the high thresholds up to 600, almost no detections take place at all. During the simulation runs, often there was no detection at all and the result was taken out. Therefore the number of successful runs is low in the higher threshold regime but still provides a good indication of what to expect. It can also be observed that the dark noise is easily overcome by a threshold while still yielding good results. Here the reference case with a dark noise of 15 kHz is used and this proves to be no problem at this value. It was expected that it was possible to still have good results for setting a high threshold since the pulses would converge to the ground station such that a good estimation is still possible. This is not confirmed here since the error gradually increases with the threshold. Thus indeed the more information is available, the better the estimation, regardless of where the information is lost, since here the information about pulses further from the ground station is lost. Also the number of detected pulses rises rapidly for a lower threshold as expected.

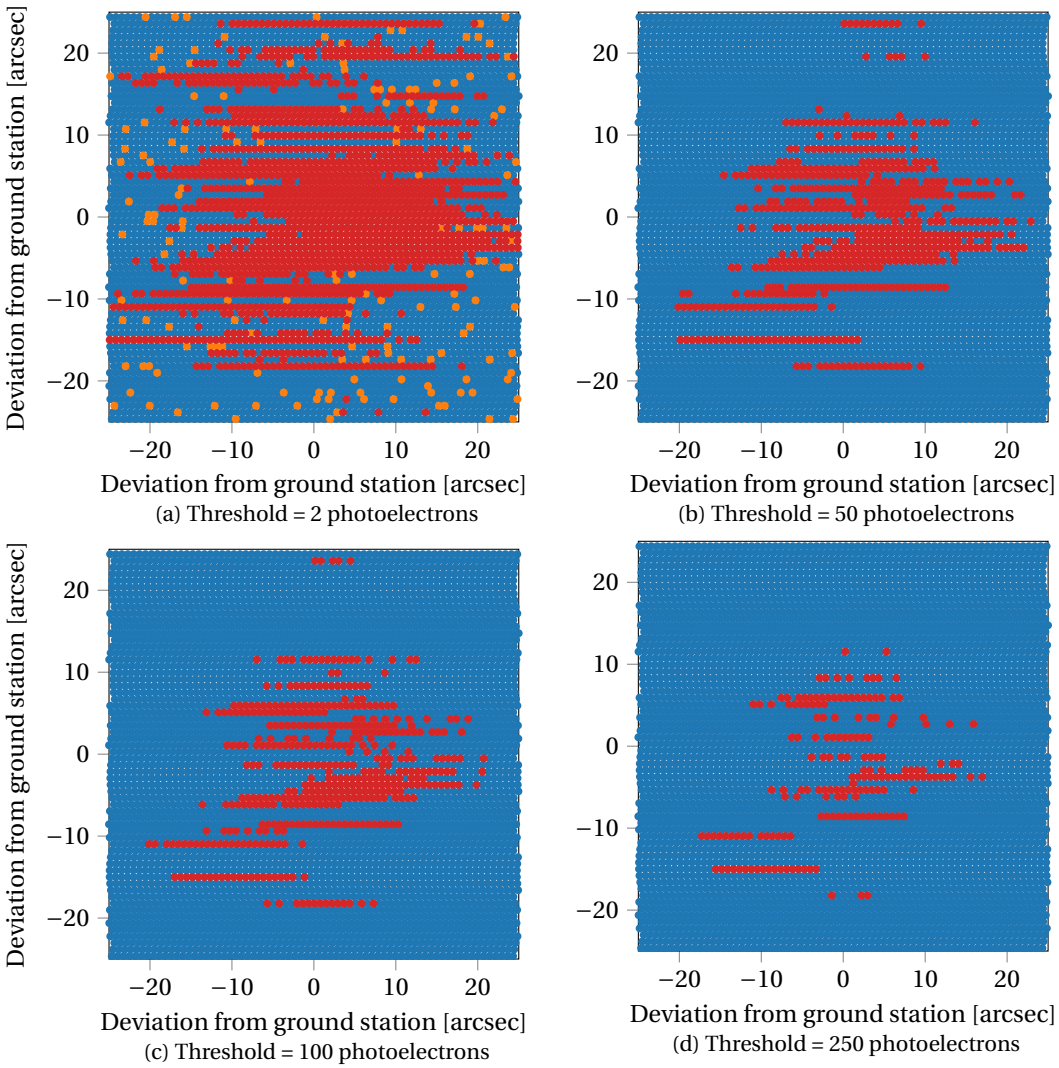

(a) Threshold = 2 photoelectrons

(b) Threshold = 50 photoelectrons

(c) Threshold = 100 photoelectrons

(d) Threshold = 250 photoelectrons

Figure 8.6: Detection distributions for the commanded attitude knowledge during a night time scan, showing various thresholds. Red indicates a detected shot while orange indicates a false detection. False detections are only visible for a low threshold since only dark noise originating from the APD is present in this case. Note that in reality the difference between false detections and true detections is not known and therefore the ground station position estimation uses all detections combined.

8.4.2. Day time ranging

In daytime ranging a different problem is at hand. Here the estimation does not only depend on the number of detections, but now also to which level it can still estimate the ground station correctly given noise detections. Since the false detections will be distributed randomly, the pulses at the ground station should cause an part of the data where the number of detections is suddenly increased, indicating the location of the ground station. This is visualised in Figure 8.7 where four sets of data are shown with increasing Sun elevation, causing more and more false detections. The figures show the data that is used to estimate the ground station position and indeed up to 35 degrees Sun elevation the sweeps caused by the shots are still visible for the eye. However the estimation procedure does not rely on visual inspection although this could be a possibility in the real case, but rather on fitting a Gaussian through all detected pulse distributions.

In the figures every single shot is shown where a red dot indicates a detection, orange a false detection and blue no detection. Whether it is a pulse or false detection is unknown to the estimation procedure. Then by introducing a grid with a certain grid size, lets say 2 arcsec, all detections are collected in each grid and each grid is assigned a number of detections. This will introduce a certain spatial distribution, used to find the top of the Gaussian pulse shape, causing this distribution. With noise, the shape is heavily disturbed

depending on the amount of noise and at some point the least squares estimation will no longer be able to build a distribution of detections on which a Gaussian can be fitted of which its peak intensity corresponds to the ground station.

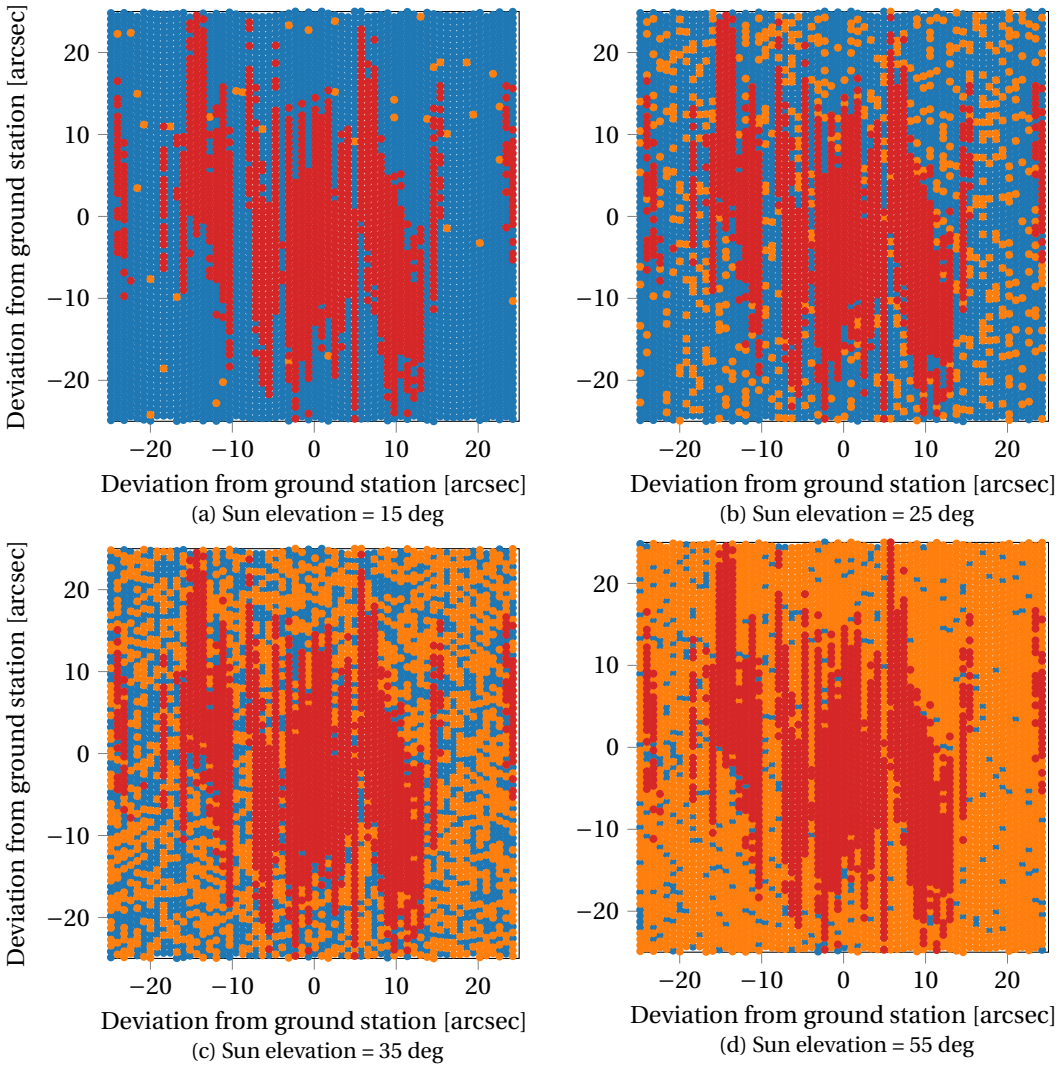

Figure 8.7: Detection distributions for the commanded attitude knowledge for various Sun elevations during day time for a constant threshold at 9 photoelectrons. Red indicates a detected shot while orange indicates a false detection. Note that in reality the difference between false detections and true detections is not known and therefore the ground station position estimation uses all detections combined.

This effect is visually depicted in Figure 8.7d where it is even visually difficult to discriminate the signal from the noise. Getting an estimate of the ground station down to a few arcsec is even more difficult because of the large amount of noise. Basically at this point more false detections take place than pulse detections as seen in Figure 8.8a. For the threshold of 9 photoelectrons, already at 25 degrees the amount of false detections is larger than the number of pulse detections in a window of 50 by 50 arcsec. This window is chosen such that it captures all possible pulse detections given the beam divergence angle and the attitude disturbance. For this window the number of false detections and pulse detections are determined and shown in Figure 8.8a for four different threshold settings. The different behaviour of the threshold settings is indicative for what a threshold is, a sudden limit where it is decided if a pulse is detected or not. Therefore, although the setting is changed from 8 to 11, the difference in false detections is large while the difference in pulse detections is only very minor. This supports the idea behind the threshold detection where with losing a minimum on pulse detections the false detections can largely be reduced to an acceptable level. Figure 8.8b shows the corresponding error of the ground station estimation and also support this conclusion. A threshold of

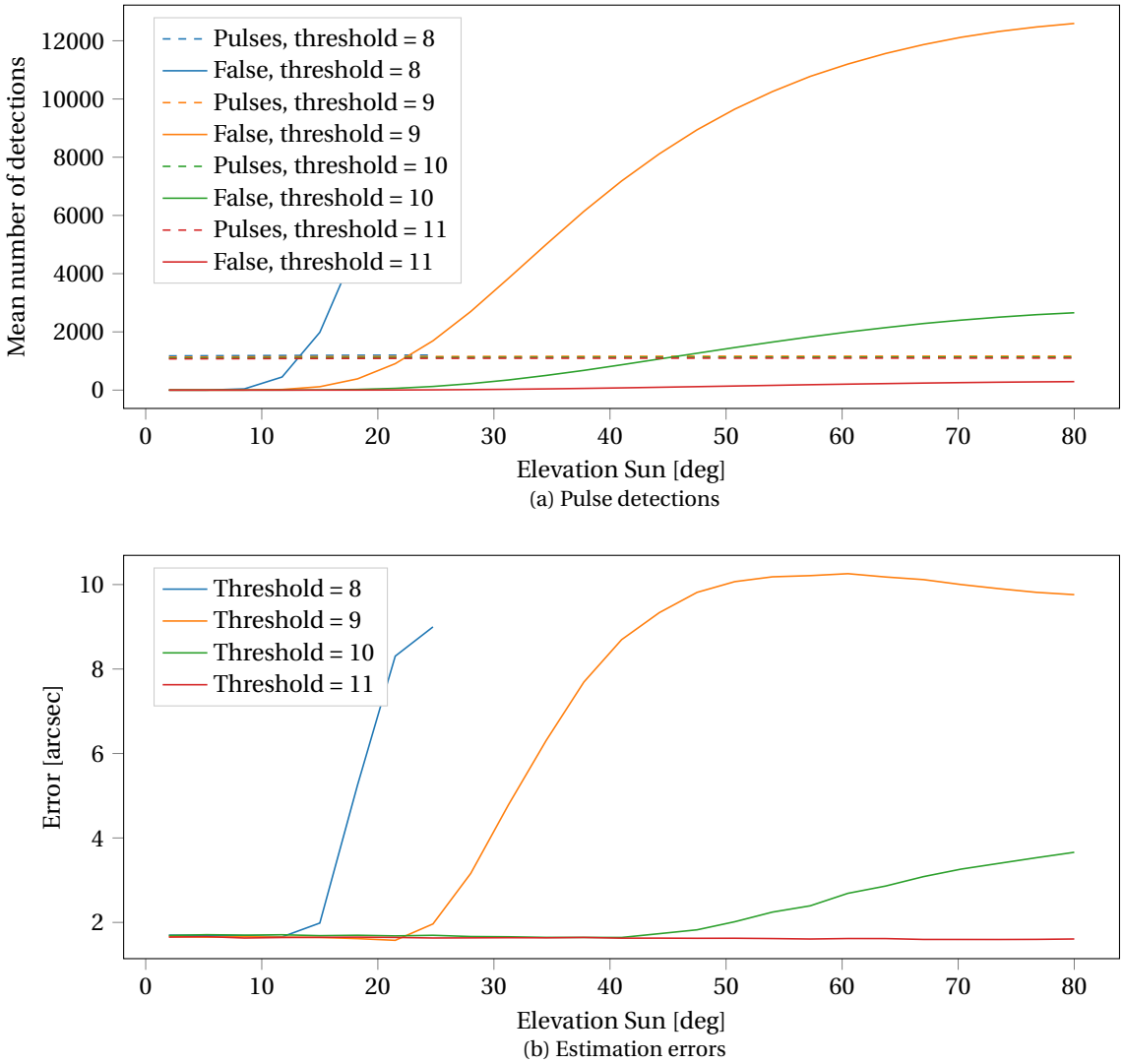

Figure 8.8: Behaviour of the ground station position estimation procedure for increasing Sun elevation using various thresholds for a day time scan. The influence of the threshold on the number of detections is presented at the top with the resulting estimation errors in the bottom figure.

11 makes sure that proper estimation is possible even with high Sun elevation and this is a large difference compared to a threshold of 8 or 9 that starts to deviate from an acceptable error even for lower Sun elevations.

Given these large differences for thresholds that only differ a few photoelectrons, it becomes apparent that setting a threshold is a very sensitive parameter for the pulse estimation and here it seems that it is better to set a higher threshold to be sure that noise is reduced. However this is the case when a large amount of shots is available for detection. This number greatly reduces with distance and at some point the threshold will reach the level of signal available for distances greater or equal to around 2 AU. Then a different regime is encountered where the threshold should be set according to the hardware of the ground station. The quantum efficiency, telescope aperture, dark noise, field of view and spectral bandwidth all will influence the required threshold. Although this will only differ a few photoelectrons, it has just been shown that these photoelectrons make a large difference. Therefore it is decided to make no further analysis on a limiting case where laser ranging is to be performed at a large distance with low available signal intensity. Enough night time options exist at large distances and the information on the equipment is not abundant enough to make a proper assessment for this. Also the influence is easily determined by looking at the equations and the effect of the mentioned properties. Except for the dark noise, which depends on the chosen APD and its temperature, all other properties are only a factor multiplying the solar and signal intensity. Thus a larger telescope will mean that more noise is received but also more signal is received so the threshold can be scaled up accord-

ingly without losing information and ending up at the same ratio of false detections to pulse detections. The same holds for the quantum efficiency, spectral bandwidth and field of view which are all dependent on the equipment available.

Furthermore it would also be possible to apply statistical methods in the temporal information. So far only statistical distributions in spatial information has been used to determine the ground station, but noise behaves randomly while pulses will arrive with a fixed frequency of 30 Hz. If enough pulse detections take place, it will be possible to discriminate a part of the noise from the signal and thus delete these noise detections, making a better estimate possible. This would require precise timing and simulation of the timing which has not been incorporated here. However the ground station position is still a spatial estimation and Figure 8.8b shows that for a proper threshold, the estimation can be carried out still with good precision.

8.5. Influence of Distance

So far all analysis has been done on the reference case at 0.23 AU distance from Earth. This is a case at medium distance and here the influence of the distance will be investigated by running simulations at different distances up to the option with the largest distance from Earth. In all cases, Wettzell will be used and only night time ranging is included. In the reference case, only the distance is changed, leaving the elevations and other conditions unchanged. Figure 8.9 presents the results in terms of estimation error and the number of detected pulses with respect to the distance. The results are comparable to changing the slew rates in terms of estimation error in Figure 8.4 in Section 8.3. A larger distance causes less detected pulses and degrades the estimation accuracy significantly. This is an expected result since information is lost due to the increase in distance and thus the shape of the Gaussian pulse becomes less and less prominent which makes it more difficult to fit. Here a higher quantum efficiency or larger telescope area would greatly benefit the result since the number of pulses detected will be increased. Also a lower dark noise would allow a lower threshold resulting in more detections and a better estimation accuracy. This is one of the main influences of choosing the ground station and essentially increasing the distance has the same effect as choosing a smaller aperture or lower quantum efficiency. The effect of the threshold is different as was explained in Section 8.4.

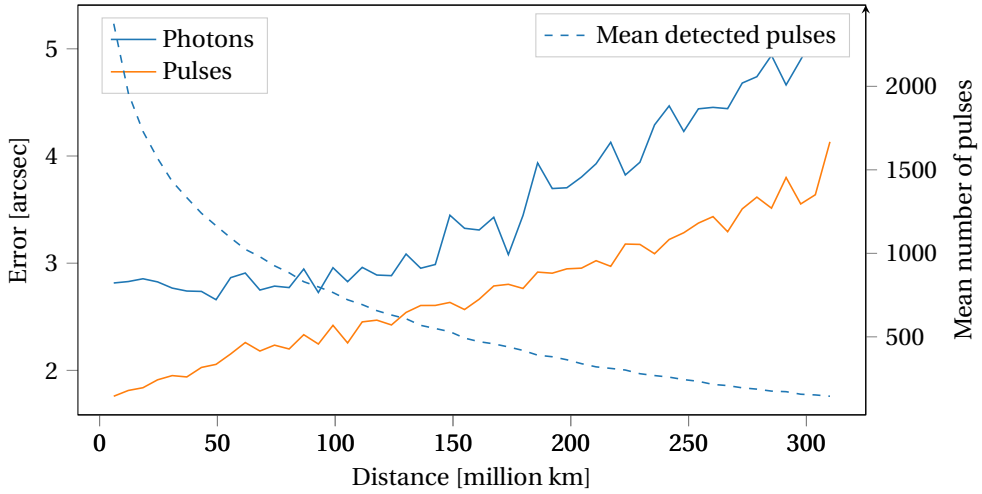

Figure 8.9: Estimation error and number of detected pulses for a threshold of 4 photoelectrons for the 2.3 reference case with varying distance.

Figure 8.10 shows the photon intensities and detections for the case found in Chapter 7, case 1 and number 4 in Table 7.2 but then choosing the latest possible option, which has the greatest range of 2 AU. The simulation is done using the Wettzell ground station and the reference settings found in Table 8.1. Given this opportunity, only a scan duration of 5 hours is available and the slew rate is set to 0.0075 deg/sec accordingly to be able to scan the 333 arcsec scan window. Although the maximum intensity found is 10 photons, it has to be kept in mind that only a few pulses will reach this intensity, most will be in the range of 2 - 6 as seen in Figure 8.10a. Therefore not many pulses will be detected with a threshold higher than 3 photoelectrons. Here the limit of the capabilities of the ground station and the used properties is reached in terms of telescope size and efficiency with only around 100 detectable pulses. When this case would be required it is advisable to use

another ground station or APD to increase the intensities and bring up the detections to at least 500 pulses to attain an acceptable accuracy as can be seen in Figure 8.5 where it was shown how many pulses are required for a certain accuracy.

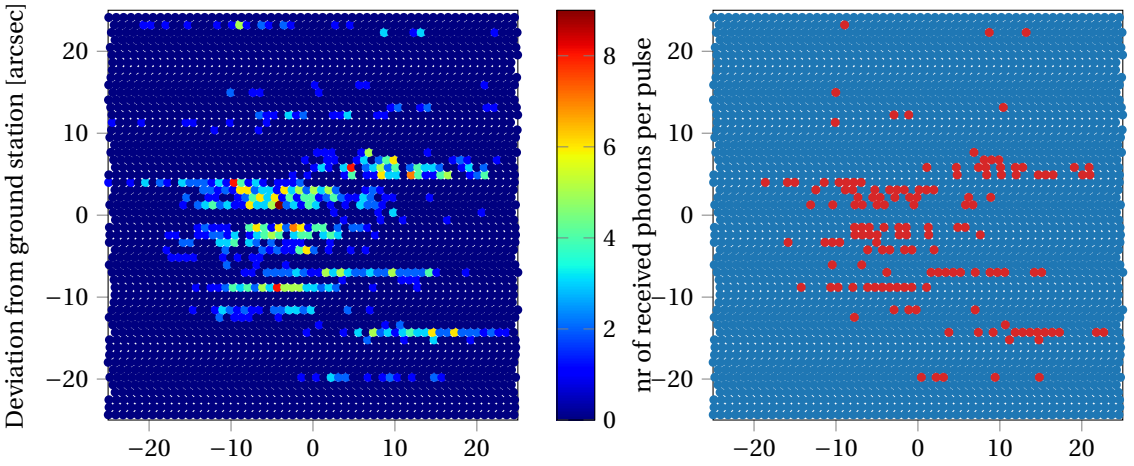

(a) Photon intensities

(b) Detected pulses (threshold = 3)

Figure 8.10: Scatter plots at the maximum distance of 2 AU showing the commanded attitude knowledge for both the photoelectron intensities as well as the detected pulses.

8.6. Calibration Accuracy

Now that all effects have been investigated an assessment of the estimation accuracy can be made using the different cases from Section 7.5.4 and the three different settings for the ground stations from Table 8.1.

Table 8.4: Calibration accuracies for the three best options.

	Case 1.2	Case 2.3	Case 3.1
Ground Station	Wettzell	Wettzell	Mt. Stromlo
Duration [hours]	10	9.5	1
Slew rate [deg/s]	0.0055	0.0055	0.017
Range	0.39 AU	0.23 AU	6 million km
Worst case			
Threshold [photoelectrons]	3	30	3
Error [arcsec]	1.68	2.55	6.39
Reference case			
Threshold [photoelectrons]	3	10	3
Error [arcsec]	1.67	1.75	4.53
Best case			
Threshold [photoelectrons]	3	8	3
Error [arcsec]	1.52	1.55	4.33

Table 8.4 presents the final standard deviations of the estimation error for the nine cases at hand. The difference between the worst and the best case is indeed as expected, in all cases the best case yields better results although the differences to the reference case are sometimes minimal. Thus the reference case was indeed a good example for a middle class option in terms of conditions positive for the estimation. Case 3.1, although very favourable in range is doing much more worse than the other with an error of 4.33 arcsec. This can largely be explained by looking at Section 8.3 where the slew rate was investigated. Since a one hour scan requires a high slew rate, the number of pulses detectable is low and consequently the estimation error is

higher. Case 2.3 should be able to perform almost as good as case 1.2 but suffers from the Sun rise, giving the need for a higher threshold and thus losing information. Case 1.2 therefore is indeed the most favourable case with a long scan duration, slow slew rate, night time ranging and still an acceptable distance.

Until now the errors have been given as the standard deviation of the estimated error. However for the requirements and errors as specified by ESA and shown for the pointing budget in Table 5.1 the errors are all mentioned at the 95% confidence level which corresponds to 2 times the standard deviation if the distribution is normal. Figure 8.11 depicts the probability density distribution of the results for the reference case of case 3.2 where the blue bars indicate the results and the line is showing what the ideal normally distribution would be using the standard deviation of 1.67 arcsec. It can be seen that the data is not perfectly normally distributed for the 1000 runs as is expected for a random process, it will never be perfectly distributed. Figure 8.11 is representative for all cases. The mean does converge to zero as was verified in Section 6.3.3 if enough runs are performed. It was found that this figure is representative as long as a reasonable estimation accuracy is possible. At limiting cases where noise is to large or where no pulse detections take place, this figure is not representative but here for the three cases selected enough pulse detections take place and the detection is not background noise limited since all of them are performed at night.

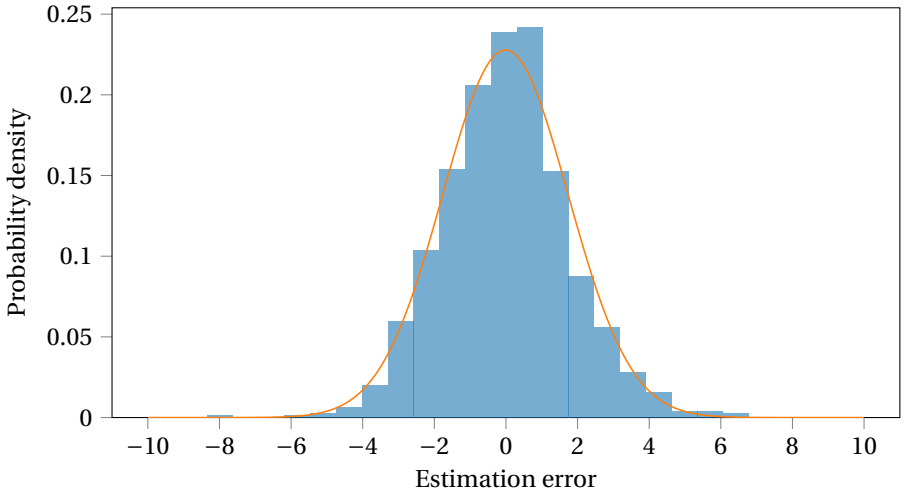

Figure 8.11: Probability density distribution of the estimation error for the reference case 2.3.

A number of things can be said about this distribution summarised in Table 8.5. First of all the standard deviation of this distribution is 1.75 arcsec and if a normal distribution is assumed this would lead to a 2 sigma value of 3.5 arcsec. The distribution shows a minor skewness but more importantly it has a positive value for its kurtosis which is a measure for the number of outliers. A perfect normal distribution with its outliers has a kurtosis of zero, and the higher the number, the less outliers are present. So in terms of error estimation it can be said that not many outliers are present, at least less than is expected from a normal distribution. This is reflected when the 95% level is computed for this distribution which is actually lower at 3.42 compared to the 2 sigma value. Finally a Kolmogorov-Smirnov test was adopted to test the distribution against a true normal distribution and see if the difference is significant or not (Massey, 1951). The probability value of this test is computed to be 0.35 and thus the null hypothesis that this distribution comes from a normal distribution can not be rejected. If it were to be lower than 0.05 it would be rejected. Thus this points in the direction that indeed the distribution found is close to normal. Thus the standard deviation of 1.75 arcsec is a reasonable assumption and the standard deviation of the standard deviation as shown in Table 8.4 as σ_σ is also computed. This is done by a process named bootstrapping where from the given data, a number of random samples are taken of which the standard deviation is calculated again. This is done many times until a statistically significant distribution for the standard deviation is present. This distribution is again found to be normal and the standard deviation of this is 0.064 arcsec which is considered low given the estimation error of 1.75 arcsec. Thus it can be concluded that for the model use here the obtained standard deviation is robust.

Another way to investigate the accuracy of the standard deviation is by looking at the standard deviations of the estimated parameters through the least squares fit of the Gaussian. It was observed that these errors were much smaller than the standard deviations found for the estimation of the ground station position.

Thus the estimation error can not be explained only by the fit. This is because the errors are assumed to be normally distributed with a zero mean. However, the attitude disturbances have a zero mean and are normally distributed over longer periods. When a scan is performed for 10 hours, only some minutes will account for detectable pulses. Therefore a sweep over the ground station will have an error more like a bias, rather than a normally distributed error. Thus the standard deviations of the estimated parameters do not provide a good measure for the estimation error.

Table 8.5: Properties of the error distribution.

	Case 2.3
Standard deviation [arcsec]	1.75
2 sigma [arcsec]	3.50
95% level [arcsec]	3.42
Kurtosis	0.89
Skewness	0.12
P-value of KS-test	0.35
σ_σ [arcsec]	0.064

Now in the worst case the value that can be used with a high level of confidence is the 3.5 arcsec with 0.12 added originating from σ_σ due to the confidence level of this value, resulting in a value of 3.62. This value is the calibration residual in Table 8.6 where the total calibration accuracy is shown. Given the ACKE and AGKE this adds up to an accuracy of 11 arcsec in total. Here the ACKE is actually the governing value for the calibration accuracy determining most of the calibration accuracy.

Table 8.6: Calibration Error.

Contributor	[arcsec]
Spacecraft	
Absolute Control Knowledge Error (ACKE)	10
Absolute Guidance Control Error (AGKE)	2
Calibration residual	3.62
Total Absolute Knowledge Error	
RSS Sum	11

The calibration accuracy depends mostly on the number of detected shots, its distribution and how well the fit can be done on the data. The main assumption here is that the laser shot follows a Gaussian shape. This is a reasonable assumption but in reality this will not be true and the laser pulses will be slightly different. Especially at the edge of the laser pulse the signal will be differently shaped. However the pulse shape of GALA will be extensively measured during calibration efforts on ground Deutsches Zentrum für Luft und Raumfahrt (DLR) (2017). With this new information, a better approximation of the pulse shape can be made over which the data is fitted. Furthermore the commanded attitude knowledge does not look like a Gaussian at all any more but still the estimation performs fairly good. Therefore the accuracy will probably by a bit lower but not significant. Another factor influencing the detected pulses is the weather and clouds which are not modelled in this thesis. When a cloud would appear right at the moment when the ground station would receive pulses, this is bad luck and would highly influence the obtained result. Also other effects of the atmosphere like beam bending and spreading will slightly influence the result by introducing a constant offset which will behave as a constant misalignment. However their influence will be negligible as discussed in Section 3.1. Another constant offset can be caused by the attitude control system. The distribution works best when the disturbance is random. If it is constant, it will behave the same as a constant misalignment and there is no way to tell if it is the misalignment or the control system that will cause this. This could be mitigated by performing the calibration multiple times using different approaches for the attitude control or

by rotating the spacecraft per calibration around the nadir axis but is for now included in the calibration error budget in Table 8.6 as the 10 arcsec ACKE value.

Another shortcoming of the model is that the pulse detection is based on a number of received photons while in reality it will be based on a certain voltage level coming from the APD. For this it is important to know the APD properties and its operation conditions very well and this was not possible for this thesis. When the photoelectrons are converted to a voltage by the APD, amplifier and circuit, some information will be lost and noise is added. Based on the discussions in this thesis, this will influence the calibration mainly in the case of background noise limited detection and laser ranging at a far distance such that the intensities approach the threshold set by the hardware. In these cases it is expected that the calibration will perform worse then in this thesis. However it has been shown that these cases can be avoided by selecting the best options.

8.7. Science return

The final science return does not depend only on the calibration accuracy but also on the other contributions shown again in Table 8.7 including the ACKE, AGKE and thermal stabilities. Here again non calibrated laser altimetry is compared to calibrated laser altimetry. Now the value of 11 arcsec found in Table 8.6 is used, resulting in an pointing error of 20 arcsec. The science return of GALA for the measurement of h_2 is largely governed by Equation 2.3 where the error terms stem from the errors in pointing. In (Steinbrügge et al., 2015), the assumed value for the misalignment, the calibration error was assumed to be 14 arcsec. At 11 arcsec, a better calibration was found in this study. For a calibration error of 14 arcsec, the calibration residual is allowed a maximum of 10 arcsec, almost three times the value found. This corresponds to a value for the standard deviation of 5 arcsec or less and it was shown in the previous sections that this is even possible for the worst case in Table 8.4 and other sections showed that under worse conditions where the slew rate is higher, the number of detected pulses is lower or the false detections are high, it is still possible to reach an error of 5 arcsec and thus the assumption of 14 arcsec is confirmed. For a higher calibration error than 10 arcsec instead of the 3.62 arcsec, the 14 arcsec assumption will not be valid any longer.

Table 8.7: Pointing budget for GALA in Ganymede orbit at 500 km altitude (GCO 500).

Scenario:	No calibration in GCO 500	Calibrated in GCO 500
Contributor	[arcsec]	[arcsec]
Spacecraft		
Absolute Control Knowledge Error (ACKE)	10	10
Absolute Guidance Control Error (AGKE)	20	20
Optical Bench		
Settling	140	-
Alignment Knowledge	14	-
Transceiver Unit		
Settling	6	-
Thermal stability	6	6
Alignment knowledge	14	-
Transmitter		
Settling	6	-
Thermal stability	6	6
Alignment knowledge	12	-
Calibration error	-	11
Total Absolute Knowledge Error		
RSS Sum	144	26

With this error budget and the Ganymede slope statistics (Berquin et al., 2013), Equation 1.3 can be used to to compute the range error δz. This was found to be 5.72 metres in Steinbrügge et al. (2015) with the assumed 14 arcsec alignment error. With a lower 11 arcsec this would result in a range error of around 5.6 metres, a slight improvement. Without any calibration, using the pointing error of 144 arcsec, this would be 30.54 m. All these results are summarised in Table 8.8. Here these three cases are depicted using a smaller version of Table 8.7 with only the AGKE, calibration error and total error. Then a total ranging error is computed as taken from Steinbrügge et al. (2015) where the different pointing errors result in different values for the pointing & alignment contribution which is the range error δz as just discussed. It has to be noted that in the pointing error budget assumed by Steinbrügge et al. (2015), the thermal stabilities were not taken into account. This why the difference between the total pointing errors of 27 and 26 arcsec is only 1 arcsec although the calibration accuracies are 11 and 14 arcsec.

It can be seen that indeed the influence of the calibration brings down the un-calibrated pointing error δz of 30 metres to 5.72 metres as found in Steinbrügge et al. (2015). With a slight improvement to 5.58 m with the calibration error of 11 arcsec found in this thesis. It can be seen that the final pointing error in Table 8.7 is now mainly driven by the AGKE originating from the orbit determination, which is why it is included in Table 8.8. It is expected that the orbit determination accuracy will become better and decrease to 15 or 10 arcsec through the PRIDE experiment European Space Agency (ESA) (2014). In that case the calibration error will be at the same level or become the largest error, largely governing the total error when the root sum square is taken. Therefore this calibration accuracy will be very beneficial for the final range error δz. This flows down even further into the total mean range error of the cross-over measurements below in Table 8.8 where also the instrument error, interpolation error and other errors are taken into account (Steinbrügge et al., 2015). While the range error is in the order of 5 metres, the others do not exceed 2 metres and thus again, the range error is largely governing the total error (Steinbrügge et al., 2015).

Table 8.8: Total error budget for GALA as in Steinbrügge et al. (2015) for different pointing errors.

Cases:	No calibration	Assumed in (Steinbrügge et al., 2015)	Best calibration	Improved orbit determination
Pointing Errors	Value [arcsec]	Value [arcsec]	Value [arcsec]	Value [arcsec]
AGKE	20	20	20	10
Calibration Error	-	14	11	11
Total Error	144	27	26	20
Ranging error	Mean value [m]	Mean value [m]	Mean value [m]	Mean value [m]
Pointing & alignment (δz)	30.54	5.72	5.58	4.2
Instrument, interpolation and others	4.85	4.85	4.85	4.85
Total mean range error	30.67	6.38	6.25	5.06

The total mean error is computed to be 6.38 metres by Steinbrügge et al. (2015) with its assumptions and thus this would drop to around 6.25 metres with the slight improvement in the range error to 5.58 metres. With a decrease of the orbit error to 10 arcsec and the 11 arcsec the total mean range error would further drop to 5 metres. Now for the final measurement of h_2 also the distribution and the total amount of cross-over measurements largely influences the accuracy of the measurement of h_2. The error in the estimate for h_2 was found to be 0.026 for the mean range error of 6.38 m in Steinbrügge et al. (2015). This would improve to 0.021 if all other errors remain the same. This is a total error of 2% and 1.6% respectively when assuming h_2 is 1.3 and this accuracy was found to be sufficient for the final goal of GALA, confirming the existence of an ocean underneath Ganymede' ice shell, and constrain its thickness (Steinbrügge et al., 2015). Thus the calibration is an important part for the science mission of GALA and ultimately JUICE given the improvement of an total mean range error of 30.67 m to 6.38 m. Together with other experiments and a calibrated GALA, JUICE might be able to draw conclusions on the thickness of the ice shell and the ocean underneath.

9

Conclusions and Recommendations

Together with the discussion on the validation of the model, the trajectory analysis and the various results presented throughout this thesis, this chapter aims to answer the questions posed for this thesis. This is done in Section 9.1 where each of the objectives is discussed and a final answer to the main question is given. Scientific research never ends and no model is deemed perfect. Therefore Section 9.2 provides some recommendations on how to improve the model and progress further in this subject. Finally Section 9.2.1 elaborates on the next step for the development of GALA.

9.1. Conclusion

The calibration of GALA through laser ranging to Earth based ground stations has been the focus of this thesis and through the investigation and selection of a concept for the laser ranging and analysing its performance the main objective has been accomplished leading to an answer for the main question posed:

How can interplanetary laser ranging to an Earth based ground station be used to calibrate the alignment of the GALA laser altimeter?

The answer to this question lies in the four objectives set at the beginning of this thesis in Section 1.2, answering the sub questions posed will lead to the answer to the main question. The sub objectives will first be treated before arriving to an answer for the main question at hand.

1 Select a representative laser ranging opportunity.

The first goal of this thesis was to select a laser ranging opportunity from the trajectory of JUICE to Jupiter in Chapter 7. Three constraints were set; the angular separation for the angle between JUICE and the Sun as seen from Earth, the angular separation between Sun and Earth as seen from JUICE and the Sun pointing of the HGA below a distance to the Sun of 1.3 AU. Three cases were set up; 1. near Earth flybys, 2. HGA remain Sun pointing and 3. Distance to the Sun greater than 1.3 AU. These options were thoroughly analysed and using the model established in Chapter 3 for the received signal and noise intensities, it was possible to select options that are optimal for laser raging. Given in Table 9.1 are the two options that represent the reference case that was used throughout this study and the option with the highest calibration accuracy found in Section 8.6. The reference case was used because of its medium range compared to other options, and the fact that the Sun is rising when longer laser ranging is performed. This causes solar noise and therefore it was also possible to assess this impact. From Section 7.5.4 it can be concluded that option 1.3 at 0.38 AU is not only the best option but is also very representative in the fact that there are no operational limitations in terms of time and duration. One can do the same laser ranging again in 1 or 2 weeks or even months later and thus this serves as an ideal case for the laser ranging during the real mission.

2 Develop and simulate a laser ranging campaign calibrating the misalignment and identify its main characteristics.

This objective required the investigation of how to calibrate a laser altimeter for its misalignment and what is important to be able to do this successfully. A closer look was taken at GALA, ground stations, the calibration

Table 9.1: Representative laser ranging options.

Property	Value	
Case identifier	2.3 (reference case)	1.3
Mean range	33501982 km (0.23 AU)	57191391 km (0.38 AU)
Start time	2024 OCT 17 02:00:00	2024 DEC 21 21:00:00
Stop time	2024 OCT 17 06:00:00	2024 DEC 22 07:00:00
Mean elevation of JUICE	55 deg	70 deg
Duration	4 hours	10 hours

of laser altimeters and laser ranging itself. After this it was investigated what is causing the misalignment producing the pointing budget as a result in Section 5.1. From this budget it can be concluded that the window to be scanned for laser ranging is -333 to +333 arcsec taking into account the 3-sigma confidence level, which is an important input for the development of the calibration. Furthermore the calibration is expected to bring down the total pointing error from 144 to 28 arcsec.

It also became clear that it was required to model the attitude behaviour of JUICE since the pointing error from the spacecraft alone is already 15 arcsec which is higher than the calibration error aimed for at 10 arcsec or better. Section 5.1.3 concluded that the RPE's were to be taken into account to model the random behaviour of the attitude and two different models were created in Section 5.2. From Section 8.2 it can be concluded that these models perform as expected and that indeed one model provides a worst case scenario where it is no longer possible to distinguish the intended scan pattern. Instead the pulses become spread out in a random manner governed by the APE of 15 arcsec and the RPE's.

A simulation was set up in Section 6.1 where the developed scan pattern, attitude models and scan window produce a distribution of laser pulses with their received intensities at the ground station. From here an estimation procedure for the ground station position was developed in Section 6.2. The idea is to use the spatial distribution of the pulses to reconstruct the spatial Gaussian pulse shape and locate the position of the ground station which lies at at the peak intensity of the found Gausian pulse shape. At first this was done using the photon intensities but it was concluded that is unlikely that this data will be available when the actual experiment is performed. Therefore, also a procedure was developed using only pulse detections and their distributions and Section 8.2 showed that this performs even slightly better. Section 6.3 verified that this procedure is robust and can be used to run many simulations and obtain statistical significant results. In the ideal case where the attitude knowledge is perfect it is concluded that the standard deviation of the estimation error is below 0.1 arcsec. This changes to 1.52 to 8 arcsec when attitude errors are introduced due to the degraded attitude knowledge of the laser pulses caused by the limited attitude knowledge of the spacecraft.

A qualitative validation was done in Section 6.4 using the Hayabusa and MLA experiments to see how well the model developed could predict the results found in those experiments. It was found that the model predicts around 3 times more detectable shots than were received during the actual experiments for MLA. Here more than 120 shots should be detected but only 24 were received. This can partly be explained by the cloud cover present during the experiment but also shows that the model is susceptible to less parameters than in real life are present. Given so many unknown parameters for laser ranging in a real experiment, the model is able to predict if detection is possible and make a qualitative assessment on this.

However, much more shots are required than 24 or 120 to make an acceptable estimation of the ground station as Chapter 8 concluded that 500 - 1000 is the number of pulse detections required for a proper estimate. This is however more achievable than one thinks when looking at the low 24 detections for MLA. The larger number of detected pulses will be achieved by the long scanning duration available for JUICE and the much higher frequency at which the shots are fired. This is 30 Hz for GALA and was only 8 Hz for MLA. Furthermore, for MLA only 3 sweeps were detectable whereas for GALA around 40 sweeps will be detectable. Also the scanning window is smaller for GALA, supporting the conclusion that far more shots are available for detection for GALA. In the Hayabusa experiment, no laser pulses were detected at all. The model was also able to predict this low probability that the Hayabusa experiment would detect any shots at all, supporting the conclusion that the model developed in this thesis can make a good qualitative assessment of a laser ranging calibration experiment.

Since the calibration procedure is based on the spatial distribution of detected pulses it was concluded that the main characteristics influencing the calibration are properties of the laser ranging that influence this distribution. It was found the attitude models, the slew rate, the threshold and the distance are the main

drivers for the calibration accuracy.

3 Investigate the performance of the calibration.

In Section 5.1.2 the pointing budget was established from which it can be concluded that the calibration accuracy, the 2-sigma standard deviation, should not be greater than 10 arcsec. Throughout Chapter 8 this number was not violated and it can thus be concluded that indeed a successful calibration can be performed. Section 8.3 showed that the slew rate could be varied from 0.017 to 0.0035 deg/sec where a worst estimation error of 4 arcsec was found. The effect of a high slew rate was less worse than the effect of setting a high detection threshold in Section 8.4 for night time ranging. For a high threshold at 500 photoelectrons a maximum error of 6 - 8 arcsec was found, where the 6 arcsec was established based on roughly the same amount of detections as the 4 arcsec for the high slew rate. Thus it can be concluded that the threshold is a very important setting, which is confirmed by the analysis for day time ranging. Here a large difference was found in the calibration accuracy when changing the threshold from 8 to 11 photoelectrons. Whereas the calibration accuracy is 2 arcsec up to high Sun elevations for a threshold of 11, this quickly degrades to 10 arcsec or higher for a threshold of 9 or 8 photoelectrons. This confirms the influence of the capabilities of the ground station, which is an input for the model that is difficult to determine. Various ground stations have various characteristics and employ different equipment such as the APD. This APD then can have various settings, changing its behaviour dramatically and unfortunately it was not possible to develop a sufficient model for this since the conditions of the APD and the electronics used at the ground station are highly variable and unknown in 10 years time. Thus a threshold detection was the most suitable option to detect shots as established in Section 3.5.

Ground stations also influence the distance at which laser ranging is possible. The maximum distance found among all options in the trajectory analysis in Section 7.5 is found to be 2 AU, which is precisely at the border of the capabilities of the ground station as specified for the reference case in Section 8.1. Section 8.5 concluded that here it becomes difficult to make a proper conclusion about the estimation accuracy in this case, since so many input parameters and properties are not accurate enough any more. Section 8.5 showed that with a telescope diameter of 0.75 m, most pulses would have an intensity of 2-6 photons. Just by choosing a different ground station such as Grasse, with double the aperture diameter, the intensity would also almost double. Since the photon intensities lie close to the required threshold to suppress the dark noise it is difficult to make a quantitative conclusion about this case. However here it is also shown that for distances for the proposed options in Section 7.5, an calibration accuracy of 2 to 3 arcsec can be achieved for a distance no greater than 0.5 AU.

From the discussion in Section 8.6 on the distribution of the estimation errors over many simulations it can be concluded that the standard deviation found is indeed a statistical significant result. Here it was shown that the standard deviation is a robust value and can be used to discuss the final calibration accuracy. The three optimal cases selected in Section 7.5.4 were simulated using the different cases for the ground station properties from Section 8.1. The best case was found to be case 1.2 were laser ranging can be performed for 10 hours at a distance of 0.39 AU. From this it can be concluded that the distribution of shots is indeed more important than the intensity governed by the distance. This can be explained by the fact that for reasonable distances up to 0.5 AU, a smaller distance resulting in higher photon intensities, will only produce more detected shots at the border of the Gaussian pulse shape. This does not provide much more information on the peak intensity of the Gaussian since these shots were already detectable if a larger distance was used. This is confirmed by the calibration error for case 3.1 at 4.5 arcsec, which is done at 6 million km only, but because of the 1 hour duration produces far worse results. Finally it can be concluded that using the 3.62 arcsec calibration residual, the calibration error is 11 arcsec, slightly better than the 14 arcsec assumed in Steinbrügge et al. (2015) and that thus this assumption is valid.

4 Investigate the improvement of the science performance of GALA

The science performance and the improvement of it were discussed in Section 8.7. Here the contribution of the pointing error for the range error was found to be 30 metres for the calibrated case with a pointing error of 144 arcsec. Compared to 5.7 metres for the calibrated case this is a large improvement enabling successful science for GALA which would not be possible in the calibrated case. Is confirmed that with this estimation procedure the science performance can indeed be as good as presented in Steinbrügge et al. (2015) and it was determined that it could improve a bit in terms of measurement accuracy of h_2 through better calibration. The range error could decrease to 5 meters if the orbit determination would improve as suggested in Section

8.7 and this would help the estimate of h_2 even more. Thus it is confirmed that the assumptions made on the calibration error in Steinbrügge et al. (2015) are correct and supported by the work in this thesis and could even improve.

Looking at the various conclusions from the different objectives, it is possible to answer to the main question that interplanetary laser ranging can be used to calibrate GALA by employing 8-10 hours of scanning at a distance no further than around 0.5 AU by using ground station characteristics such as found at Wettzell with a telescope diameter of 0.75 metres and optical and quantum efficiencies of 0.5 and 0.2 respectively. At these distances it can be concluded that if around 500 - 1000 shots are detected, it is possible to make an estimation of the ground station with acceptable accuracy. This thesis confirms that this number of detected pulses is considered realistic given the long scanning durations, slow slew rates and high shot frequency. The work in this thesis also supports the assumption that through calibration as developed here, the envisioned science performance of GALA can be achieved and might even improve it.

9.2. Recommendations

Throughout this study several new aspects were found and some were to big too take on in the amount of time available. New questions arose and opportunities for improvement for this study have been discovered. A separation can be made in the recommendations, first possible improvements of the model will be given that were found throughout this study. However, this study is part of a greater process in developing a space mission to Jupiter, therefore also some recommendations and outlooks will be given towards this goal that will become part of the development plan for GALA as will be carried out the next 5 years.

It was concluded that the calibration accuracy showed a large dependence on the attitude model used. As the development of JUICE will progress, better models for the attitude and its errors will become available. It is therefore recommended to implement these more and more advancing models into the simulation. With these advances also more established ideas about how JUICE will operate will become available. For example in building the sweep scan pattern, it is assumed that it is possible to jump from one sweep line to the next in just one shot. However, in reality this will take some time. Also a spacecraft takes some time to achieve a certain slew rate and attitude required for a given sweep line. This is not modelled but when attitude models become available it can be incorporated in the simulation. Then the attitude would first be simulated trough the more advance attitude simulation before it is processed into the simulation developed here to produce pulse distributions and intensities. This will make the simulation more realistic, possibly reducing the scanning time available. It is expected however that the final accuracy will not vary greatly since in this model already the shots are very randomly distributed when passing over the ground station.

Another improvement can be made with regards to the pulse and false detections. If a statistical method such as proposed in Ricklefs and Shelus (1993) would be developed to filter out false detections, one could lower the threshold and accept much more false detections, leading also to more pulse detections. It was already shown that more pulse detections lead to a better estimation accuracy. Basically this improvement would add temporal filtering after which the developed estimation is done on the spatial distribution of the shots. This would lead to improved accuracy, especially when laser ranging is background noise limited, as is the case for day time ranging. For night time ranging this would mean that the threshold could be set even lower and more data is available even at greater distance. GALA itself employs very different algorithms to detect pulses by analysing the shape of the entire signal and such an algorithm can also be employed in this case, where pulse detection does not take place using a threshold, but by analysing the digitised return from the APD.

The laser pulse profile will and can be measured on ground during testing. This will make information on the spatial pulse shape available and this can be incorporated in the calibration procedure. Then the estimation algorithm can try to fit this pulse shape instead of the perfect Gaussian shape to make the ground station position estimation even more accurate and realistic.

The next step in the theoretical investigation of the laser ranging is to extend the study to incorporate timing of the shots. So far the focus was on the spatial distribution of shots and by simulating also time, the temporal effects can be analysed. Then one could also simulate a more precise concept for the detection using range gates, whereas now a continuous operation of the APD is assumed. This can extend the entire laser ranging campaign towards not only the goal of calibrating GALA, but also do range measurements and breaking the record for distance at which a laser link is established. A prediction can be made on what accu-

racies can be achieved and focus more on the science case for an interplanetary laser link itself, rather than on the science case for the calibration of GALA.

9.2.1. Towards a full scale test

The next step in the development process of GALA will be involving hardware. During a visit to Wettzell (Schreiber, 2017), already the plan to install GALA on the available telescope as depicted in Figure 9.1 was discussed and also employed for the development of BELA (Schreiber et al., 2009). This could be used to do real world verification of the received photon intensities in the model. The idea is to aim GALA at a satellite or laser retro reflector and see what is received back of the signal. The distance can be simulated by using a satellite at a certain distance and with a certain area, mimicking the signal strength of a laser beam over a large distance. The laser sent out by GALA is then received back at the ground station and thus the signal intensities can be verified by comparing the received intensities with the simulated intensities found in this thesis.

Figure 9.1: BELA mounted on the telescope at the Wettzell ground station in south Germany (Schreiber et al., 2009)

This also gives opportunity to test asynchronous laser ranging with GALA and the laser at Wettzell, proving and testing the concept realistically, serving as a validation of the concept proposed in this study. Finally detection schemes can be tested and pulse detection algorithms can be tested using real data. So no longer there will be a need to simulate noise but one can use real measured noise and use this in further simulations or calibrate the models used here. The only thing not achievable is to test the attitude of spacecraft during a scan, as in this experiment, GALA and the telescope will be co-aligned and thus every pulse sent is also received. However, this can already be improved by using models from ESA and Airbus as was discussed before.

Bibliography

Abshire, J. B., Sun, X., and Afzal, R. S. (2000). Mars orbiter laser altimeter: receiver model and performance analysis. *Applied optics*, 39(15):2449–2460.

Airbus Defence and Space (2016). Airbus Defence and Space JUICE spacecraft. http://space.airbus.com/portfolio/space-exploration/juice-searching-for-life-on-jupiters-icy-moons/. Accessed: 2017-07-24.

Althaus, C. and Stark, A. (2017). Instrument Calibration Plan JUI-DLRP-GAL-PL-18002. Technical report, Deutsches Zentrum für Luft und Raumfahrt (DLR), Berlin.

Belton, M. J. S., Head, J. W., Ingersoll, A. P., Greeley, R., McEwen, A. S., Klaasen, K. P., Senske, D., Pappalardo, R., Collins, G., Vasavada, A. R., Sullivan, R., Simonelli, D., Geissler, P., Carr, M. H., Davies, M. E., Veverka, J., Gierasch, P. J., Banfield, D., Bell, M., Chapman, C. R., Anger, C., Greenberg, R., Neukum, G., Pilcher, C. B., Beebe, R. F., Burns, J. A., Fanale, F., Ip, W., Johnson, T. V., Morrison, D., Moore, J., Orton, G. S., Thomas, P., and West, R. A. (1996). Galileo's First Images of Jupiter and the Galilean Satellites. *Science*, 274(5286).

Bender, P. L., Currie, D. G., Poultney, S. K., Alley, C. O., Dicke, R. H., Wilkinson, D. T., Eckhardt, D. H., Faller, J. E., Kaula, W. M., Mulholland, J. D., Plotkin, H. H., Silverberg, E. C., and Williams, J. G. (1973). The Lunar Laser Ranging Experiment. *Science (New York, N.Y.)*, 182(4109):229–38.

Berquin, Y., Kofman, W., Herique, A., Alberti, G., and Beck, P. (2013). A study on Ganymede's surface topography: Perspectives for radar sounding. *Planetary and Space Science*, 77:40–44.

Bignami, G., Cargill, P., Schutz, B., Turon, C., Wilson, A., and Perel, J. (2005). Cosmic Vision: Space Science for Europe 2015-2025. Technical report, European Space Agency, Noordwijk.

Boutonnet, A. and Varga, G. (2016). JUICE - Jupiter Icy moons Explorer Consolidated Report on Mission Analysis (CReMA) JUI-ESOC-MOC-RP-001. Technical report, European Space Operations Centre, Darmstadt.

Cavanaugh, J. F., Smith, J. C., Sun, X., Bartels, A. E., Ramos-Izquierdo, L., Krebs, D. J., McGarry, J. F., Trunzo, R., Novo-Gradac, A. M., Britt, J. L., Karsh, J., Katz, R. B., Lukemire, A. T., Szymkiewicz, R., Berry, D. L., Swinski, J. P., Neumann, G. A., Zuber, M. T., and Smith, D. E. (2007). The Mercury Laser Altimeter Instrument for the MESSENGER Mission. *Space Science Reviews*, 131(1-4):451–479.

Collins, G. and Johnson, T. V. (2014). Ganymede and Callisto. In Spohn, T., Breuer, D., and Johnson, T. V., editors, *Encyclopedia of the Solar System*, chapter 37, pages 813–829. Elsevier.

Coyle, D. B., Skillman, D., Steigelman, J., Cavanaugh, J. F., Neumann, G. A., and Sun, X. (2006). The 24 Million Kilometer Optical Link with the Mercury Laser Altimeter. In *The Second ESA-NASA Working Meeting on Optoelectronics: Qualifications of Technologies and Lessons Learned from Satellite LIDAR and Altimeter Missions*, Noordwijk.

Degnan, J. J. (1993). Millimeter Accuracy Satellite Laser Ranging: A Review. *Contributions of Space Geodesy to Geodynamics: Technology*, 25:31.

Degnan, J. J. (2001). Unified Approach to Photon-counting Microlaser Rangers, Transponders and Altimeters. *Surveys in Geophysics*, 22(5):431–447.

Degnan, J. J. (2002a). Asynchronous laser transponders for precise interplanetary ranging and time transfer. *Journal of Geodynamics*, 34(3):551–594.

Degnan, J. J. (2002b). Photon-counting multikilohertz microlaser altimeters for airborne and spaceborne topographic measurements. *Journal of Geodynamics*, 34:503–549.

Deutsches Zentrum für Luft und Raumfahrt (DLR) (2017). Experiment Interface Document - Part B JUI-DLRP-GALA-EID-10002. Technical report, DLR, Berlin.

Dirkx, D., Noomen, R., Prochazka, I., Bauer, S., and Vermeersen, L. (2014a). Influence of atmospheric turbulence on planetary transceiver laser ranging. *Advances in Space Research*, 54(11):2349–2370.

Dirkx, D., Noomen, R., Visser, P., Bauer, S., and Vermeersen, L. (2015). Comparative analysis of one- and two-way planetary laser ranging concepts. *Planetary and Space Science*, 117:159–176.

Dirkx, D., Vermeersen, L., Noomen, R., and Visser, P. (2014b). Phobos laser ranging: Numerical Geodesy experiments for Martian system science. *Planetary and Space Science*, 99:84–102.

Dougherty, M. (2011). JUICE: exploring the emergence of habitable worlds around gas giants. Assessment Study Report. Technical Report December, European Space Agency.

European Space Agency (ESA) (2008). Space Engineering Control Performance ECSS-E-ST-60-10C. Technical Report November, European Space Agency, Noordwijk.

European Space Agency (ESA) (2011). ESA pointing error engineering handbook ESSB-HB-E-003. Technical report, European Space Agency.

European Space Agency (ESA) (2014). JUpiter ICy moons Explorer Exploring the emergence of habitable worlds around gas giants. Definition Study Report. Technical Report September, European Space Agency.

European Space Agency (ESA) (2017). JUICE Experiment Interface Document - Part A. JUI-EST-SYS-EID-001. Technical report, ESA, Noordwijk.

Gardner, C. S. (1992). Ranging performance of satellite laser altimeters. *IEEE Transactions on Geoscience and Remote Sensing*, 30(5):1061–1072.

Grasset, O., Dougherty, M. K., Coustenis, A., Bunce, E. J., Erd, C., Titov, D., Blanc, M., Coates, A., Drossart, P., Fletcher, L. N., Hussmann, H., Jaumann, R., Krupp, N., Lebreton, J. P., Prieto-Ballesteros, O., Tortora, P., Tosi, F., and Van Hoolst, T. (2013). JUpiter ICy moons Explorer (JUICE): An ESA mission to orbit Ganymede and to characterise the Jupiter system. *Planetary and Space Science*, 78:1–21.

Gunderson, K., Thomas, N., and Rohner, M. (2006). A Laser Altimeter Performance Model and Its Application to BELA. *IEEE Transactions on Geoscience and Remote Sensing*, 44(11):3308–3319.

Gurtner, W., Noomen, R., and Pearlman, M. (2005). The International Laser Ranging Service: current status and future developments. *Advances in Space Research*, 36(3):327–332.

Hussmann, H., Lingenauber, K., Oberst, J., Kobayashi, M., Namiki, N., Kimura, J., Thomas, N., Lara, L., and Steinbrügge, G. (2014). The Ganymede Laser Altimeter (GALA). *European Planetary Science Congress*, 9(EPSC2014-347):2.

Hussmann, H., Sohl, F., and Oberst, J. (2011). Measuring tidal deformations at Europa's surface. *Advances in Space Research*, 48(4):718–724.

Hussmann, H., Sotin, C., and Lunine, J. (2015). Interiors and Evolution of Icy Satellites. In *Treatise on Geophysics*, chapter 10.18, pages 605–635. Elsevier.

Hussmann H, Sohl, F., and Spohn, T. (2006). Subsurface oceans and deep interiors of medium-sized outer planet satellites and large trans-neptunian objects. *Icarus*, 185(1):258–273.

IDEX Optics and Photonics (2016). Gaussian Beam Propagation.

IRLS (2017). ILRS | Network | List of Stations | Active Stations | STL3 Site Log. https://ilrs.cddis.eosdis.nasa.gov/network/stations/active/STL3{_}sitelog.html{#}6.ReceiverSystem. Accessed: 2017-06-09.

Japan Aerospace Exploration Agency (JAXA) (2017). Hayabusa Project Science Data Archive : JAXA, SPICE. https://darts.isas.jaxa.jp/planet/project/hayabusa/spice.html. Accessed: 2017-06-10.

Jie, S. and Toth, C. K. (2008). *Topographic Laser Ranging and Scanning: Principles and Processing*. CRC Press.

Kasting, J. F., Whitmire, D. P., and Reynolds, R. T. (1993). Habitable Zones around Main Sequence Stars. *Icarus*, 101(1):108–128.

Kivelson, M. G., Khurana, K. K., Russell, C. T., Walker, R. J., Warnecke, J., Coroniti, F. V., Polanskey, C., Southwood, D. J., and Schubert, G. (1996). Discovery of Ganymede's magnetic field by the Galileo spacecraft. *Nature*, 384(6609):537–541.

Kivelson, M. G., Khurana, K. K., and Volwerk, M. (2002). The Permanent and Inductive Magnetic Moments of Ganymede. *Icarus*, 157:507–522.

Laser Components (2016). Silicon Geiger Mode Avalanche Photodiode SAP500-Series Datasheet. Technical report, Laser Components.

Laser Components (2017). Silicon Avalanche Photodiode SAR1500x/SAR3000x Datasheet. Technical report, Laser Components.

Lebreton, J.-P., Witasse, O., Sollazzo, C., Blancquaert, T., Couzin, P., Schipper, A.-M., Jones, J. B., Matson, D. L., Gurvits, L. I., Atkinson, D. H., Kazeminejad, B., and Pérez-Ayúcar, M. (2005). An overview of the descent and landing of the Huygens probe on Titan. *Nature*, 438(8):758–764.

Lingenauber, K., Hussmann, H., Michaelis, H., Oberst, J., Kobayashi, M., Namiki, N., Thomas, N., Seiferlin, K., and Lara, L. M. (2013). The Ganymede Laser Altimeter (GALA) on ESA's JUICE mission: Overview of the instrument design. In *International Workshop on Instrumentation for Planetary Missions*.

Lingenauber, K., Hussmann, H., Michaelis, H., Oberst, J., Kobayashi, M., Namiki, N., Thomas, N., Seiferlin, K., and Lara, L. M. (2014). The Ganymede Laser Altimeter (GALA) on ESA's JUICE mission: Overview of the instrument design. In *International Workshop on Instrumentation for Planetary Missions*, pages 1–19. DLR.

Lisano, M. E. and Schiutz, B. E. (2001). Arcsecond-level pointing calibration for ICESat laser altimetry of ice sheets. *Journal of Geodesy*, 75:99–108.

Love, A. E. H. (1911). *Some Problems of Geodynamics*. Cambridge University Press, Cambridge.

Lu, H., Zhao, W., and Xie, X. (2012). Analysis of temporal broadening of optical pulses by atmospheric dispersion in laser communication system. *Optics Communications*, 285(13-14):3169–3173.

Luthcke, S. B., Rowlands, D. D., McCarthy, J. J., Pavlis, D. E., Stoneking, E., Goddard, N., and Flight, S. (2000). Spaceborne Laser-Altimeter-Pointing Bias Calibration from Range Residual Analysis. *Journal of Spacecraft and Rockets*, 37(3):374–384.

Magruder, L., Silverberg, E., Webb, C., and Schutz, B. (2005). In situ timing and pointing verification of the ICESat altimeter using a ground-based system. *Geophysical Research Letters*, 32(21):L21S04.

Magruder, L. A., Schutz, B. E., and Silverberg, E. C. (2003). Laser pointing angle and time of measurement verification of the ICESat laser altimeter using a ground-based electro-optical detection system. *Journal of Geodesy*, 77(3-4):148–154.

Marini, J. W. and Murray, C. W., J. (1973). Correction of laser range tracking data for atmospheric refraction at elevations above 10 degrees. Technical report, NASA Goddard Space Flight Center.

Massey, F. J. (1951). The Kolmogorov-Smirnov Test for Goodness of Fit. *Journal of the American Statistical Association*, 46(253):68–78.

Mauk, B. H., Mitchell, D. G., McEntire, R. W., Paranicas, C. P., Roelof, E. C., Williams, D. J., Krimigis, S. M., and Lagg, A. (2004). Energetic ion characteristics and neutral gas interactions in Jupiter's magnetosphere. *Journal of Geophysical Research*, 109(A9):A09S12.

Mendes, V. B. and Pavlis, E. C. (2004). High-accuracy zenith delay prediction at optical wavelengths. *Geophysical Research Letters*, 31(14):L14602.

Mizuno, T., Kase, T., Shiina, T., Mita, M., Namiki, N., Senshu, H., Yamada, R., Noda, H., Kunimori, H., Hirata, N., Terui, F., and Mimasu, Y. (2016). Development of the Laser Altimeter (LIDAR) for Hayabusa 2. *Space Science Reviews*, pages 1–15.

Moore, W. B. and Schubert, G. (2003). The tidal response of Ganymede and Callisto with and without liquid water oceans. *Icarus*, 166(1):223–226.

Moré, J. J. (1978). The Levenberg-Marquardt algorithm: Implementation and theory. In *Conference on numerical analysis*, pages 105–116, Dundee, UK.

Murphy, T. (2001). Statistics of Photon Arrival Time. Technical report, Center for Astrophysics and Space Sciences (CASS).

NASA/JPL (1998). PIA00716: Ganymede Color Global. http://photojournal.jpl.nasa.gov/catalog/PIA00716.

Navigation and Ancillary Information Facility (NAIF) (2012). NAIF PDS SPICE Archives MESSENGER. https://naif.jpl.nasa.gov/pub/naif/pds/data/mess-e{_}v{_}h-spice-6-v1.0/messsp{_}1000/. Accessed: 2017-06-10.

Navigation and Ancillary Information Facility (NAIF) (2017). SPICE Toolkit. https://naif.jpl.nasa.gov/naif/toolkit.html. Accessed: 2017-07-22.

Noda, H., Kunimori, H., Mizuno, T., Senshu, H., Ogawa, N., Takeuchi, H., Moore, C., Pollard, A., Yamaguchi, T., Namiki, N., Kase, T., Saiki, T., and Tsuda, Y. (2017). Laser link experiment with the Hayabusa2 laser altimeter for in-flight alignment measurement. *Earth, Planets and Space*, 69(2).

Noda, H., Mizuno, T., Kunimori, H., Takeuchi, H., and Namiki, N. (2013). Alignment measurement with optical transponder system of Hayabusa-2 LIDAR. In *18th International Workshop on Laser Ranging*, Fujiyoshida.

Noda, H., Mizuno, T., Kunimori, H., Takeuchi, H., Senshu, H., Ogawa, N., Saiki, T., Yamaguchi, T., Pollard, A., Moore, C., Namiki, N., and Tsuda, Y. (2016). Establishment of Laser Link between Ground Station and Hayabusa 2 LIDAR. *Lunar and Planetary Science Conference*, 47.

Oberst, J., Lainey, V., Poncin-Lafitte, C. L., Dehant, V., Rosenblatt, P., Ulamec, S., Biele, J., Spurmann, J., Kahle, R., Klein, V., Schreiber, U., Schlicht, A., Rambaux, N., Laurent, P., Noyelles, B., Foulon, B., Zakharov, A., Gurvits, L., Uchaev, D., Murchie, S., Reed, C., Turyshev, S. G., Gil, J., Graziano, M., Willner, K., Wickhusen, K., Pasewaldt, A., Wählisch, M., and Hoffmann, H. (2012). GETEMME—a mission to explore the Martian satellites and the fundamentals of solar system physics. *Experimental Astronomy*, 34(2):243–271.

Pappalardo, R. T., Head, J. W., Collins, G. C., Kirk, R. L., Neukum, G., Oberst, J., Giese, B., Greeley, R., Chapman, C. R., Helfenstein, P., Moore, J. M., McEwen, A., Tufts, B., Senske, D. A., Breneman, H., and Klaasen, K. (1998). Grooved Terrain on Ganymede: First Results from Galileo High-Resolution Imaging. *Icarus*, 135(1):276–302.

Pearlman ', M. R., Degnar, J. J., and Bosworth2, J. M. (2002). The International Laser Ranging Service. *Adv. Space Res*, 30(2):13–143.

Perkin Elmer (2003). Avalanche Photodiodes: A User's Guide. Technical report, Perkin Elmer.

Princeton Lightwave (2010). PGA-200 Cooled Single Photon Counting Avalanche Photodiode. Technical report, Princeton Lightwave, Inc., Cranbury.

Princeton Lightwave (2017). PGA Series Single Photon Counting Avalanche Photodiodes. Technical report, Princeton Lightwave, Inc., Cranbury.

Prockter, L. M., Figueredo, P. H., Pappalardo, R. T., Head, J. W., and Collins, G. C. (2000). Geology and mapping of dark terrain on Ganymede and implications for grooved terrain formation. *Journal of Geophysical Research: Planets*, 105(E9):22519–22540.

Prockter, L. M., Head, J. W., Pappalardo, R. T., Senske, D. A., Neukum, G., Wagner, R., Wolf, U., Oberst, J. O., Giese, B., Moore, J. M., Chapman, C. R., Helfenstein, P., Greeley, R., Breneman, H., and Belton, M. J. (1998). Dark Terrain on Ganymede: Geological Mapping and Interpretation of Galileo Regio at High Resolution. *Icarus*, 135(1):317–344.

Prockter, L. M., Lopes, R. M. C., Giese, B., Jaumann, R., Lorenz, R. D., Pappalardo, R. T., Patterson, G. W., Thomas, P. C., Turtle, E. P., and Wagner, R. J. (2010). Characteristics of icy surfaces. *Space Science Reviews*, 153(1-4):63–111.

Renker, D. (2006). Geiger-mode avalanche photodiodes, history, properties and problems. *Nuclear Instruments and Methods in Physics Research Section A: Accelerators, Spectrometers, Detectors and Associated Equipment*, 567(1):48–56.

Ricklefs, R. L. and Shelus, P. J. (1993). Poisson filtering of laser ranging data. In *Eighth International Workshop on Laser Ranging Instrumentation*, page 7, Austin, TX, United States.

Riris, H., Cavanaugh, J., and Neumann, G. (2010). Calibration Document for the Lunar Orbiter Laser Altimeter (LOLA) Instrument. Technical report, Goddard Space Flight Center, Greenbelt, Maryland.

Rowlands, D. D., Carabajal, C. C., Luthcke, S. B., Harding, D. J., Sauber, J. M., and Bufton, J. L. (2000). Satellite Laser Altimetry. On-Orbit Calibration Techniques for Precise Geolocation. *The Review of Laser Engineering*, 28(January 2000):796–803.

Saur, J., Duling, S., Roth, L., Jia, X., Strobel, D. F., Feldman, P. D., Christensen, U. R., Retherford, K. D., McGrath, M. A., Musacchio, F., Wennmacher, A., Neubauer, F. M., Simon, S., and Hartkorn, O. (2015). The search for a subsurface ocean in Ganymede with Hubble Space Telescope observations of its auroral ovals. *Journal of Geophysical Research: Space Physics*, 120(3):1715–1737.

Schreiber, K., Hiener, M., Holzapfel, B., Michaelis, H., Brandl, N., Haufe, K.-H., Lauber, P., and Neidhardt, A. (2009). Altimetry and transponder ground simulation experiment. *Planetary and Space Science*, 57(12):1485–1490.

Schreiber, U. (2017). Private Communication.

Schutz, B. E., Zwally, H. J., Shuman, C. A., Hancock, D., and DiMarzio, J. P. (2005). Overview of the ICESat Mission. *Geophysical Research Letters*, 32(21):L21S01.

Showman, a. P. and Malhotra, R. (1999). The Galilean satellites. *Science (New York, N.Y.)*, 286(5437):77–84.

Siegman, A. E. (1986). *Lasers*. University Science Books, Sausalite, California.

Sirota, J. M., Bae, S., Millar, P., Mostofi, D., Webb, C., Schutz, B., Luthcke, S., Bae, S., Millar, P., Mostofi, D., Webb, C., Schutz, B., and Luthcke, S. (2005). The transmitter pointing determination in the Geoscience Laser Altimeter System. *Geophys. Res. Lett*, 32:22–11.

Smith, D. E., Zuber, M. T., Jackson, G. B., Cavanaugh, J. F., Neumann, G. A., Riris, H., Sun, X., Zellar, R. S., Coltharp, C., Connelly, J., Katz, R. B., Kleyner, I., Liiva, P., Matuszeski, A., Mazarico, E. M., Mcgarry, J. F., Novo-Gradac, A.-M., Ott, M. N., Peters, C., Ramos-Izquierdo, L. A., Ramsey, L., Rowlands, D. D., Schmidt, S., Stanley, ·. V., Iii, S., Shaw, G. B., Smith, J. C., Swinski, J.-P., Torrence, M. H., Unger, G., Yu, A. W., Zagwodzki, T. W., Smith, D. E., Neumann, G. A., Riris, H., Sun, X., Mazarico, E. M., Mcgarry, J. F., Rowlands, D. D., Scott Iii, V. S., Swinski, J.-P., Zagwodzki, T. W., Zuber, M. T., Jackson, G. B., Cavanaugh, J. F., Zellar, R. S., Coltharp, ·. C., Connelly, J., Katz, R. B., Kleyner, I., Matuszeski, A., Novo-Gradac, A.-M., Ott, M. N., Peters, C., Ramos-Izquierdo, L. A., Ramsey, L., Schmidt, S., Shaw, G. B., Smith, J. C., Unger, G., Yu, A. W., Torrence, M. H., and Liiva, P. (2010). The Lunar Orbiter Laser Altimeter Investigation on the Lunar Reconnaissance Orbiter Mission. *Space Sci Rev*, 150:209–241.

Smith, D. E., Zuber, M. T., Sun, X., Neumann, G. A., Cavanaugh, J. F., Mcgarry, J. F., and Zagwodzki, T. W. (2005). Supporting Online Material for Two-Way Laser Link Over Interplanetary Distance. *Science*, 311(53).

Smith, D. E., Zuber, M. T., Sun, X., Neumann, G. A., Cavanaugh, J. F., McGarry, J. F., and Zagwodzki, T. W. (2006). Two-way laser link over interplanetary distance. *Science (New York, N.Y.)*, 311(5757):53.

Steinbrügge, G., Stark, A., Hussmann, H., Sohl, F., and Oberst, J. (2015). Measuring tidal deformations by laser altimetry. A performance model for the Ganymede Laser Altimeter. *Planetary and Space Science*, 117:184–191.

Sun, X. and Neumann, G. A. (2015). Calibration of the Mercury Laser Altimeter on the MESSENGER Spacecraft. *IEEE Transactions on Geoscience and Remote Sensing*, 53(5):2860–2874.

Thomas, N., Spohn, T., Barriot, J.-P., Benz, W., Beutler, G., Christensen, U., Dehant, V., Fallnich, C., Giardini, D., Groussin, O., Gunderson, K., Hauber, E., Hilchenbach, M., Iess, L., Lamy, P., Lara, L.-M., Lognonné, P., Lopez-Moreno, J., Michaelis, H., Oberst, J., Resendes, D., Reynaud, J.-L., Rodrigo, R., Sasaki, S., Seiferlin, K., Wieczorek, M., and Whitby, J. (2007). The BepiColombo Laser Altimeter (BELA): Concept and baseline design. *Planetary and Space Science*, 55(10):1398–1413.

Tyahla, L. J. and Noll, C. (2016). International Laser Ranging Service. http://ilrs.gsfc.nasa.gov. Accessed: 2016-09-25.

Vance, S., Bouffard, M., Choukroun, M., and Sotin, C. (2014). Ganymedes internal structure including thermodynamics of magnesium sulfate oceans in contact with ice. *Planetary and Space Science*, 96:62–70.

Wegert, H. (2016). GALA Straylight Analysis Report. Technical report, Airbus DS Optronics.

Yelle, R. and Miller, S. (2004). Jupiter's Thermosphere and Ionosphere. In Bagenal, F., Dowling, T., and McKinnon, W., editors, *Jupiter: The Planet, Satellites and Magnetosphere*, pages 185–218. Cambridge University Press, Cambridge, U.K.

Zuber, M. T., Smith, D. E., Zellar, R. S., Neumann, G. A., Sun, X., Katz, R. B., Kleyner, I., Matuszeski, A., Mcgarry, J. F., Ott, M. N., Ramos-Izquierdo, L. A., Rowlands, D. D., Torrence, M. H., Zagwodzki, T. W., Zuber, M. T., Smith, D. E., Neumann, G. A., Sun, X., Mcgarry, J. F., Rowlands, D. D., Zagwodzki, T. W., Zellar, R. S., Katz, ·. R. B., Kleyner, I., Matuszeski, A., Ott, M. N., Ramos-Izquierdo, L. A., and Torrence, M. H. (2010). The Lunar Reconnaissance Orbiter Laser Ranging Investigation. *Space Sci Rev*, 150:63–80.